Simulation of Bone Remodeling Process around Dental Implant During the Healing Period

DISSERTATION

zur

Erlangung des Doktorgades (Dr.rer.nat.)

der

Mathematisch-Naturwissenschaftlischen Fakultät

der

Rheinischen Friedrich-Wilhelms-Universität Bonn

vorgelegt von

Salih Çelik

aus

Mardin/Türkei

Bonn, 2020

... ji diya min re.

... to my mother.

Abstract

This interdisciplinary thesis deals with the numerical investigation of bone remodeling around dental implants during the healing period with regard to biomechanical aspects. The aim of the study was to develop algorithms for the simulation of the tissue behavior during this very critical phase of implant healing, including osseointegration processes at the implant surface as a time-dependent function in response to local mechanical stimulus.

Initially, two dimensional (2D) and three dimensional (3D) Finite Element (FE) simulations were performed to calculate the loading of the bone bed around dental implants. The remodeling theory presented by Li et al. was used in our remodeling simulations. Three different layers with three different thicknesses were added around the implant in the models to simulate the osseointegration phases. Phase 1: Layers of 0.1, 0.2, and 0.3 mm, respectively, of connective tissue (CT), surrounded the implant. Phase 2: Layers of 0.1, 0.2, and 0.3 mm CT, soft callus (SOC), and intermediate soft callus (MSC) surrounded the implant. Phase 3: Layers of 0.1, 0.2, and 0.3 mm SOC, MSC, and stiff callus (SC) surrounded the implant. Different boundary conditions and material properties were applied to the models considering different bone remodeling parameters. Various forces (100-300 N) were applied on the implants at 20° and 0° from their long axis. The model was subjected to a compression and tension pressure with 0.5-10.0 MPa on the lingual and the labial sides to simulate muscle forces. Additionally, implant stability and the effect of the bending forces were investigated in this thesis.

By comparing the applied force on the implant of 100 and 300 N, the density of bone reached the maximum value on the cortical bone and the outside of the spongious bone at 300 N. Comparing the muscle forces on the models, the bone formation was obtained in the spongious bone and around the implant at 1.5-4.0 MPa. Osseointegration was observed with a layer of 0.1 mm thickness in the 2D model. With a layer of 0.3 mm simulation resulted in bone resorption.

The results of these simulations compared to the studies of several other authors. Subsequently, so-called bone remodeling theories were used to simulate the long-term behavior of the bone bed around the cyclically loaded implant. A stable region for all remodeling parameters could be determined, such that bone density resulted in an equilibrium state with a soft tissue layer

of 0.1 mm, which is in accordance with clinical findings. These studies will help to predict the osseointegration of dental implants and will help to assess the clinical reliability, especially of immediately loaded implants, and, if necessary, to optimize their design and their prosthetic superstructure. This could offer a future way into a patient dependent treatment planning and the prediction of long-term stability of dental implants.

Acknowledgement

List of Figures

List of Tables

List of Abbreviations

2D Two-Dimensional.

3D Three-Dimensional.

BMD Bone Mineral Density.

BMU Basic Multicellular Unit.

CT Connective Tissue.

EEL Element Edge Lengths.

FE Finite Element.

FEA Finite Element Analysis.

FEM Finite Element Method.

MSC Intermediate Soft Callus.

PDL Periodontal Ligament.

SC Stiff Callus.

SED Strain Energy Density.

SOC Soft Callus.

Nomenclature

$\emptyset$ Diameter

Δt Time step

ϵ Strain Tensor

$\mu\varepsilon$ Equivalent of total strain

ρ Density of Bone

ρ_{cb} Density of Cortical Bone

ρ_{max} Upper Limit for the Density

ρ_{min} Lower Limit for the Density

ρ_{tt} Density of Current Tissue Type

σ Stress Tensor

σ_1 Lower Critical Stress

σ_2 Upper Critical Stress

υ Poisson's Ratio

A_{ij} Matrix of Remodeling Coefficients

B_{ij} Matrix of Remodeling Coefficients

C Constant

C_x Remodeling Rate Coefficient

E Young's Modulus

e_{ij}° Equilibrium Strain Tensor

e_{ij} Actual Strain Tensor

F Force

k Threshold Value

$K, B,$ D   Bone Remodeling Parameters

L Length

n Number of Elements

n_{max} Maximum Number of Steps in the Euler Iteration

U Strain Energy Density

U/ρ Mechanical Daily Stimulus

U^* Equilibrium Value of Strain Energy Density

w Half of the Width of the Dead Zone

Table of Contents

1 INTRODUCTION

In this chapter, we want to give some information about anatomical planes, facial skeleton, muscle, and tooth positions in the human body. There is just a short introduction to the tissues surrounding the teeth. The aim of this chapter was to give some information to engineers, physicists, or mathematicians, not to the medical scientist.

1.1 Anatomical Reference Frames

We start by describing anatomical planes of the human body. It is also essential to talk about the localization of the body. The coronal, sagittal, and transverse planes are corresponding to a frontal, profile, and bottom-up view, respectively, see Fig.1.1.
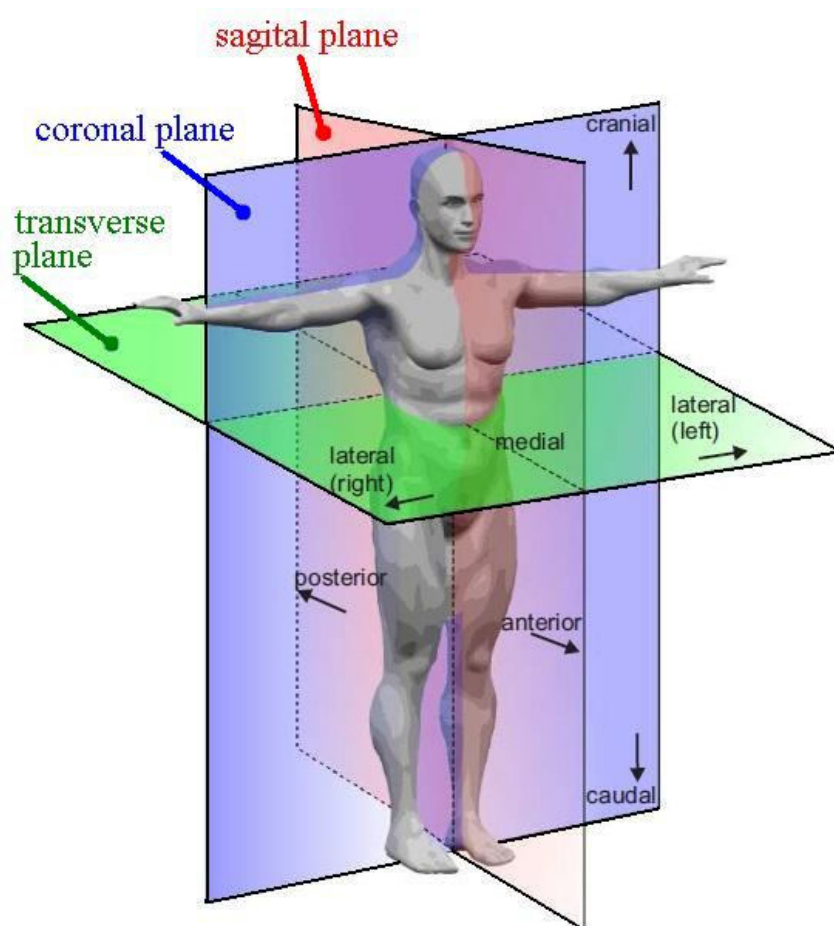
Figure 1.1: Anatomical planes of the human body (modified from [1]).

Figure 1.1 displays six orientations: anterior-posterior is from front to back, cranial-caudal is from head to toes, lateral is towards the exterior of the body, medial is towards the center of the body, the distal is at the tip of the limb, the proximal one is where it joins the body.

1.2 The Facial Skeleton

Figure 1.2 is a view of the facial skeleton. The superior facial complex has thirteen bones. The facial skeleton has mainly two parts called Maxilla and Mandible. Maxilla in Figure 1.2 is the main bone in this region. The most important tasks of the Maxilla are to protect the face, hold the upper teeth in place, and design the floor of the nose [1].
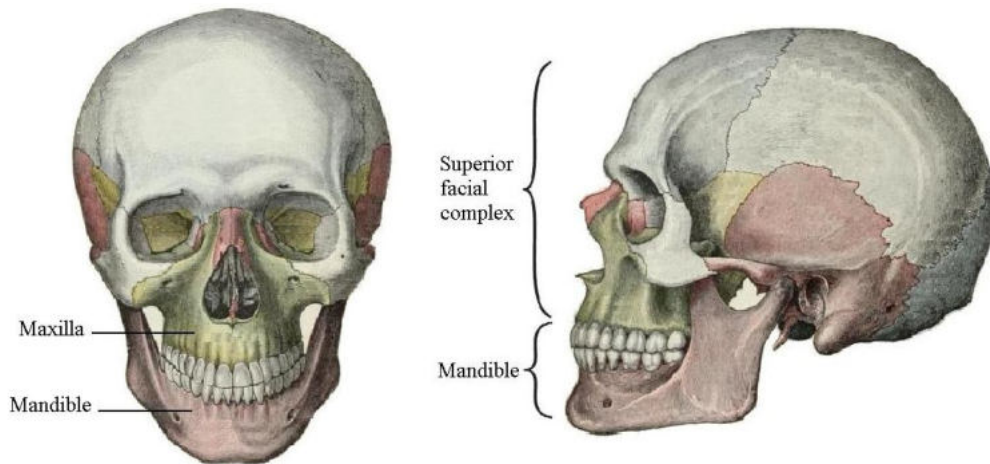
Figure 1.2: Anterior-posterior views of the facial skeleton (adapted from [2]).
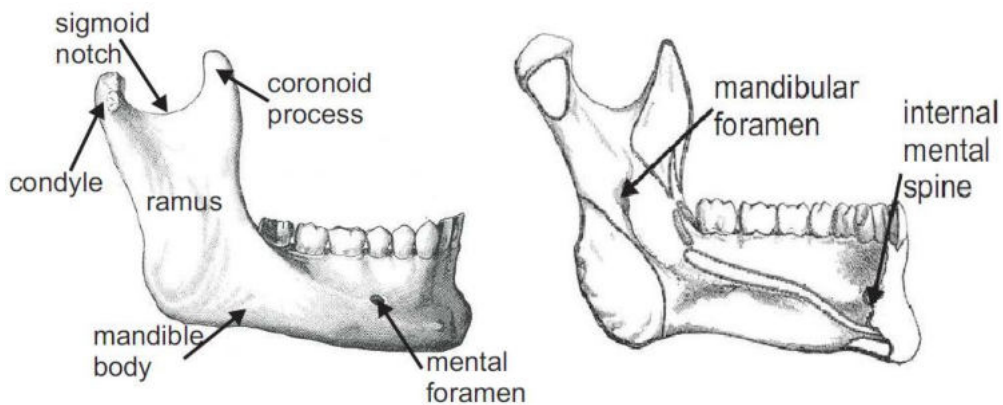
Figure 1.3: Mandible (modified after [1, 2]).

The mandible however, is responsible for holding the teeth in place and promoting the lower part of the face (Figure 1.3). The only mobile bone of the face is the mandible, which is necessary to move the mouth. The mandible is joined on both sides by the temporomandibular joints. Several muscles of the face are attached to the mandible. Attachment sites of the muscles are shown in Figure 1.4 on page 4. Masseter (M1, M2), anterior temporalis (M3, M4), lateral pterygoid (M5, M6), medial pterygoid (M7, M8), and anterior digastric (M9, M10) muscles are shown in Figure 1.4. The directions of the muscles are shown with the arrows. The points of both condyles are shown with the direction of their forces ($F_{condyle,R}$, $F_{condyle,L}$) [1, 2].

Teeth are the hardest structure of the body, but all teeth are not in the same structure. For example, molars are powerful and the strongest teeth. Figure 1.5 shows the tooth positions. The tooth crown is the visible portion of the tooth; the root is the lower two-thirds of the tooth. It is surrounded by and anchored in the bone. All teeth have different roots. For example, molars and premolars are multi-rooted, one root and one root, respectively. Figure 1.6 shows the surrounding tissues around the tooth. The crown is covered by enamel, which is the outer layer of the tooth. The enamel is protecting the teeth against damage. Tooth enamel is the hardest tissue in the human body. The second layer of the tooth is dentin, which is the largest part of the tooth. Dental pulp is a chamber that contains nerve tissues and blood vessels.

The periodontal ligament (PDL) is a connective tissue between jaw bone and cementum. It is one of the tissues that support the tooth. The PDL is responsible for attaching the tooth to the jaw bone. It has many functions, like supporting and remodeling functions. Alveolar bone has cortical plates and trabecular bone. It is part of the jaws that form and also support the teeth. Damage to the alveolar bone results in serious problems. Loss of teeth is the main and most serious problem when alveolar bone is damaged.

1.3   Bone Biology

Bone is a dynamic and living tissue that continually remodels. It has one of the most complex structures in the body. Magnetic resonance imaging (MRI) and nano-indentation are now offering new insights into bone microstructure. Furthermore, not all the cells are visible under light microscopy. Bone can adapt to mechanical factors. One of the primary roles of bone is to protect the soft organs in the body.

1.3.1 Bone Tissue

Bone tissue is the major supportive connective tissue of the body. Bone tissue includes water, organic components, and non-organic mineral salts. Collagen fibers are an example of organic components. Calcium, phosphate, and magnesium are the main non-organic components in the bone tissue. Bone tissue also has a living component and bone cells. Many types of factors with different types of cells are active in bone activities. Osteoblasts, osteoclasts, and osteocytes are the three main cells for bone activities. Osteoblasts are responsible for new bone formation, and osteoclasts mainly remove bone tissue. The carrying of calcium and other ions between bone minerals and blood plasma is arranged by osteocytes [4]. They are the major constituents involved in the process of bone remodeling.
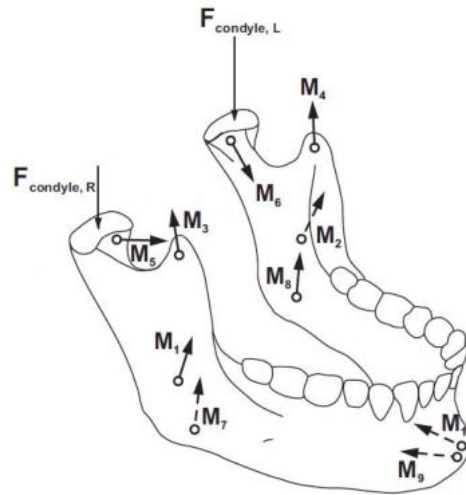
Figure 1.4: Muscles and anatomical forces on the mandible (modified after [1, 2]).
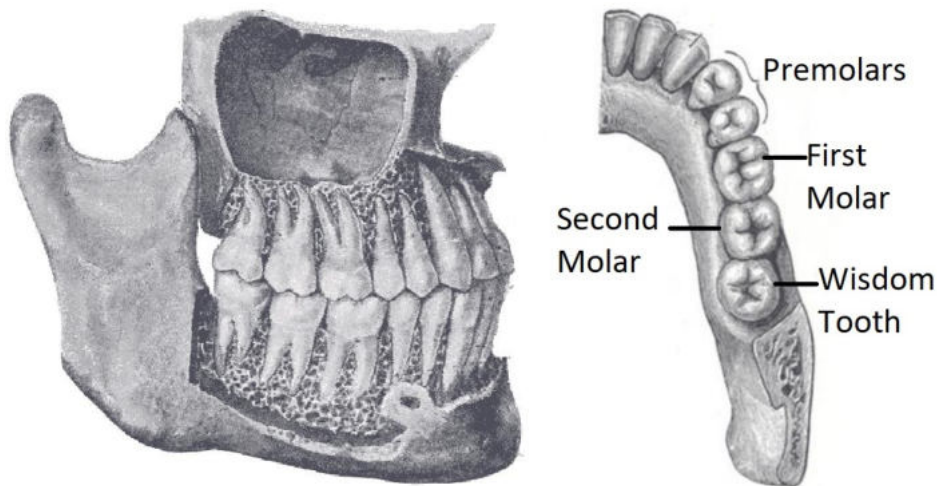
Figure 1.5: Position of the teeth in both maxilla and mandible (adapted from [1, 2]).
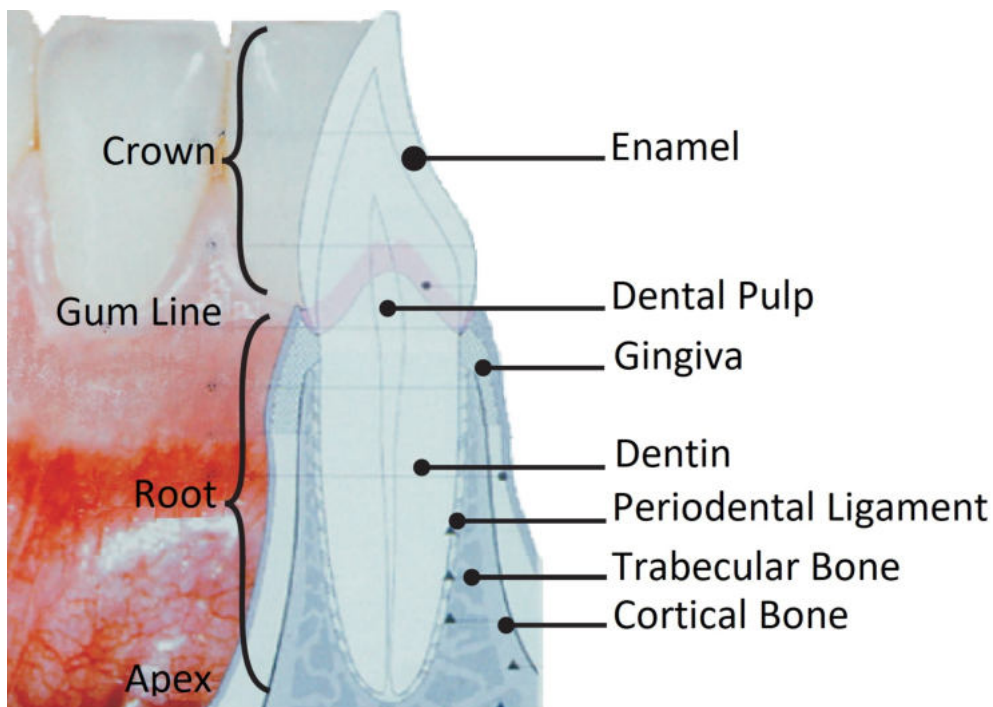
Figure 1.6: Surrounding tissues around teeth (adapted from [3]).

Bone has a self-repair mechanism with its own vessels and living cells. It produces red and white blood cells. Bone has a complex internal and external structure. The bone has a self-repairing feature in external loading. It can adjust itself to its mass, shape, and properties against the external loads without breaking or causing pain. Bone has two significant forms of bone tissue, which is called cortical bone and trabecular bone. The outside of the bone is called cortical bone, which is denser than the trabecular bone [5]. Cancellous bone is comprised of trabeculae. Naturally, cortical bone has its predominant location in the neighborhood of the joints, and trabecular bone has the predominant location in the central section of the bone [6].

1.3.2 Cancellous Bone (or Trabecular Bone)

Cancellous bone is also called spongy bone or trabecular bone because it is composed of short struts of bone material called trabeculae, as shown in Figure 1.7. Spongy bone is less dense, softer, and weaker compared to cortical bone. It is surrounded by cortical bone. Spongy bone is vascularized and has red bone marrow to produce blood cells. Osteoblast cells are produced in the tissue of the spongy bone area.

In Figure 1.8, a spongy bone is shown that has a connection with rods

and plates. Spongy bone keeps the bone marrow and the calcium between the rods and plates. This part of the bone plays an important role in being replaced and renewed by remodeling within years. The regions of these tissues will remodel to be enough stronger in the way of forces [7].

Figure 1.7: Cancellous bone (modified after [8]).

1.3.3 Cortical Bone (or Compact Bone)

Cortical bone is a solid body. It is transversed by many channels, as shown in Figure 1.9. The percentage of the density in the porosity is the impressive point between cortical and spongy bone. In the porosity regions, cortical bone is less than 5%, where spongy bone is much less in the shape of rods or plates [Figure 1.9]. Cortical bone percentage is 80% of bony tissue in the human body. In Figure 1.9 the Haversian system is shown which is the functional unit of cortical bone. The Haversian system is also called an
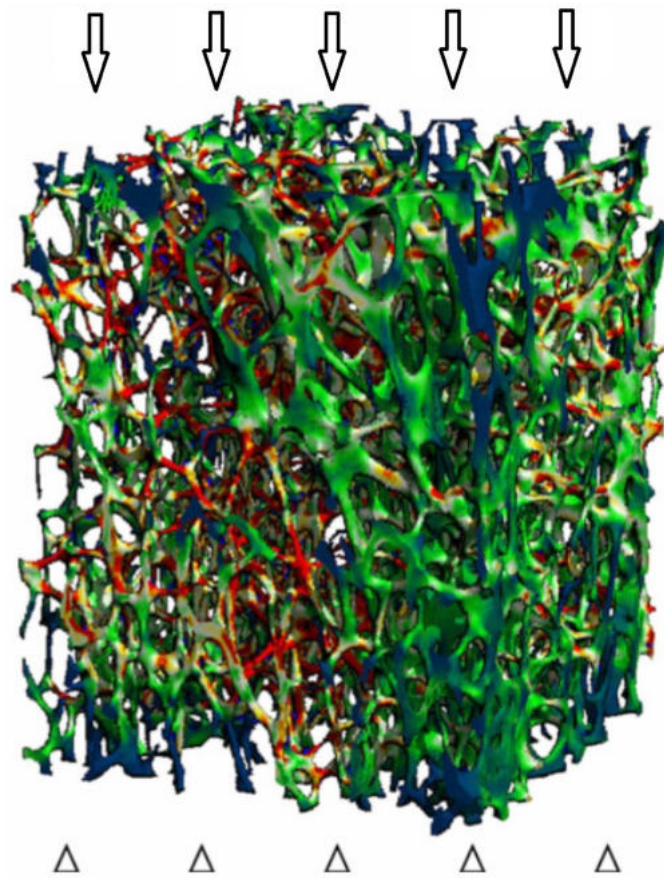
Figure 1.8: A micro-CT reconstruction of a section of trabecular bone. Red areas correspond to regions under the highest calculated local stresses that could be generated by a 1% compressive strain; blue areas experience the lowest stresses. Each rod is approximately $100\,\mu m$ in diameter (modified after [9]).

osteon. The diameter of the osteon is approximately 100 to $300\,\mu m$, and it is a cylindrical structure. Additionally, blood vessels and nerves are found in the Haversian canal. Between different Haversian systems, the blood vessels and osteons are connected with the Volkmann's canals [10].

1.4 Bone Modeling and Remodeling

Bone modeling and remodeling processes are described as two different mechanisms from different types of bone cells that work individually to create bone formation and bone resorption [12]. These two processes work together in the growing skeleton to repair structurally compromised regions of bone.
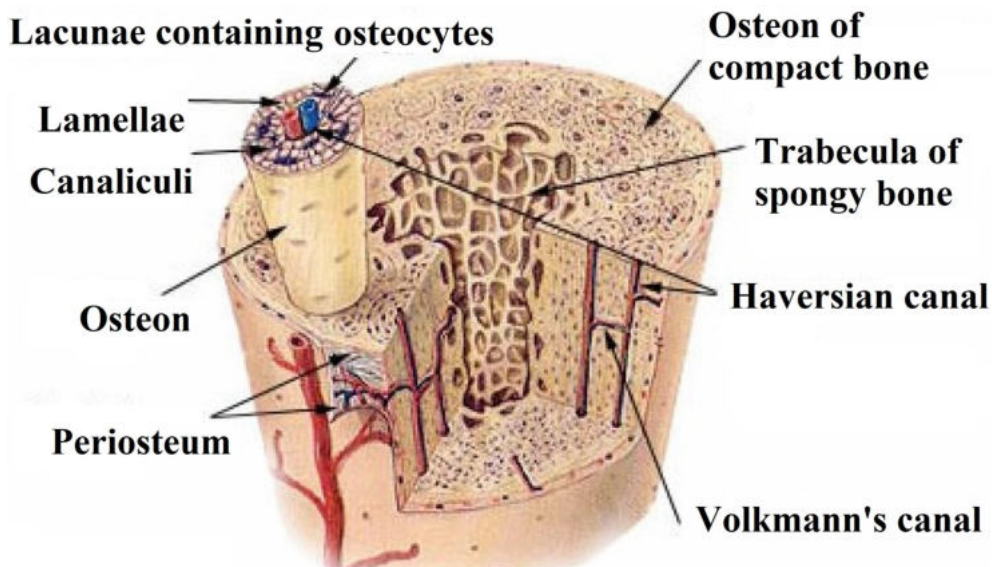
Figure 1.9: Structural organization of bone. Modified from [10].

Bone modeling is a process that works when bone resorption and formation occur on separate surfaces. During bone modeling, osteoblasts and osteoclasts are individually working at the different sites of the bone. Bone changes its shape and mass with the bone modeling process. An example of this process is in length and diameter of long bones. This process occurs from birth to adulthood.

In 1892, the first time the German scientist Julius Wolff defined a basic aspect of a theory to describe bone remodeling processes and bone adaptation [13], and the process of bone modeling and remodeling is called "'Wolff's Law"'. Although - with respect to Physics or Mathematics - Wolff did not formulate a quantitative law, he described the relationships between bone loading and bone structure. Furthermore, he described the orientation of the trabeculae that follow the stress trajectories due to the external loading. He assumed that all processes are regulated on the bony tissue level, and cellular reactions on local tissue stress control the bone mass.

In the past thirty years, a number of bone remodeling theories have been developed. They all are based upon the assumption that it is the loading history of the bone that determines its structure and its adaptation [14–16]. The term loading history collects all variations combined with the external loading of the bone. Due to the idealizations, the models developed must be
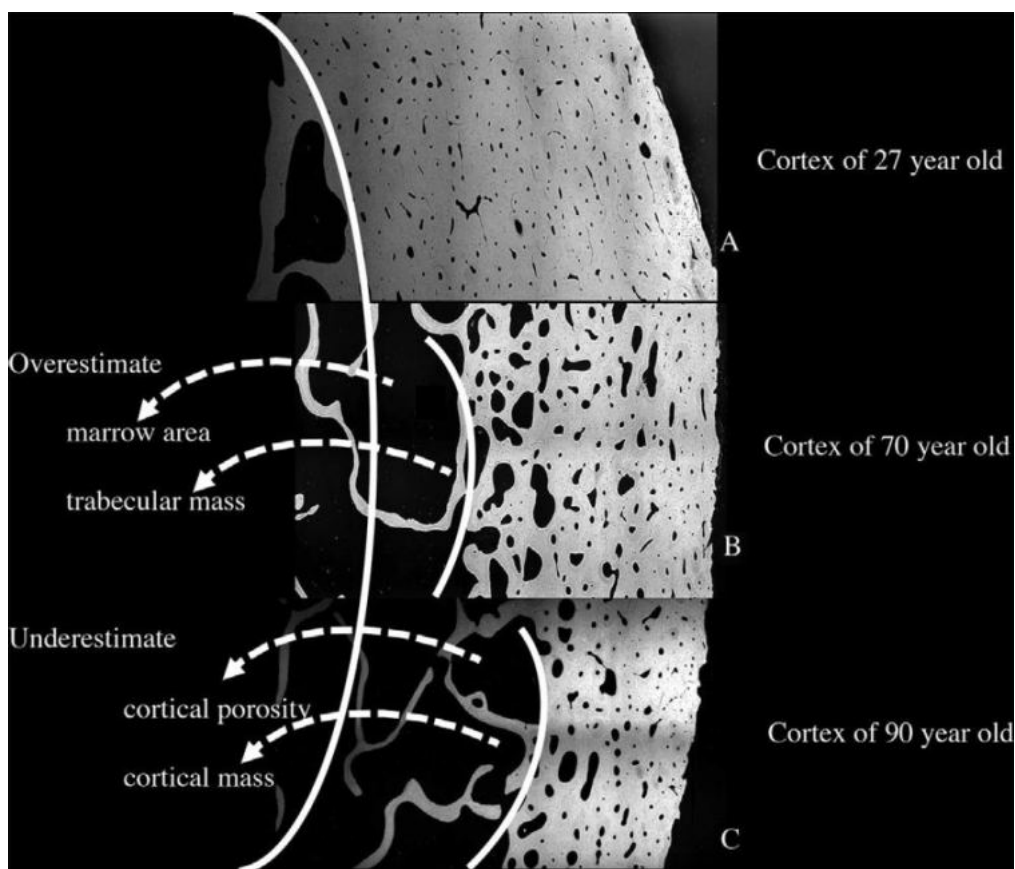
Figure 1.10: Corroded bone cortex with the effect of bone remodeling. The endocortical surface (white line A of a specimen from a 27-year-old) denotes the true medullary cavity/cortical interface achieved at completion of growth. If the surface of the thinned but still compact appearing cortex (white line B in a 70-year-old or C in a 90-year-old) is erroneously described as the endocortical surface, several errors occur by incorrectly apportioning in the cortical fragments and porosity that created them to the seemingly expanded medullary canal (modified after [11]).

regarded as being phenomenological and qualitative. A Schematic view of bone remodeling is shown in Figure 1.11 on page 10.

Bone resorption and bone formation are balanced in a homeostatic equilibrium. In this equilibrium, bone can be continuously repaired by new tissue; in this way, bone adapts to mechanical loads and strain. Frost has defined this fact as bone remodeling in 1990 [18]. Furthermore, bone remodeling has always the same procedure as shown below [19]:
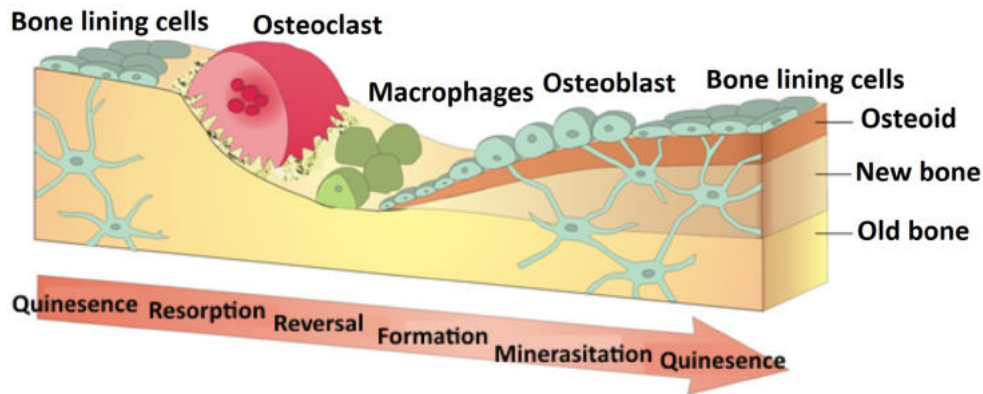
Figure 1.11: Schematic view of bone remodeling phases (modified after [17]).

activation $\rightarrow$ resorption $\rightarrow$ formation sequence ($A \rightarrow R \rightarrow F$).

Bone remodeling has two different phenomenological descriptions, which are called "'surface"' and "'internal"' remodeling [20]. Osteoclasts and osteoblasts work together in the bone remodeling process in so-called basic multicellular units (BMU). Because of the large surface of trabecular bone, it is more actively remodeled than cortical bone. The moving speed of the osteoclasts is approximately 25 μm/day on the surface of trabecular bone [21]. Remodeling peaks until the mid '30s and by the way, until the age of 40. Thus adults begin to lose bone mass at a significant rate.

In a basic BMU, each unit of cells remodels bone in reaction of mechanical and biological stimuli. Bone remodeling is a sensible process concerning mechanical and piezo-electrical conditions. Bone formation increases when mechanical stresses increase in bone [22].

The processes of resorption and formation are matching each other as a coupled phenomenon, where the osteoblast cells work after the osteoclast cells because of the morphology of the remodeling BMU. This relationship is a controlled process, ensuring that where old bone is removed, new bone will be repaired [23].

The process of old bone removal and new bone formation in bone remodeling is called bone balance. This bone balance can be affected in many disease states, i.e., in osteoporotic patients, resorption and formation are coupled though more bone is resorbed than is replaced from the BMU [24].

Bone remodeling tissue is regularly remodeled in BMUs in the growing, adult, and aging skeleton. The BMUs depend on many factors in a specified volume of tissue at any one moment [25]. The activation frequency (Ac.f) is the first factor. This factor is the "'birth rate"' of new BMUs. In a large number of secondary osteons, ultimately, and a large number of active BMUs, a high activation frequency will result. The longevity of individual BMUs is the second factor, which is correlated to the speed with which the BMU travels over the tissue area. This second factor is called the sigma period (σ_{RC}). This sigma factor quantifies the time which takes a BMU to remodel a two-dimensional part through a part of the bone. This concept would take approximately 120 days for the entire BMU to pass through a plane, leaving a new osteon behind in the human cortical bone. The initiation and increase of the diameter of the resorption cavity by the osteoclasts would take roughly 20 days. And after that, by ten days of relative quiescence, the centripetal deposition of bone matrix by osteoblast teams would take 90 days. Sigma periods are often subdivided into two periods which are called resorption [$\sigma_{RC(r)}$] and formation [$\sigma_{RC(f)}$] periods [26].

The average age of cortical bone is 20 years, and it is one to four years for trabecular bone [27]. Bone remodeling plays several roles in the bone during its process. It assists in removing microdamage and replacing dead bone and also adapting microarchitecture to local stress. Bone remodeling removes trabeculae on cancellous bone. Also, it increases cortical porosity on the cortical bone, decreases cortical width, and reduces bone strength [5]. For example the radius remodels in reaction to the extra load applied when the ulna was removed from a pig [28]. Bone remodeling reacts individually to mechanical loading in immature bone. Increased stress at the growth plate reduces bone growth, decreased stress at the growth place increases it [29]. This affair may lead to the deformity in pediatric scoliosis and Blount's disease. In immature bone, the piezo-electrical charges can have contrary effects on bone remodeling. The electro-negative effect happens with the compression side of the bone, and it is stimulating bone formation with osteoblasts. On the other hand, a electro-positive effect happens with the tension side of the bone, and it is stimulating bone resorption with osteoclasts [22]. In other words, bone formation types occur due to the kind of force applied to the bone. Compressive forces, tensile forces, and shear forces stimulate endochondral ossification, intramembranous ossification, and fibrous tissue formation, respectively [30]. This relationship is important for bone healing.

1.4.1   Bone Remodeling and Mechanical Stimulus

Bone is an active tissue in the human skeletal system, and it evolves to adapt to the changes in the environment. More than a century, the ability of the bone has been an alluring research topic for scientists. But we can say it openly that the scientists have to work more with the bone to understand the bone resorption and deposition processes thoroughly.

As mentioned before, Wolff proposed the earliest theory to explain the bone deposition and resorption in 1870, and elaborated it in a monograph in 1892. Wolff's law is well known in the biomechanics community. According to Wolff's law, for an increase in the function, the bone reacts with deposition, and for a decrease in function, the bone reacts with resorption. In 1892 Wolff's law was defined as follows: "Every change in the form and function of a bone or of their function alone is followed by certain definite changes in their internal architecture, and equally definite secondary alteration in their external conformation, in accordance with mathematical laws." Wolff said that bone formation occurs from the force of muscular tensions and static stresses of the body in the erect position. All these forces always act with the correct angles to the bone. Even though many authors agree with Wolff's law, some of them still have some doubts about this theory.

According to clinical experiments, bone "melts away" from around orthopedic implants and screws where too high stresses are located. Consequently, the bone may either be sensible against the demand placed upon it or may have got an upper demand cut-off level above which it changes its response [31]. Bassett wanted to propose a restatement of Wolff's law in modern terms: "The form of the bone being given, the bone elements place or displace themselves in the direction of the functional pressures and increase or decrease their mass to reflect the amount of functional pressure" [32]. Wolff's law is also summarized as a feedback mechanism by Bassett [33].

For decades, many theories have been suggested to define the loading mechanism in bone structure. Many scientists thought that the mechanical stress is somehow directly acting on current osteoblasts or osteoclasts to influence bone shape and mass. The mechanostat theory is one of the most accepted theories which was defined by Harold Frost [34–36].

1.4.2 Harold Frost's Mechanostat

Frost described the adaptation of bone tissues to their mechanical environment. He proposed that bone mass fits the typical mechanical usage (MU) of a healthy skeleton. This idea shows that some mechanism(s) create(s) their biological mechanisms from the MU of bone to fix the incongruence between bone mass and its MU. That mechanism was called a mechanostat. He also created a relation between MU and bone mass [20, 34]:

$$MU \rightarrow bone \rightarrow mechanostat \rightarrow bone\ mass\ effect$$

Relation (1): Relationship between biological mechanism, bone architecture and bone mass.

Relation (1) shows the communication between biological mechanisms and bone architecture and bone mass originally with a feedback loop, which was suggested by Frost [20] and later accepted by most biomechanist [37–39]. The mechanostat should involve three different biological mechanisms: growth, modeling, and remodeling. In response to the MU, the bone mass can be affected in some way by all these mechanisms. In this theory, MU consists of all physical loads and motions imposed on the bony skeleton [34].

Strain or deformation is a geometrical change in the dimension of the material when an external force is applied. The ratio of this change of size in the material to its actual length is called strain. Strain is therefore expressed in absolute terms without units or percentage. Frost defined four different regions of bone deformation and related each region to a mechanical adaptation (Figure 1.13):

- Disuse Atrophy,

- Steady State,

- Physiological Overload and

- Pathological Overload.

The strain is dimensionless because it changes in length over length. In regard to bone, for strain commonly the term microstrain (10^{-6}) is used because bone strains are typically very small, which is between 100 and 2,000 $\mu\varepsilon$. Frost proposed that bone responds to a complex interaction of time and strain, ideas that incorporated elements of frequency, rate, and magnitude.
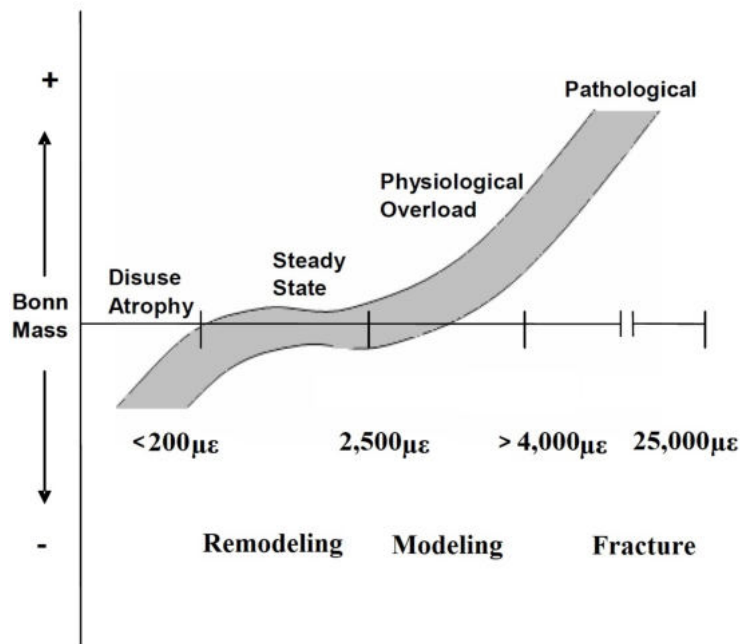
Figure 1.13: The Mechanostat Theory from Frost. In the disuse atrophy, the limit of strain magnitude with minimal Effective Strain (MES) of 50 to 250 $\mu\varepsilon$ is all-important to provide the bone mass according to the bone loss. Bone remodeling area is from 50 to 250 and 2,500 to 4,000 $\mu\varepsilon$. Shaded area shows the scope of response in terms of change in bone mass. Peak load magnitudes creating strains above 2,500 to 4,000 $\mu\varepsilon$ MES, lead to new bone formation (modelling) that continues until increased bone mass decreases strain values below modelling MES. At the end, the rapid catastrophic fracture takes place when peak load levels exceed 25,000 $\mu\varepsilon$ (modified after [40]).

Because of this reason, he used the term "'strain"' in a more general sense than it is normally used [41].

In Figure 1.13, Frost suggested that the magnitude of the strain is the mechanical stimulus for bone functional adaptation. When the peak strain magnitude falls below 50-250 $\mu\varepsilon$, disuse atrophy is suggested to occur at low frequencies. If an area of bone lost mechanical loading, then a relative disuse atrophy would exist in which there is a loss of net bone mass.

In general, bone mass (an indirect measure of the effects of local mechanical and structural properties) would be preserved in a physiologically reasonable range that arranges acceptable mechanical properties for the kind of loads the local area of bone experienced. Bone mass and bone strength

14

are reduced in this regime as well as bone opposition and bone repair (re-modeling).

When strain is between ca. 200 $\mu\varepsilon$ and ca. 2,500 $\mu\varepsilon$ bone formation and bone resorption are equal, which means bone mass and bone strength stay constant and bone repair (remodeling) is in the steady-state region. In the physiological overload region, which is between 2,500 and 4,000 $\mu\varepsilon$, bone growth (modeling) happens in this part. It means bone mass and bone strength are increased between these strain values. Immature bone occurs in the physiological overload region mineralized, and after that weaker than the lamellar bone. Bone mass will increase during strain increase in this regime as far as the bony interface fits to these changes, and then load strain values will fall back into the region of steady-state. This procedure for example causes ridge resorption after tooth loss. The pathological overload regime is defined with peak strain magnitudes of over 4,000 $\mu\varepsilon$, which may result in net bone resorption. Bone fracture occurs in this region while maximum elastically deformation exceeds in the pathological overload region.

Cumulative activity
MU increased: growth and modeling increase; remodeling declines
MU decreased: growth and modeling decrease; remodeling increases
Compact bone mass
MU increased: mass increases in children, is conserved in adults
MU decreased: gains decrease in children, mass decreases in adults due to marrow cavity expansion
Trabecular bone mass
MU increased: existing spongious is conserved at all ages; additions of new spongious increases in children
MU decreased: loss of existing spongious increases at all ages; addition of new spongious decreases in children
Bone architecture
MU increased: Children: thicker cortex, greater outside bone diameter, denser spongious, smaller marrow cavity, slightly longer bone
Adults: conserved spongious and cortical-endosteal bone
MU decreased: Children: smaller outside diameter of bone, osteopenic spongious, slightly shorter bone
Adults: larger marrow cavity, osteopenic spongious

Table 1.1: Mechanical usage (MU) effects on bone growth, modeling, global remodeling, and mass.

Table 1.1 shows MU effects which are shown by many clinical, experimental, and histomorphometric evidence, some cited by [38, 42–56].

The total amount of spongious bone increases during growth because the growth-related additions of new primary spongious bone exceeds the removal by continuing remodeling of the existing spongious bone. When growth stops at maturity, its addition of new spongious bone do likewise; after that, the net losses due to continuing remodeling begins to become apparent (table 1.1 adapted from material in [57]). Growth and modeling drifts are not ordinarily effective in human adults [34].

1.4.3 Experimental Investigation of Bone Remodeling

The mechanism of mechanostat theory from Frost has been applied in numerous in vivo studies in animals in which artificial loads have been applied to the bones on one side and the modeling and remodeling responses in the loaded bones were compared with those in the non-loaded contra-lateral pair [58–67] on the other side. For example, several researchers [68–79] worked with rabbit tibia, rat ulna, mice, mouse ulna, murine tibia, mouse tibia, mouse fibula in vivo. Pearce et al. [80] worked with different animals to check the resemblance between animal and human bone in terms of macrostructure, microstructure, bone composition, and bone remodeling rate in dogs, sheep/goat, pigs, and rabbits. This article showed that pigs have the most similar bone remodeling behavior with human bone. Dogs, sheep/goats, and rabbits have less similarity with human bone.

Besides that, an animal experiment reported that in rapidly growing male rats in single period of dynamic high-magnitude axial loading of the ulna on one side was correlated with significant levels of new cortical bone formation at the periosteal surface of the contra-lateral non-loaded ulna and in the cortical regions of adjacent bones in the loaded limbs. In this study it was concluded that mechanically adaptive bone (re)modeling is dominated by procedures with substantial systemic and central nervous components [81].

Bone remodeling has been investigated via numerous animal experiments. Hert designed the first systematic series of tests to investigate the mechanism of functional adaptation in bone tissue [82]. Later then he and his coworkers worked with the tibias of rabbits applying artificial loads [82–84]. Some other researchers have worked with sheep experiments under controlled dynamic loads [85, 86], followed by chicken experiments [87, 88], and finally turkeys [89].

Then again bone mass increased with increasing loading during the loading applied to the bone in vivo in some other animal experiments like turkey ulna, mouse tibia, and mouse caudal vertebra, respectively from [90–92], and some other animal experiments [93–97]. In some studies it has been reported that there is a relationship between static load and remodeling activity [98–100].

A research group were the first to work with deer antler. A novel animal study, using the deer antler as an implant bed has been established. This animal study allows the investigation of the healing processes around dental implants, without the necessity to sacrifice the animals [101].

Many studies reported that minor influence of loading on peri-implant bone contrasts with the large anabolic response on intact bone [64, 92, 102]. Lambers and colleagues studied using the mouse caudal vertebra. They reported that bone mass increases when increasing loading is applied to the bone in vivo [92]. Ogawa and colleagues studied the proximal tibia of rats to simulate immediate loading after implantation [103]. Mechanically, bone (re)modeling is stimulated with the local bone formation and resorption occurs at sites of high and low tissue strains, sequentially [102, 104, 105]. Jariwala et al. [106] studied with the proximal tibia of rats. They adopted in vivo micro-CT to characterize the time course of cancellous bone regeneration around non-loaded and loaded implants. The authors applied loading directly to the implant and observed a large influence on osseointegration at the bone-implant interface. Also, Li and colleagues pointed out the influence of mechanical loading on peri-implant bone regeneration [107]. Bone remodeling around dental implants has been studied in different periods, until complete osseointegration of the implants was achieved in Sika deer antlers [108].

1.4.4 Computer Simulation of Bone remodeling

Numerical simulation of the bone/implant system using finite element methods (FEM) only represents a stationary impression of the current mechanical status. Changing the bone loading by the insertion of an implant means that an existing state of equilibrium is disturbed. The bone, in turn, tries to adapt to the new loading situation, thus changing in structure and density, which changes the mechanical condition again. This process runs until a new state of equilibrium is reached, which is adapted to the changed loading situation. This process might go so far that the implant loses its anchorage in

the bone. Strictly speaking, the bone is a dynamic, self-optimizing structure that should be simulated with an appropriate model.

Different physical properties on the cellular level are possible and have been used as a key stimulus to formulate the bone remodeling simulations [38, 109–113]: piezoelectric signals, flow potentials, mechanical stresses and strains, strain energy densities, invariant quantities derived from the afore-mentioned. A first mathematical model was presented in 1972 by Kummer to formulate the bone remodeling theory [114]. In this model, the bone remodeling was connected to the tension in the bone by a cubic approach. Further work about mechanical stimuli that have been considered in bone remodeling include strain or stress tensors [115], strain [6, 116], stress [114, 117], effective stress [109, 118, 119], strain energy [112, 120], or strain rate [111]. Several researchers have investigated mathematical theories that might clarify development of bone density [121, 122], trabecular architecture [123] and [118, 121, 124] as effects of external forces, using finite element analysis (FEA) computer simulation models. From mechanical point of view, the model presented by Huiskes and his co-works seems to be the most advanced. It can either simulate external shape adaptation or internal adaptation by a change of the trabecular structure, respectively. Additionally, processes of combined internal and external bone adaptation can be simulated. Good correlation was found in combined animal experimental and numerical studies [125]. Furthermore, a theory assuming mechano-sensory and signaling functions for the osteocytes could explain the mechanical adaptation of trabecular density and trabecular architecture [126–128] within the conceptual theories of Frost [18, 129].

Bone remodeling theory on the cellular scale was simulated using FEM by one research group. According to their theory, osteoclasts could cause trabecular perforations if they resorb bone based on local microdamage. They calculated the local mechanical behavior of the tissue and extrapolated the cellular behavior based on a threshold response to the strain [130].

Bone adaptive behavior was simulated with mathematical models using FE methods as a simulation tool [131, 132]. Additionally, a two-dimensional finite element analysis (FEA) model was built up to test a balance between osteoclast resorption and osteoblast formation, modulated by external loads through osteocytic sensing and signaling [133, 134]. Subsequently, a three-dimensional version of the FEA model was created to test its predictions relative to trabecular bone metabolism as it occurs in the reality of bone modeling and remodeling [135]. A bone remodeling model, including the

directional activity of BMUs, has been published by Martinez et al. [136]. The goal of the study was to describe the macroscopic evolution of BMUs during bone remodeling and relate it with the anisotropy distribution in bone, which is influenced by the loads borne by certain specimens. An FE model was created to obtain the anisotropic and mechanical properties of the human proximal femur under physiological loads with initial conditions corresponding to a heterogeneous/isotropic bone. The potential of the model was analyzed to predict the alignment of the bone microstructure with external loads in different situations.

Geraldes described a novel method of achieving a physiological orthotropic heterogeneous model of the femur by incorporating a bone adaptation algorithm with FE modeling of the femur spanning the hip and knee joints. The purpose of the thesis was to describe the creation, development, and validation of this method of achieving a physiological orthotropic heterogeneous model of the femur. A fully balanced loading configuration was remodeled using muscle and ligament forces applied to the 3D FE model [137]. Lou et al. [138] performed numerical studies with human femur remodeling using medical image data. The purpose of the study was the utilization of human medical computer tomography (CT) images to quantitatively evaluate two kinds of "'error-driven"' material algorithms, that is, the isotropic and orthopic algorithms, for bone remodeling. In this study, a combination of the FE method and the material algorithms was used for bone remodeling simulations. This "'error-driven"' bone material algorithm has been developed from [133, 139–141] and [142, 143], assuming bone is either an isotropic or orthotropic material, respectively. This algorithm was also used with total hip arthroplasty [144, 145] for bone remodeling.

1.4.5 Computer Simulation of Bone Remodeling Around Dental Implants

The developed adaptive finite element models are capable of simulating bone remodeling phenomena as a result of a given stress/strain distribution. An application of these theories to describe bone remodeling phenomena around dental implants should follow these concepts. Today, even on an international level there are only a few groups that work in this field [146–154], and only some papers report about simulations of the healing phase [155–158] or a comparison of the bone development in the early stage after implantation with animal experimental and/or histological data. Consequently, this extremely decisive phase of implant healing and bone ingrowth into the im-

plant surface has not yet been investigated biomechanically in detail. Strain Energy Density (SED), equivalent stress, and equivalent strain were used to predict bone remodeling around dental implants based on existing theories. The stress states of loaded implant-bone interfaces were analyzed before and after osseointegration using FEM. The results from this mechanical stimulus were then compared with in vivo data [159].

Furthermore, the effect of bone loss on mechanical responses was studied using FE models [160–162]. In another study, an alternative mathematical model is proposed for bone remodeling from Li et al. [146]. Li et al. described the change in bone density as a function of the mechanical stimulus. They developed a new bone remodeling algorithm by introducing an additional quadratic term using the theory of Weinans et al. [121]. The theory of Weinans simulates both, underload and overload resorption using the SED as the stimulus for bone remodeling. The algorithm of Li et al. [146] was applied in conjunction with FEM to simulate a dental implant treatment. The process of time-dependent bone adaptation was studied via computer simulations based on the implementation of remodeling theories on dental implants [148]. Lian et al. [163] proposed a new algorithm for bone remodeling based on existing theories [112, 121, 123, 126]. Two-dimensional FE models of implant and jaw bone were studied to demonstrate the ability of the proposed algorithm in predicting the density distribution of bone surrounding a dental implant. Lazy zone and SED parameters were used in this study. Besides, Eser et al. [164] studied bone remodeling around dental implants by applying the Stanford isotropic bone remodeling model. The aim of the study was focused on the influence of different designs of screw-shaped implants and predict the time-dependent changes in the cortical and trabecular bone around immediately loaded implants with different macro geometric designs by application of the Stanford theory which was defined by Beaupré et al. [14]. Also, Lin et al. [165] described a similar analysis of bone remodeling around dental implants. The purpose of the study was to show how bone remodeling increases the bone density in the peri-implant region. They used a mandible model with a trabecular bone body surrounded by a cortical shell of fixed thickness.

Hasan and her coworkers have analyzed the biomechanical FEA of small diameter and short dental implants. Both implant types were inserted in an idealized bone bed representing the anterior mandibular jaw region. Immediate loading conditions were applied to the models [149]. Furthermore, Hasan et al. aimed to predict the distribution of bone trabeculae, as a density change per unit volume around dental implants based on applying a selected

mathematical remodeling model. The apparent bone density change as a function of the mechanical stimulus was the base of the applied remodeling model that described disuse and overload bone resorption. A screw-shaped dental implant was tested with an FE model of an idealized bone segment. A sensitivity analysis with different parameters was performed as well [157]. Therefore, trabecular bone structure around dental implants has been simulated on a computer tomography (CT)-based FE model. In this study, CT images were used of a patient taken six years after the dental implant insertion [156].

Eser et al. worked with time-dependent bone remodeling theories around tissue and bone-level implants inserted in bone with reduced width [166]. Different Young's moduli of dental implants were used by application of the Stanford theory. Rungsiyakull et al. studied the bone remodeling responses of two different abutment configurations, implant-implant-supported versus tooth-implant-supported fixed partial dentures [167]. In this study, two 3D FE models were created based on computerized tomography data. As a mechanical stimulus for driving the bone remodeling, the SED induced by occlusal loading was used. Numerical simulation of bone remodeling around dental implants has been published by Ojeda et al. [168]. Several mathematical models [169–171] of bone remodeling are used to study the homogenized structural evolution of peri-implant bone. 3D FE models were used to study the influence of the diameter and length of dental implants made of pure titanium on their long-term stability. An "'error-driven"' algorithm was used by various groups to predict bone remodeling around dental implants [172, 173] and the stress, strain, or SED usually served as a mechanical stimulus. The main hypothesis for this algorithm is that higher mechanical load causes an increase in the amount of local bone where lower mechanical load leads to a decrease.

Bone remodeling under tooth loading was studied by Su et al. [174]. They aimed at developing a numerical algorithm to simulate bone remodeling activities under mechanical loading. 2D FE models were generated to calculate the strain/stress distribution in the alveolar bone under tooth loading. Regular chewing and biting forces were simulated using FEM in teeth and their surrounding tissues. A recent paper reported about biomechanical analysis of bone remodeling following mandibular reconstruction using fibula free flap. The purpose of the study was to evaluate the bone healing/remodeling activity in a reconstructed mandible and its influence on jaw biomechanics using CT data. FE analyses were conducted to quantify the bone mechanobiological stimuli. In this study, SED was defined as a mechanobiological stimulus

for the simulations [175].

Bone remodeling processes around dental implants during the healing period were simulated by Salih et al. They aimed to simulate the tissue behavior at the implant surface as a time-dependent function in response to local mechanical stimulus. In this study, 2D and 3D FE models were used to simulate classical bone remodeling theory under different loading conditions and different bone remodeling parameters [158].

1.4.6 Numerical Background of Bone Remodeling

Several scientists investigated the bone remodeling process mathematically in order to accurately predict bone resorption and formation [6, 57, 114]. In some situations, it is necessary that the internal mechanical stimulus in bone structure can be defined in terms of strains and stresses, for what the FEM is a useful tool [176]. Quantitative predictions of bone resorption and formation in bone structures can be made by combining the mathematical bone remodeling distributions involving FE models [109, 112, 119, 124, 177, 178]. Basically, these models are all based on the principle that bone remodeling is induced by a mechanical stimulus that activates the osteocytes. Furthermore, it is supposed that the bone has its own sensors to detect the mechanical stimulus and, depending on the magnitude of this mechanical stimulus, causes local bone adaptation. A generic mathematical expression can describe this procedure, using the apparent density as the characterization of internal morphology. The rate of change of apparent density of the bone structure with $\rho = \rho(x, y, z)$ at a particular location $d\rho/dt$, can be described as an objective function F, which depends on a specific stimulus at location (x, y, z). It is assumed that this mechanical stimulus is precisely comprehended with the local mechanical load in the bone structure and can be determined from the local stress tensor $\sigma(x, y, z)$, the local strain tensor $\varepsilon(x, y, z)$, and the apparent density $\rho = \rho(x, y, z)$:

$$\frac{d\rho}{dt} = F(\sigma, \varepsilon, \rho), \qquad 0 < \rho \leqslant \rho_{cb}, \qquad (1.4.1)$$

where ρ_{cb} is the maximal density of the considered material (cortical bone). When the objective function F reaches zero, the system is in equilibrium. The relationship between bone density change and mechanical stimulus was defined in the remodeling theory developed by Weinans et al. [121]:

$$\frac{d\rho}{dt} = B(S - k), \qquad 0 < \rho \leqslant \rho_{cb}, \qquad (1.4.2)$$

where B is a constant, $S = S(x, y, z)$ represents mechanical stimulus and $k = k(x, y, z)$ is the threshold value or simply a constant for the stimulus. When combined with a FE model, S is usually expressed per element. In that case, it is assumed that there is precisely one sensor point per element. Equation 1.4.2 signifies that the stimulus strives to become equal to the reference value k, which can either be site-specific [$k = k(x, y, z)$] or non-site-specific ($k = constant$) [121]. The relationship between the loading and the threshold value is described in equation 1.4.2. If the loading is below the threshold value, the density change will be negative. That means bone resorption will take place because of under-loading. On the contrary, if the loading is above the threshold value, the density change will be positive, which means bone growth will occur. The lazy zone is the range of stimulus within which no net bone remodeling takes place [112].

1.5 Bone Remodeling Theories

It is well known that mechanical loading plays an important role in bone remodeling in both cortical and spongious bone. Numerous researchers have been encouraged to propose mathematical models for the bone remodeling process based on Wolff's Law [13]. Wollf indicated that there is a direct mathematical relationship between skeletal loads and bone shape. Wolff's composite illustration shows trabecular arches in a diagrammatic drawing of a human femur in 1870 [179], see Fig. 1.14.

Bone adapts its shape and/or its internal remodeling [20]. Frost developed the mechanostat theory to explain bone remodeling with mathematical theory, which was a starting idea for current mathematical theories [34]. An adaptive elasticity theory was developed by Cowin and Hegedus [6, 116]. This theory considered strain as a mechanical stimulus to initiate the bone remodeling process. Huiskes and his coworkers used a similar approach using the SED as the mechanical stimulus [112]. The driving force for adaptation of the apparent density would be the difference between actual and reference SED at the same location. Consequently, in equation 1.4.2, $S = S(x, y, z)$ and $k = k(x, y, z)$ would be the actual SED and the reference SED, respectively. For more information the normal stimulus distribution $k = k(x, y, z)$ must be known or be determined from a normal equilibrium density distribution, to predict the bone adaptation process to an abnormal situation [121]. Bone was assumed to be an isotropic linear elastic material in most of these approaches. There are just a few papers that have worked with bone material as an anisotropic material [181–183].
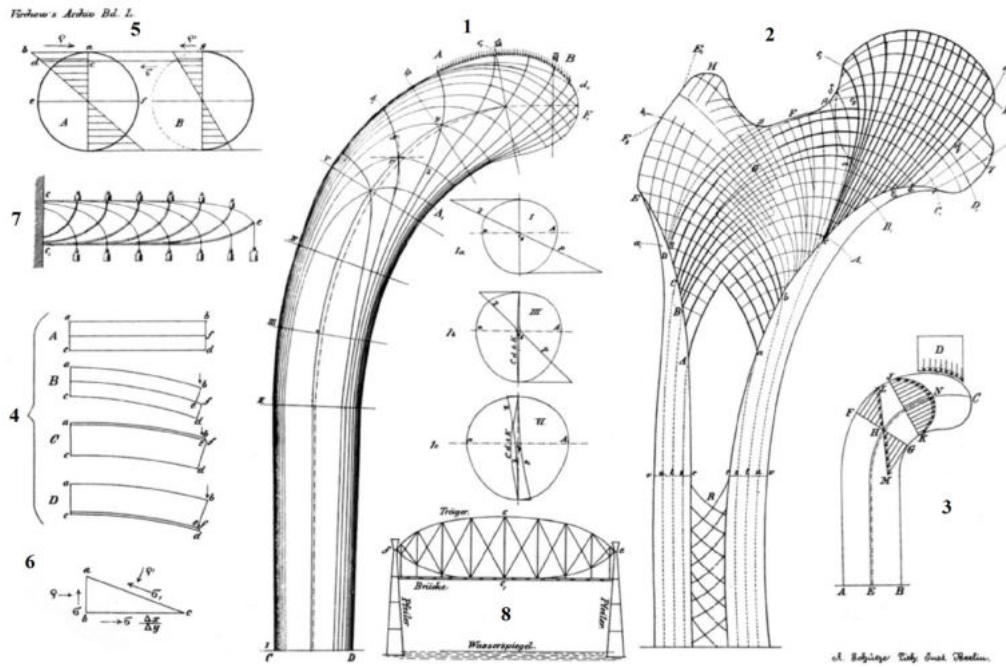
Figure 1.14: Wolff's composite diagram including eight figures which include reproductions of Culmann's cantilevered beam and 'crane'. Wolff obtained most of the structures (i.e., drawing of the 'crane') from Culmann in 1870 and 1892. Fig. 1. Illustration of forces and trajectories that act on the interior of a bone. The students made the original drawing of Professor Culmann under his supervision. Fig. 2. Schematic reproduction of human femur. Fig. 3-7 These five figures are related to the explanation of the 'graphical static' method. Fig. 8. Schematic illustration of a bridge built with stress-carrying structural members (image adapted from [180]).

1.5.1 Micro-Damage of Bone Remodeling

A semi-mechanistic model for bone remodeling was introduced by Huiskes et al. in 2000 [133] which included the experimental findings in bone cell physiology [184], such as a separate description of osteoblastic formation and osteoclastic resorption [185], a mechanosensory system from osteocytes [186, 187], and role of micro damage [188]. Nowadays, several bone remodeling theories considered both, microdamage and mechanical loads [189]. Firstly, microdamage was described by Frost [190]. Fatigue loading increases microdamage which activates bone remodeling and osteocyte apoptosis [191]. Like any structure that can withstand repeated stress, bone also suffers microdamage, which can impair its mechanical competence. However, in contrast to inert materials, biologically active bone can recognize and counteract the

development of microdamage. It is assumed that human supporting bone, such as the tibia, would break in only three years of normal stress [192] without such a mechanism of material repair. The microdamage formation itself contributes to the toughness of the bone by shielding the crack tip. Some microdamage studies showed that too much in vivo cracks propagate during in vitro fatigue loading [193]. The role of microdamage of trabecular bone is less studied until now. Zilch et al. showed that bovine trabecular bone has fatigue and creep characteristics similar to human cortical bone [194]. More data into crack growth mechanisms in trabecular bone is required, because of the correlations with the mechanism of cortical bone.

1.5.2 Internal and External Remodeling

Julius Wolff showed: Every change in the function of bone is followed by specific, definite changes in internal architecture and external conformation in accordance with mathematical laws [13]. The adaptation between bone tissue and bone density is called interior remodeling (spongy bone). External remodeling (cortical bone) is the apposition of bone tissue on the surface of the bone. That's why external remodeling is known as surface remodeling. In 1964, Frost proposed that internal and external remodeling should be differentiated [20]. Cowin et al. and Huiskes et al. separated internal and external remodeling. Strains were used as a mechanical stimulus by Cowin et al. [16]. On the other hand, Huiskes et al. regarded the SED as the signal that controls bone remodeling [112].

1.5.3 Cowin and Hegedus' Adaptive Elasticity Theory

In 1976, the theory of 'adaptive elasticity' was developed by Cowin and Hegedus. Following a suggestion by Frost [20], Cowin et al. separately modelled the internal and external remodeling using the following equations which were developed to explain the remodeling behavior of cortical bone. It is supposed that cortical bone has site-specific natural or homeostatic equilibrium strain state. The elastic modulus which is related to density was formulated to change in agreement with:

$$\frac{dE}{dt} = A_{ij}(e_{ij} - e_{ij}^{\circ}),$$

(1.5.1)

where e_{ij} is the actual strain tensor, e_{ij}° is the equilibrium strain tensor, E is the local modulus of elasticity, and A_{ij} is the matrix of remodeling coefficients. The strain state at the periosteal and endosteal surfaces simulated that the bone was assumed to add or remove material on those surfaces, in agreement with:

$$\frac{dX}{dt} = B_{ij}(e_{ij} - e_{ij}^{\circ}), \tag{1.5.2}$$

where B_{ij} is again a remodeling coefficient and X is a characteristic surface coordinate perpendicular to the surface [112]. Hart et al. used a 3D computational model based on FEM to determine the remodeling shape both on the endosteal and periosteal surfaces [124, 195, 196]. Cowin et al. used the strain tensor as the mechanical stimulus for bone remodeling [16, 197]. Later on, they used the theory of external remodeling to simulate animal experiments and found agreement between animal experimental results and theoretical predictions.

1.5.4 Strain Energy Density Theory by Huiskes et al.

The theory from Cowin et al. [6] was extended by Huiskes et al. [112] with two main differences. They added a lazy zone, which was proposed by Carter [198]. The lazy zone effect was suggested based on experimental investigation. Later on, this effect used to become an essential factor from other researchers in the simulation of the bone remodeling process.

The "'lazy zone"' describes that the bone has no net density change, and is defined as $\frac{U}{\rho}$. Additionally, SED U $[J/mm^3]$ was used in their remodeling equation as the mechanical signal. The SED is the strain energy per unit volume:

$$SED = \frac{U}{\rho} \tag{1.5.3}$$

The SED can be calculated as [159, 199]:

$$U = \frac{1}{2}\varepsilon\sigma, \tag{1.5.4}$$

where U is the SED, ε is the strain tensor, and σ is the stress tensor of the bone tissue. Cowin [200] and Rouhi [201] defined that the use of the strain tensor as mechanical stimulus for remodeling makes it difficult to determine the remodeling rate coefficients. With the purpose to determine the remodeling rate coefficient, Huiskes et al. [112] recommended the SED, a scalar quantity, as a suitable mechanical signal for both, external and internal remodeling. Considering the external remodeling, the bone can either add material or remove material according to:

$$\frac{dX}{dt} = C_x(U - U^*), \tag{1.5.5}$$

where $\frac{dX}{dt}$ is the rate of surface growth of bone, C_x is the remodeling rate coefficient, U is the SED, U^* is the equilibrium value of SED that determines the boundary between bone resorption and formation. On the other hand, for internal remodeling the bone could adapt its density value, that means there will be changes in bone apparent density. By this, assuming that the elastic modulus relates to the apparent density one can write:

$$\frac{dE}{dt} = C_e(U - U^*), \qquad (1.5.6)$$

where $\frac{dE}{dt}$ is the rate of change of elastic modulus, E is the local elastic modulus, C_e is a proportionality constant. These both equations 1.5.5, 1.5.6 can be transformed into finite difference formulations as follows. For external remodeling:

$$\Delta X = \Delta t C_x(U^i(t) - U_m^i) \qquad i = 1, m, \qquad (1.5.7)$$

where ΔX is the growth of the surface nodal point normal to the surface, m is the number of surface nodal points considered, Δt is the period of one time step, and C_x is a constant to determine the external remodeling rate.

For internal remodeling:

$$\Delta E = \Delta t C_e(U^i(t) - U_n^i) \qquad i = 1, n, \qquad (1.5.8)$$

where ΔE is the change in the elastic modulus in one time step, n is the number of elements for internal remodeling, Δt is the period of one time step, and C_e is a constant to determine the internal remodeling rate.

Concept of a lazy zone proposed by Carter [198]: Carter defined that bone is 'lazy' in terms of reacting to mechanical stimulus. This concept occurs out of the bone resorption and formation, see figure 1.15. The idea of 'lazy zone' means that there are thresholds to be exceeded before bone adaptation can occur (figure 1.15). Huiskes et al. used the concept of the lazy zone in their model [112]. The Huiskes model was able to express bone adaptation on a macroscopic level [135]. This theory was successfully applied to evaluate bone adaptation in 3D femur models after implantation of hip arthroplasty. The FE models were constructed from an animal experiment.

Additionally, Huiskes et al. suggested a new theory to explain bone remodeling, a semi-mechanistic bone remodeling theory, which includes spongy bone remodeling. This semi-mechanistic spongy bone remodeling theory is depicted as a coupling process of bone formation, and resorption on the bone surfaces [133].
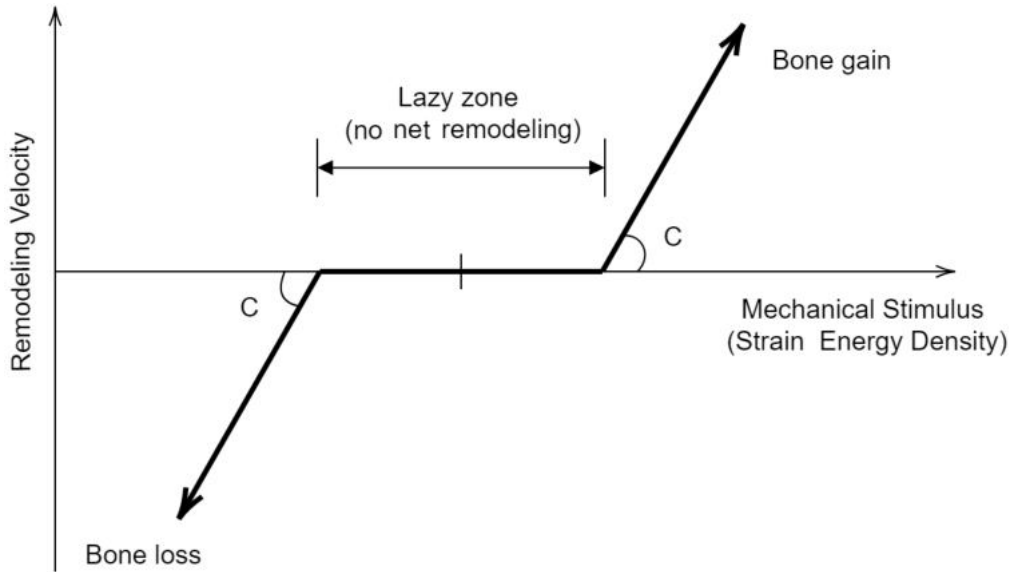
Figure 1.15: The assumed, local bone adaptation as a function of SED with lazy zone effect (adapted from [112]). There is no adaptive response in the lazy zone.

1.5.5 Stanford Theory

The theory of Beaupré and Carter [14], the so-called Stanford theory, was selected as the mathematical model for bone remodeling around implants. A daily stress stimulus is used as a mechanical stimulus in this theory. In 1989, Carter et al. worked with the proximal human femur and 2D FEM. The work aimed to solve the distribution of bone morphology and to consider the bone as an initially isotropic, inhomogeneous structure in which the apparent density and modulus could subsequently vary as a function of position as their computer programs remodeled the bone [119]. The Young's modulus E was calculated as a power function of the apparent density ρ since the bone apparent density changes during the bone remodeling as given by Carter and Hayes [202]:

$$E = 3,790\,\rho^3. \tag{1.5.9}$$

The equation 1.5.9 is used for spongy and cortical bone, as the bone remodeling takes place on bone surfaces of marrow/voids in cancellous bone and Haversian canals in cortical bone [14]. The new elastic modulus can be calculated for each step by using the equation 1.5.9.

Carter and coworkers expanded the single-load approach for predicting bone density to include the history of multiple loading of bone over time. Stress magnitudes or cyclic SED and the number of loading cycles are identified for bone loading histories for an average day. Multiple loading conditions were used with FE models as there is no single loading condition that can be reasonably excepted to be the stimulus for the full trabecular architecture. The theory described in their previous work in 1987 [118] was used. That theory considered a relationship between element density and an effective stress. The study hypothesized that the apparent local density of cancellous bone could be approximated by the relationship [119]:

$$\rho = K \left(\sum_{i=1}^{c} n_i \sigma_i^M \right)^{(1/2M)}, \qquad (1.5.10)$$

where the daily loading history has been summarized as K and M which are constants, c is the number of discrete loading conditions, n is the number of loading cycles, σ continuum model cyclic peak effective stress (scalar quantity) which is the energy stress, and ρ the bone apparent density defined as:

$$\sigma_{energy} = \sqrt{2E_{avg}U}, \qquad (1.5.11)$$

where U is the continuum model SED, and E is the continuum model elastic modulus. In the proximal femur, the distributions of calculated density are similar. Defining the remodeling rate was done as the variation in density as a function of effective stress. A lazy zone was also added in the equation system of Carter et al. in 1987 [118]. Weinans and coworkers also used the Stanford theory in 1992. They applied this theory to a 2D FEM of a proximal femur. Because of mechanical stimulation, the bone was represented as a continuum, capable of adapting its apparent density [121]. The Stanford theory was used in all these studies in long bones.

1.6   Bone Density

Bone density is a key factor for a successful long term implant treatment. The bone quality in dentistry typically is defined in four classes [203]:

- Quality 1: This consists of primarily dense cortical bone. It is located in the anterior mandible.

- Quality 2: The quality of this part has a thick cortical bone that surrounds a core of dense cancellous bone. It is associated with the posterior mandible.

- Quality 3: This consists of a thin layer of cortical bone, which also surrounds a core of dense cancellous bone, and it is usually associated with the anterior maxilla.

- Quality 4: This consists of a thin layer of cortical bone that surrounds a core of lower density cancellous bone.

These four classifications have been used in treatments for implant placement. Later on, some other researchers have proposed an extension of this idea by comparing the surgical resistance of the bone during osteotomy preparation [204–207]. It is consensus that titanium dental implants have a high success rate by both the quality and quantity of available bone in the long-term [208–211]. Some parameters can affect the modeling and remodeling as the direction, magnitude, and repetition rate of biomechanical quantities. Bone has the ability to resist immediate loading, and bone quality is increased under repetitive forces. Density can increase when the simulation is within the physiological limits, it may generate an increase in osseous density at the implant-bone interface [198, 212–215]. The spread and the distribution of contacts are the advantages of immediately loaded implant systems during the first days and weeks after immediate/early loading. The distribution of force to all abutments can be affected by the rigid splinting of the prosthesis. Computer tomography can be used for bone quality assessment before surgery using Housfield unity [216, 217]. The bone mineral density (BMD) can be measured with quantitative computer tomography images from cortical and spongy bone separately [218]. However, the position of implant can not find during the process of measuring the BMD since BMD values vary locally to a high extent [219].

1.7 Bone Healing Process

Bone fracture happens mostly from physical trauma. The inflammatory phase, the soft callus phase, the hard callus phase, and the remodeling phase are the four overlapping phases of the regeneration process of fractured bone [220]. The initial bone healing stage is starting with the process which turns from cortical bone, periosteum, and surrounding soft tissues, and rupturing numerous blood vessels [221]. Growth factors affect the healing process into the regeneration area from the surrounding tissues [220]. Not only growth factors but also a variety of other factors, including the mechanical and the biological environment affect bone healing. After the bone has healed and undergone remodeling, the fracture area will have returned to the pre-injury condition.

Bone forming and regenerative processes are similar principles as bone fracture healing. Some examples of these processes are, e.g., bone tissue engineering, limb lengthening, bone ingrowth on implants, and long bone growth during fetal development. Some research groups approved that mechanical stimulation can activate fracture healing [222, 223]. Nevertheless, it is still unknown how the mechanical signals are transferred into a biological response.

Computer modeling has a significant influence on mechanobiology [224]. Computational models are useful to calculate the relationship between global mechanical loads and the local stresses and strains that influence tissue formation. Mathematical models are favorable to simulate the complex systems as many biological processes, including bone healing, are complicated, either too time-consuming, too expensive, or impossible. Computational models are used with both in vivo and in vitro experiments to explain the effect of mechanical stimulus on cells and tissue differentiation, growth, adaptation, and maintenance of bone [225]. Augat et al. studied with shear movements at the fracture site the result in healing with decreased external callus formation [226]. In vivo experimental models have been used to investigate the effect of mechanical loading during bone healing [227]. Strain, stability, pressure, and fluid velocity are salient parameters that react as stimuli for tissue formation during fracture healing [228].

Bone healing has two forms called primary and secondary healing.

1.7.1 Primary Bone Healing

Primary healing is also called as direct healing or intramembranous bone formation. There is no callus formation during the primary healing. It can occur either with a small gap or direct contact of the fractured compact bone ends. The primary bone healing is a slow process that takes a few months to a few years until the process ends. The gap of the fracture is a critical point. The osteoblast cells fill the fracture gap, if the fracture gap is between $800\,\mu m$ and $1\,mm$. Two bone fragments are connected directly by osteoblasts and osteoclasts [229].

1.7.2 Secondary Bone Healing

Secondary fracture healing is known as indirect fracture healing, which is the most common form of bone healing. The secondary healing process is a natural process that occurs in the presence of some interfragmentary

movement between the fractured bone ends. It includes a consecutive tissue differentiation process as shown in figure 1.16 [230]. Four overlapping stages consist of sequentially inflammation, soft callus tissue, hard callus tissue, and remodeling (resorption of the callus) [231, 232].
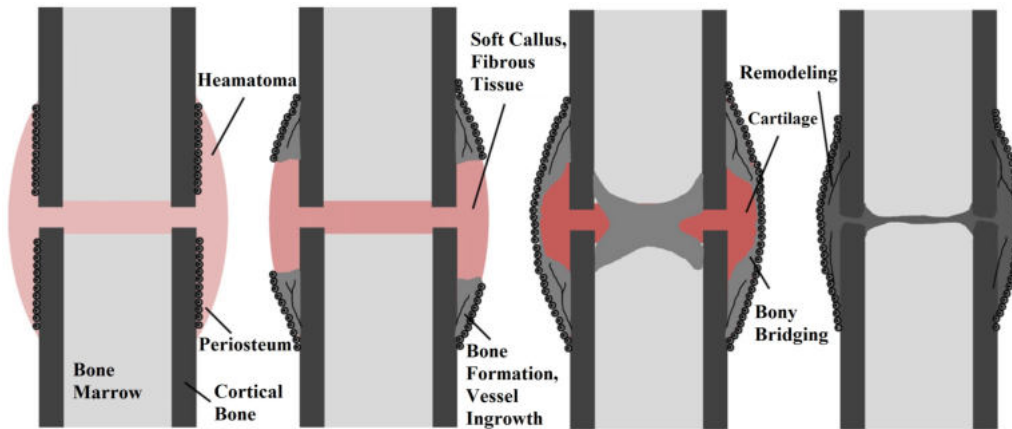
Figure 1.16: Some sequential processes happen during the secondary healing: an initial heamatoma, soft callus formation, hard callus formation, external bony bridging, and bone remodeling (left to right, modified after [228]).

1.7.3 Bone Healing around Dental Implants

Branemark and coworkers have suggested a direct relationship between implant and bone and introduced the term of osseointegration in 1977 [233]. The interface between bone and implant covered with a clot form, blood, and inflammatory cells [234]. Osteoclast cells remove the damaged bone, and new bone is formed on top of the bone by osteoblast cells.

1.7.4 Osseointegration

The implant can be integrated with the bone when it is inserted into the jawbone. This direct contact between implant and bone is defined as osseointegration after an implant was inserted into the bone. If the primary stability is not achieved and the implant moves during integration, then bone can repair with a fibrous capsule around it [235]. If fibrous tissue is formed around the implant, osseointegration is not possible, and the anchorage is then not sufficient for the prostheses to function like a regular tooth. The type and quantity of bone affects the primary stability at the implant site [235, 236].

1.8 Dental Implant Design

Many factors can affect implant failure, e.g., the implant, abutment, or dental prosthesis, the patient may not be satisfied with the result, or it might not have been inserted adequately [237]. In case the osseointegration is lost, a so far successfully osseointegrated implant can fail too. When the bone quality or volume in the area is not sufficient to bear the occlusal load, the osseointegrated implant fails [238]. Smoking and the age of the patient are also risk factors for bone. The diameter and length of implants are major critical factors for the long term implant stability. The diameter of the implant may vary between 1.8 and 6.5 mm. The optimum diameter can be used according to the bone quality and the location in the jaw, i.e., the mastication force. On the other side, the length of the dental implant is 10.00 mm or longer; nevertheless, shorter implants can also be used depending on the anatomical structures. An inferior prognosis is seeable with shorter implants [239]. There are different implants with different screw designs in the dental sector. These different implant designs exist to raise the fixture stability and encourage osseointegration [240].

2 MATERIALS AND METHODS

2.1 Investigation of Implants

The scope of this thesis was to develop theoretical models to define a bone remodeling theory for the early healing phase of dental implants. The theory is based on work of Li et al. [146]. The work program of the project part applied here consists of theoretical studies and FE simulations, as well as numerical biomechanical investigations. In this chapter, different 2D and 3D implant models used to investigate the bone remodeling process around dental implants with and without osseointegration are presented. All numerical simulations were run in the Marc Mentat FE software from MSC. The bone remodeling algorithm was developed in 'C++' programming language and by special subroutines implemented in Marc Mentat.

2.1.1 Geometry of 2D Implants

The basic 2D FE implant models without screw pitches were developed to quantify changes in bone loading conditions by forces at the beginning of the research. Later on, screw pitches were added to the implant models (figure 2.1). The diameter and length of implants were varied to find the standard dimensions for bone remodeling theory in our FE models with ø=3 mm and L=11 mm. The material properties of implants are defined as titanium (table 2.1).

2.1.2 Geometry of 3D Implants

Different commercial dental implants were used for the 3D models in this research. *tioLogic*© ST and Dentaurum CITO mini®dental implants were used, which are shown in figure 2.2. The dimensions of the *tioLogic*© ST implant were ø=3.7 mm and L=13 mm, and ø=2.2 mm and L=15 mm for the mini implant.

Material	Young's modulus (MPa)	Poisson's ratio
Titanium alloy	110,000	0.30

Table 2.1: Material properties of 2D and 3D implants.
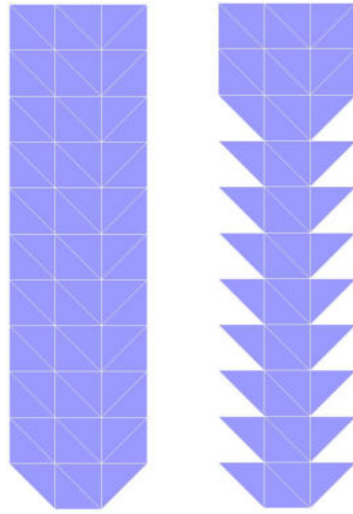
Figure 2.1: Two different basic 2D FE implant models were developed with and without screw pitches.
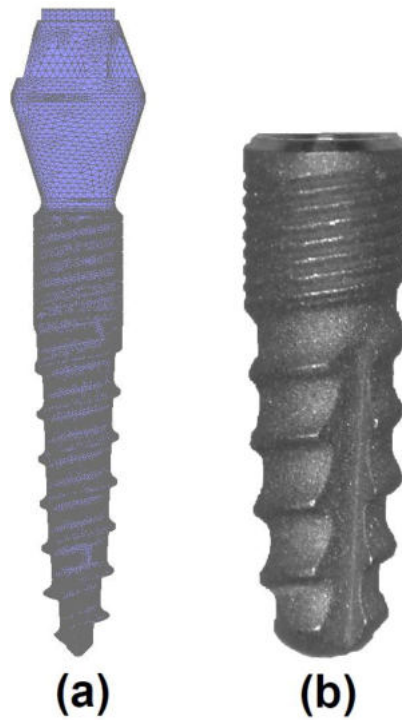
Figure 2.2: 3D implant designs: (a) Dentaurum CITO mini®dental implant and (b) *tioLogic*© ST.

2.2 Bone Remodeling Theory

Some numerical background for remodeling will be given in this section. The theory aimed to investigate the response of the bone around dental implants in fully or non osseointegrated cases. Various boundary conditions, different cortical and spongious bone material properties, loading magnitudes and directions, bone quality, and different implant designs are used during all simulations. After that, different tissue types with different thicknesses in the simulations were tested to simulate different osseointegration phases.

2.2.1 Bone Remodeling Basics

When a mechanical load is applied to a bony structure, the bone responds to this load and is remodeled depending on the magnitude of this load. This remodeling process can change the density of the existing bone and/or change the geometry of the bone.

C++ programming language is used to write the codes to formulate the bone remodeling theory of Li et al. [146]. The change of bone density is considered in these codes. In the following text, ρ denotes the local bone density. For cortical bone $\mathbf{0} < \rho \leqslant \rho_{\mathbf{cb}}$ will be assumed, where $\rho_{\mathbf{cb}}$ is the maximum density of cortical bone ($\rho = 1.74\,gcm^{-3}$). Later this bone remodeling model will be expanded to also contain remodeling processes during the osseointegration phase of dental implants. For this case, above assumptions on the limits of bone density have to be slightly adapted. For the different tissue types that are evolving during the osseointegration, $\mathbf{0} < \rho \leqslant \rho_{\mathbf{tt}}$ will be assumed, where $\rho_{\mathbf{tt}}$ is the maximum density of current tissue type.

This C++ code is mainly based on the bone remodeling model developed by Li et al. [146] and extended by Hasan et al. [149, 240]. They calculated the density change over time as a function of SED $\mathbf{U}$ within the bone and the current local density ρ:

$$\frac{d\rho}{dt} = f(U, \rho) = B(\frac{U}{\rho} - k) - D(\frac{U}{\rho} - k)^2, \tag{2.2.1}$$

where $\mathbf{B}$ and $\mathbf{D}$ are constants, $\mathbf{U}/\rho$ is the mechanical daily stimulus, $\mathbf{k}$ is the threshold value for the stimulus and $\rho_{\mathbf{c}}\mathbf{b}$ is the ideal density of bone without porosity. Li et al. aimed at expressing the SED $\mathbf{U}$ as a function of the stress σ. For uni-axial loading, the SED $\mathbf{U}$ can be expressed as $\mathbf{U} = \sigma\epsilon/\mathbf{2}$,

which in turn can be expanded to $U = \sigma^2/2E$ using $\sigma = E\epsilon$, where E is Young's modulus of the given material. Using this in the above formula results in:

$$\frac{d\rho}{dt} = f(\sigma, \rho) = B(\frac{\sigma^2}{2E\rho^2} - k) - D(\frac{\sigma^2}{2E\rho^2} - k)^2. \tag{2.2.2}$$

Several approaches have been made to describe Young's modulus E of bone as a function of the bone density ρ. While Li et al. [146] used a relationship formulated by Carter and Hayes [202], we will stick to a more general approach by simply using $E = E(\rho)$:

$$\frac{d\rho}{dt} = f(\sigma, \rho) = B(\frac{\sigma^2}{2E(\rho)\rho^2} - k) - D(\frac{\sigma^2}{2E(\rho)\rho^2} - k)^2. \tag{2.2.3}$$

This formula 2.2.3 is implemented in the function which calculates the density change based on the current density and mechanical stimulus. This function implements the two differential equations 2.2.4 and 2.2.5 from [146];

$$\frac{d\rho}{dt} = f(\sigma, \rho), \tag{2.2.4}$$

$$\frac{d\rho}{dt} = f(U, \rho), \tag{2.2.5}$$

both extended to include a 'dead zone' surrounding k, in which no bone remodeling takes place. The Euler method can be used to solve this differential equation numerically;

$$\rho_{n+1}^* = \rho_n + \Delta t f(\sigma, \rho_n), \tag{2.2.6}$$

$$\rho_{n+1} = \rho_n + \frac{\Delta t}{2}[f(\sigma, \rho_n) + f(\sigma, \rho_{n+1}^*)]. \tag{2.2.7}$$

The same approach can be used if the density change is expressed directly as a function of the SED using the function $f(U, \rho)$. The iterative process for the Euler method is implemented in the function, which calculates the density change. σ is the equivalent stress in the element, ρ is the current density in the element. As a time step Δt was selected.

2.2.2 The 'lazy' or 'dead' Zone

Several authors suggested that a certain amount in over- or underloading must be exceeded before the bone remodeling occurs. The loading area between these threshold levels is often referred to as the 'lazy zone' or 'dead zone' [112, 146, 198]. While the basic idea to implement such a dead zone is straight forward, there are some implementation details that have to be considered. The current implementation in which calculation of the density change is based on the current density and mechanical stimulus, uses the following non-continuous approach (where **w** is half of the width of the dead zone):

$$
\frac{d\rho}{dt} = \begin{cases} 0 & \text{if} \quad \frac{U}{\rho} \in [(1-w)k, (1+w)k] \\ & \text{and} \\ B(\frac{U}{\rho^2} - k) - D(\frac{U}{\rho} - k)^2 & \text{otherwise} \end{cases} \qquad (2.2.8)
$$

Alternative approaches would shift parts of the function $\frac{d\rho}{dt}$ horizontally to the left or the right below or above the dead zone, respectively (which would change the roots of the function) or use a modified function which retains the roots. Further investigations have been performed to determine the influence of these different approaches to the final bone distribution. Hasan et al. [241] extended the theory from Li [146] with the dead zone. Figure 2.3 shows the bone density change over time against mechanical stimulus U/ρ.
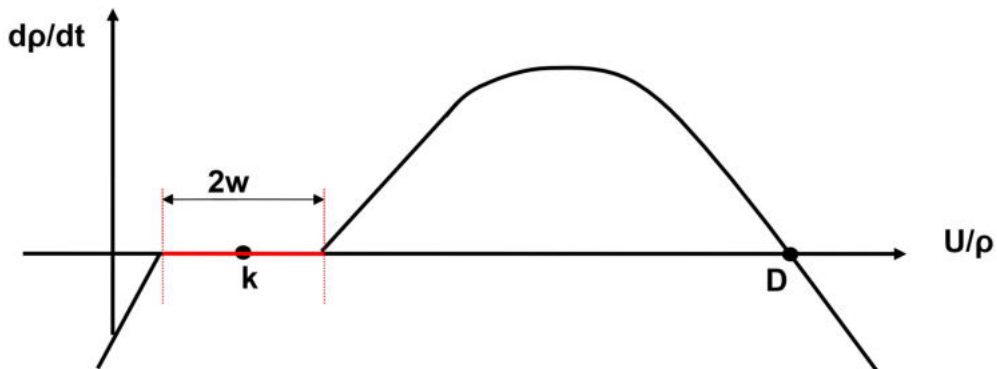
Figure 2.3: Schematic representation of the functional dependency between the current stimulus U/ρ and the resulting density change in the bone, with permission from [241].

2.2.3 Relationship between Bone Density and Elasticity

Several papers propagate a functional relationship between the density ρ of the bone and it's Young's modulus $\mathbf{E}$. This relationship is used in different places, some are obvious like calculating density changes, some are less obvious. For example, calculating the remodeling parameters $\mathbf{k}$, $\mathbf{B}$ and $\mathbf{D}$ from some clinically observed (or derived) stress or strain values requires to calculate the density from Young's modulus and vice versa. Carter and Hayes [202] formulated the relationship as:

$$E(\rho) = C\rho^3, \quad with \quad C = 3790\, MPa(gcm^{-3})^{-3}. \tag{2.2.9}$$

Beaupré and coworkers [14] defined this 2.2.9 relationship as:

$$E(\rho) = \left\{ \begin{array}{ll} 2014\rho^{2.5} & if \quad \rho \leq 1.2, \\ 1736\rho^{3.2} & \text{otherwise} \end{array} \right\} \tag{2.2.10}$$

Weinans and his coworkers [242] defined:

$$E(\rho) = \left\{ \begin{array}{llll} 1353\rho^{1.48} & if & 0.0 \leq \rho \leq 1.4\ gcm^{-3}, \\ 34623\rho - 46246 & if & 1.4 \leq \rho \leq 2.0\ gcm^{-3}, \end{array} \right\} \tag{2.2.11}$$

The two functions which convert Young's modulus into the bone density and convert the bone density into Young's modulus are currently implemented in the model proposed by Carter and Hayes [202].

2.2.4 Tissue Types

To be able to describe the osseointegration process, the remodeling of different tissue types have to be considered. All tissue types are assigned in the FE model in this way. Four different tissue types are distinguished during remodeling:

- stiff callus (SC), i.e. cortical bone,

- connective tissue (CT), i.e., blood, bone marrow and bone fragments directly after insertion of the implant,

- soft callus (SOC) and

- intermediate soft callus (MSC).

The healing phases are shown in figure 2.4. Three different stages occur during the healing periods with the different tissue types.
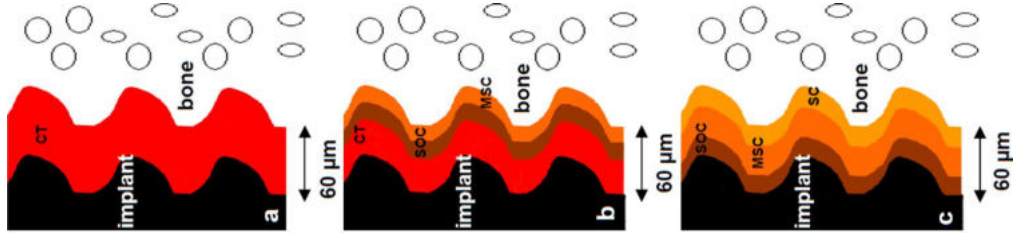
Figure 2.4: Histologically, osseointegration consists of three phases of different tissue states: a) Immediately after implant insertion to two weeks: haematoma, connective tissue (CT). b) After two months: intermediate stiff callus (MSC), soft callus (SOC), connective tissue (CT). c) After four months: stiff callus (SC), intermediate stiff callus (MSC), soft callus (SOC).

2.2.5 Remodeling Parameters

The remodeling parameters $\mathbf{k}$, $\mathbf{B}$ and $\mathbf{D}$ are functions of the critical stresses (or strains) and the maximum density of each of the tissue types. As the density is used to determine the maximum Young's modulus of each type, the final values of these parameters depend on the exact functional dependency between density and Young's modulus as well. The two roots of the density change function $\frac{\mathbf{d}\rho}{\mathbf{dt}}$ are $\mathbf{k}$ and $\mathbf{B}/\mathbf{D} + \mathbf{k}$. In 1992, Weinans et al. [242] used 0.01 gcm^{-3} and 1.74 gcm^{-3} as lower and upper limits of the density, respectively. They derived the upper limit by using the inverse function to the formula $E(\rho) = C\rho^3$ [202] with a maximum Young's modulus of 20,000 GPa. The dead zone is an area around the daily stimulus $\mathbf{k}$ in which no remodeling occurs. This area is defined as the range $[(\mathbf{1} - \mathbf{w})\mathbf{k}, (\mathbf{1} + \mathbf{w})\mathbf{k}]$, where $\mathbf{w}$ is half of the width of the dead zone.

At the lower critical stress and the upper critical stress, bone density does not change. The lower critical stress is defined as $\sigma_{\mathbf{1}}$ to calculate the constant $\mathbf{k}$:

$$|k^*| = \frac{\sigma_1{}^2}{2C\rho_{cb}^4}, \qquad (2.2.12)$$

and to calculate the constant $\mathbf{D}$ with the upper critical stress $\sigma_{\mathbf{2}}$:

$$|k^*| = \frac{2C\rho_{cb}^4 B}{\sigma_2^2 - 2C\rho_{cb}^4 k^*}. \qquad (2.2.13)$$

Different remodeling parameters from different tissue types are shown in table 2.2.

Tissue Types	B	k	D	w	dt	n_{max}	ρ_{max}	ρ_{min}
SC	1.0	0.0001	55.0	0.2	3.0	100000	1.74	0.1
CT	1.0	0.0000004	55.0	0.2	1.0	100000	0.07	0.01
SOC	1.0	0.00002	55.0	0.2	1.0	100000	0.75	0.01
MSC	1.0	0.00008	55.0	0.2	1.0	100000	1.4	0.01

Table 2.2: Remodeling parameters of the different tissue types.

2.2.6 Flow Chart Diagram for the Bone Remodeling

The work package of the study, which includes C++ codes and FE simulations for the algorithm of bone remodeling, is illustrated in Figure 2.5.

We first need to define and design the initial geometry, the external loads, material properties, and the other boundary conditions for FE analysis. The bone remodeling algorithm then consists first of a loop over the load increments in time steps. The scaling factor is a variable to control the amount of density change per iteration. If the calculated density change is taken into account at full scale, the differences between two iterations may be too drastic. But the clinical situation corresponds to a gradual change of the bone density, as even a small change in the density distribution changes the distribution of strains and stresses within the anatomical structures, which in turn control the ongoing remodeling. Different scaling factors were used in the study, which are shown in table 2.3. The critical scaling factor is that factor, at which the resulting maximum possible density change is too small to move the current element from its current material group into an adjacent material group. The maximum possible density change is:

$$\text{critical scaling factor} = +/-(\text{scaling factor}*\rho_{max}tissuetype).$$

Scaling Factor:	0.01	0.05	0.1	0.2	0.33	0.5

Table 2.3: Scaling factors used in the study.
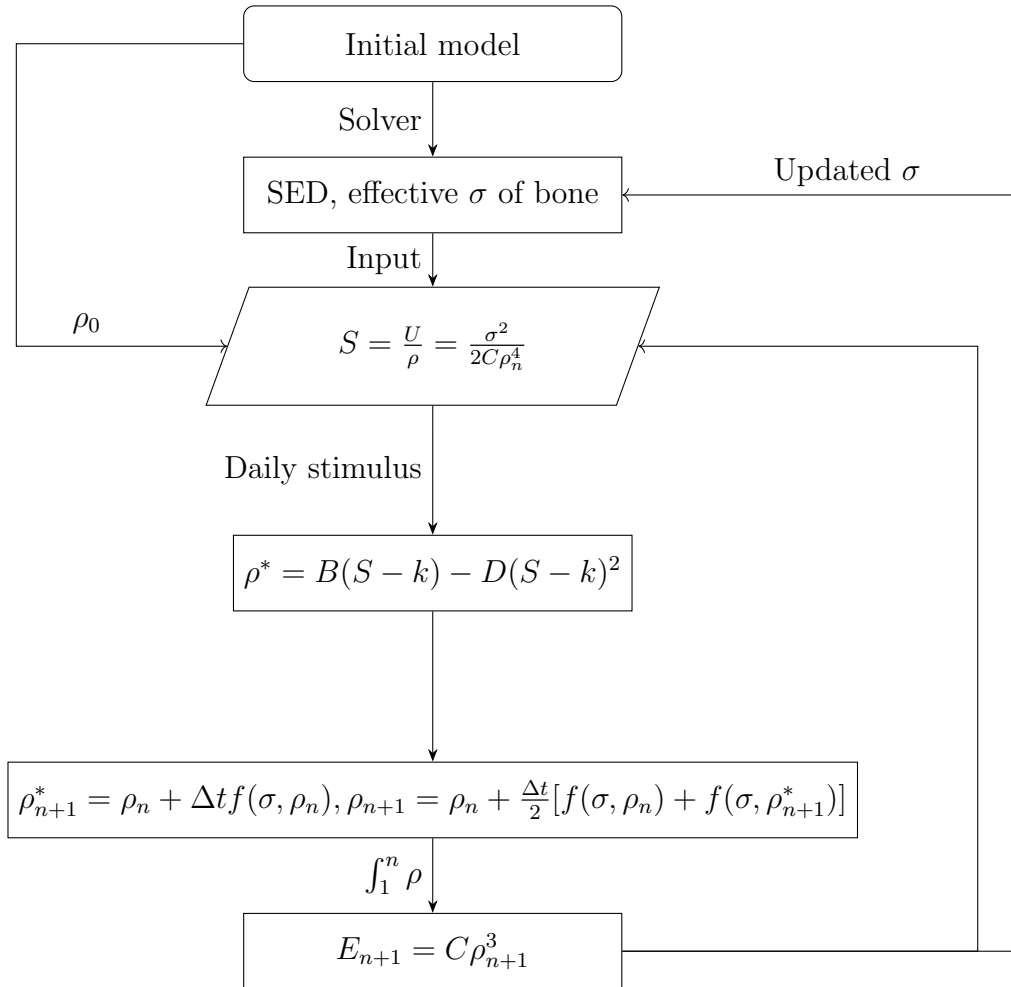
Figure 2.5: Outline of the algorithm of bone remodeling used in FE analyses. Adapted from [240].

2.3 2D and 3D Models for Bone Remodeling Simulation

At the beginning of the study, the basic model was created with a basic dental implant in the FE software. The aim of developing a basic 2D model was to quantify the optimal boundary conditions for the later simulations of bone remodeling and osseointegration phases. The proposed 2D model consists of cortical bone, spongy bone, and implant. The reason for no periodontal ligament (PDL) is that there is no PDL after implant insertion into the bone. All material properties of analysis are presented in table 2.4.

Material	Young's modulus (MPa)	Poissonfls ratio
Implant	110,000	0.30
Cortical bone	18,000	0.30
Spongious bone	1,000	0.30

Table 2.4: Material properties of basic 2D FE models.

2.3.1 Sensitivity Tests with 2D Models

The mathematical model for bone remodeling was implemented into the FE package using 2D models. Different sensitivity tests were simulated in this section.

2.3.1.1 Influence of the Spongious Bone Stiffness

The definition of the material properties of elements in the model is shown in figure 2.6, where each color refers to different material properties in the model. Blue, dark brown, and cream colors are showing implant, cortical bone, and spongy bone, respectively. The boundary conditions are shown in figure 2.6. Total force was applied directly to the implant with 100 N, as shown in the figure 2.6.

The fixation was done from both sides of the model. The FE mesh consisted of a triangular element class. The triangular element used in this study was type 6, class 3 in the commercial FE software MSC.Marc/Mentat library. This triangular class has three nodes for plane strain applications, where geometry is more complicated. The whole model consisted of 359 nodes and 640 elements. The implant was modeled without pitches in the basic model. Different Young's modulus of spongious bone was used in the simulations of 1 MPa, 10 MPa, 100 MPa, 125 MPa, 130 MPa, 140 MPa, 150 MPa, 175
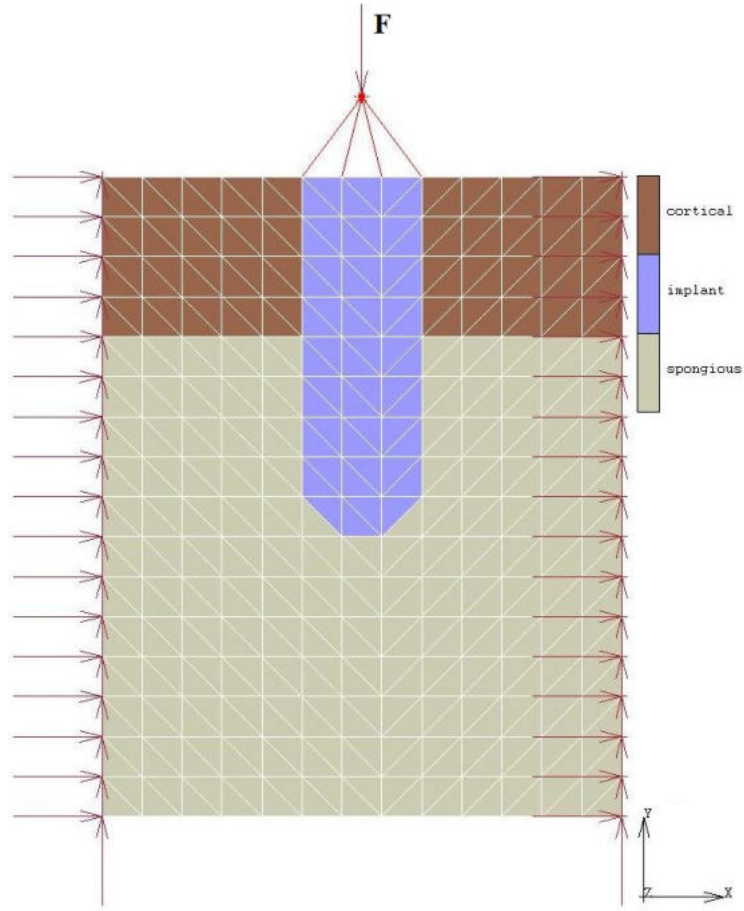
Figure 2.6: Boundary conditions of the basic 2D model.

MPa, 200 MPa, 300 MPa, 400 MPa, 500 MPa, 600 MPa, 700 MPa, 800 MPa, 900 MPa, and 1000 MPa. The scaling factor was 0.05.

2.3.1.2 Influence of the Element Size

The model for sensitivity analysis was developed with different element edge lengths (EEL), namely: 0.5, 0.25, 0.2, 0.167, 0.125, 0.1 mm. The model was used as shown in the figure 2.6. The total force was used in the simulations of 100, 200, 300, 500, and 1000 N. The remodeling parameters were used from [146, 240] as below:

From [146]: k= 0.0004 Jg^{-1}, B= 1.0 $(gcm^{-3})^2$ $MPa^{-1}(timeunit)^{-1}$, D= 60.00 $(gcm^{-3})^{-3}$ $MPa^{-2}(timeunit)^{-1}$,
From [240]: k= 0.0004 Jg^{-1}, B= 1.0 $(gcm^{-3})^2$ $MPa^{-1}(timeunit)^{-1}$, D=

19.48 $(gcm^{-3})^{-3} MPa^{-2}(timeunit)^{-1}$.

All these remodeling parameters were used for the stiff callus (SC), i.e., cortical bone. Later on, the other tissue types were added into the simulation, including healing phases.

2.3.1.3 Influence of the Cortical Bone

To get the ideal model of bone for the bone remodeling simulation, the structure of the bone was changed. For this purpose, a new part of the cortical bone was also added in the lower part of the model, see in figure 2.7. The model was fixed from both sides of the cortical bone.
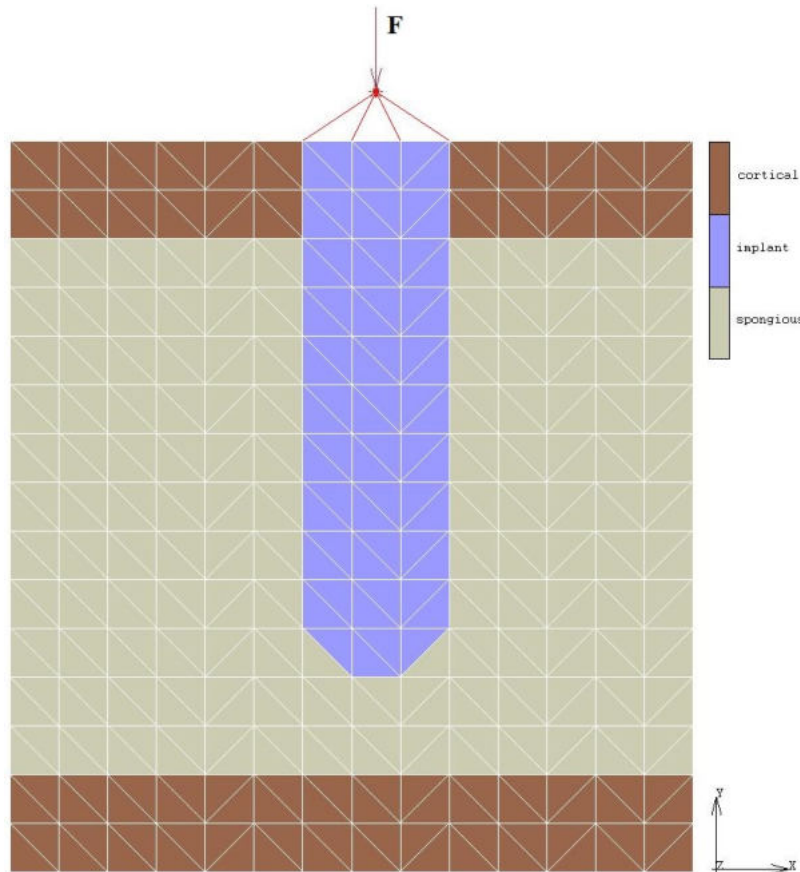
Figure 2.7: Geometry of 2D model with additional cortical part to the bottom of the model.

45

2.3.1.4 Influence of the Implant Geometry

The objective of this section was to see the effect of the pitches in the implant. The bone was considered to be isotropic material with Young's modulus of 20,000 MPa and 300 MPa for cortical and spongious bone, respectively. Poisson's ratio was set to 0.3. For this simulation, similar model was used as shown in figure 2.8, additionally implant was designed with pitches. Density changes were observed after all processes, as shown in the flow chart 2.5. The boundary conditions were similar as before. The model was fixed from both sides of the cortical bone, and the total force was 100 N, applied on the implant. Additionally, muscle pressures were applied as compression and tension to the model from both sides with a force of 5 N.
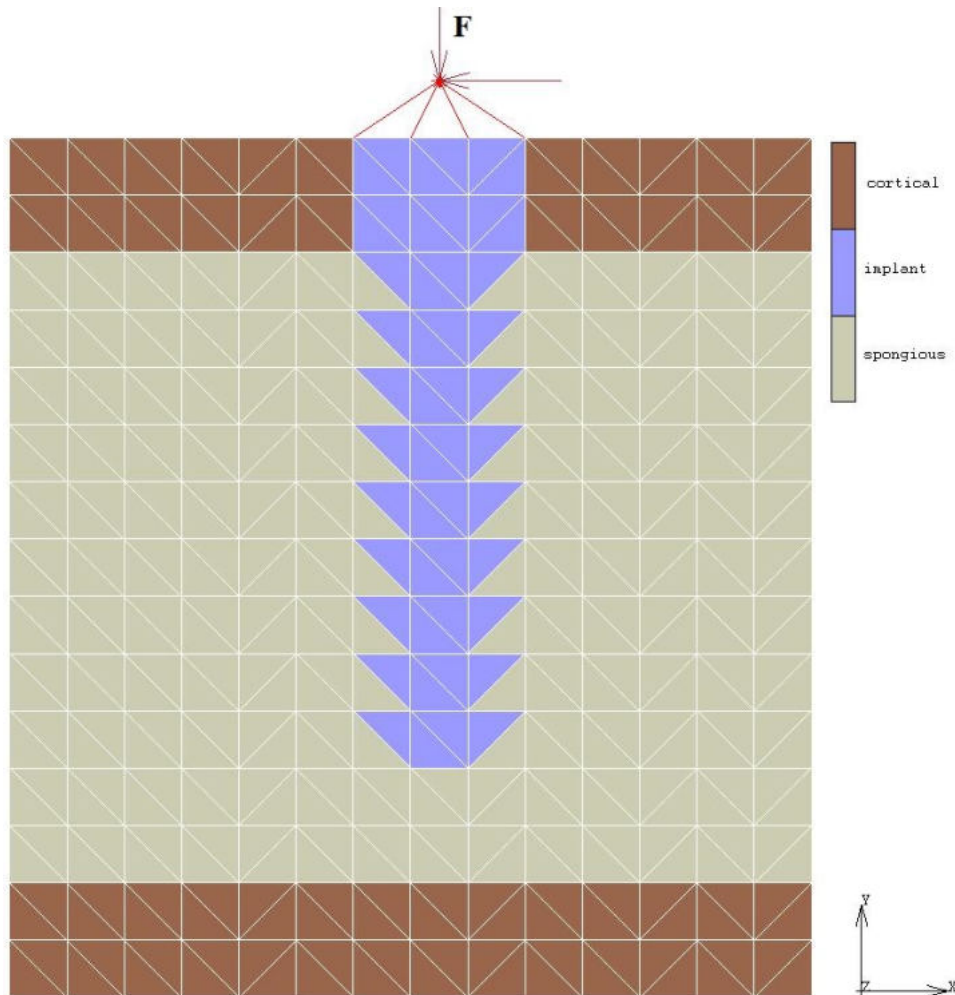
Figure 2.8: Implant with screw pitches in the 2D model.

Later on, the muscle pressure was added in the model to simulate the muscle, which opens the mouth. For this purpose, the opener muscle was attached at the bottom of the model with a surface load, see figure 2.9.
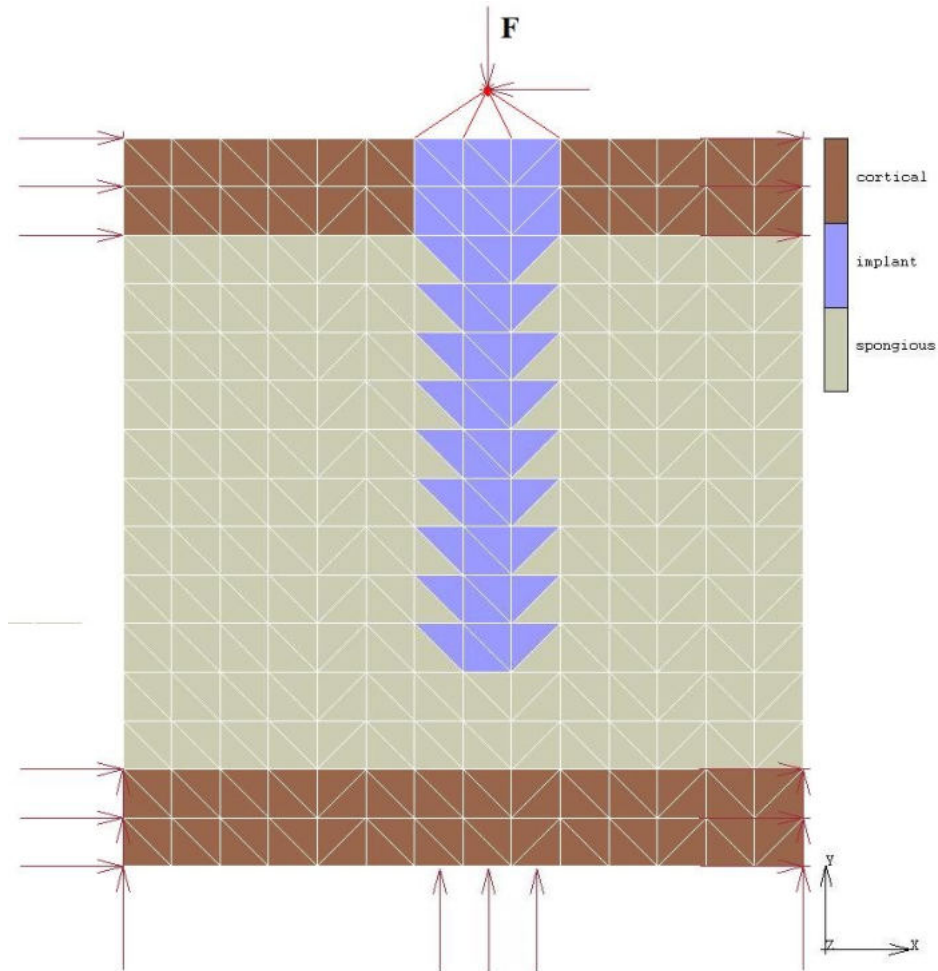
Figure 2.9: Opener muscle and boundary conditions that were used for testing the simulations. The presented model was meshed with EEL of 1.0 mm

2.3.1.5 Influence of the Thickness of Bone

In this section, the model was extended in the Z direction to change the dimension of the model from 2D to 3D. The model is shown in figure 2.10. The total force was applied on the implant at 20° from its long axis with 100 N. The model was developed with different element edge lengths, namely:

47

0.5, 0.2. Different material properties of spongious bone were used during this section to get the ideal material properties: 100 MPa, 250 MPa, 350 MPa, 500 MPa, 800 MPa, 1000 MPa. At the end of this section, muscle force was simulated in the model. Cortical bone was subjected to a tension pressure on the lingual side and a compression pressure on the buccal side at the same time. The muscle pressure were 1.0-15.0 N.
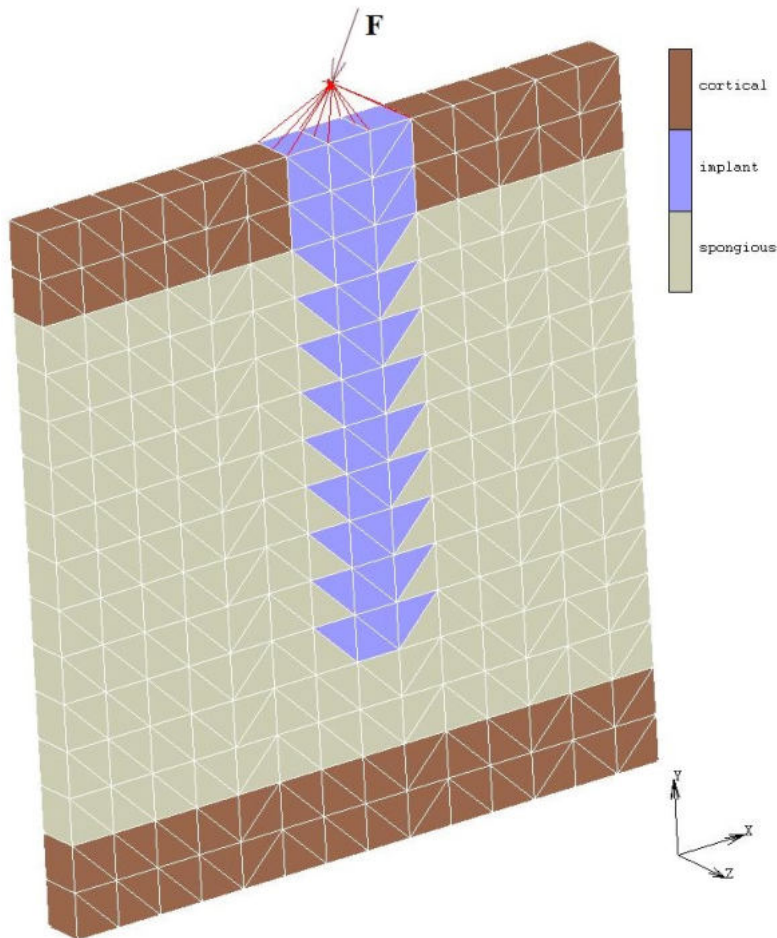
Figure 2.10: The model was extended in the Z direction in order to change the model from 2D to 3D.

2.3.1.6 Influence of the Different Bone Models

Two different models were created in these sections to simulate different implant-bone conditions. Both models were developed with varying shapes of the implant, i.e., diameter and length.

2.3.1.6.1   First Model of Bone

The first model was created with a more realistic bone geometry surrounding the implant. The shape of the model was bigger and longer than previous models. The total force was applied directly from the Y direction to the implant with 100 N. The model was fixed at the bottom nodes from the cortical bone in X, Y, and Z directions. Young's modulus of spongious bone was 1,000 MPa. Also, muscle face loads were applied to the model from the labial and lingual side as compression with 1 N to 15 N (see figure 2.11). The implant dimensions were ⌀=3 mm and L=11 mm.
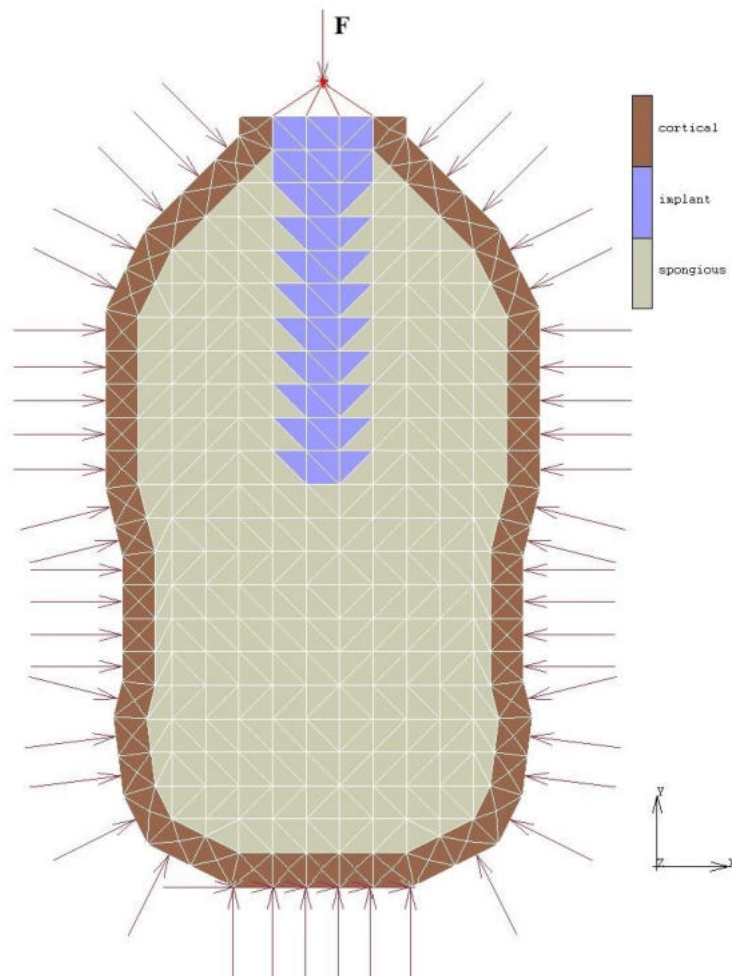
Figure 2.11: View of more realistic geometry in 2D FE model with face loads and boundary conditions.

2.3.1.6.2 Second Model of Bone

The second model was generated with different shape (figure 2.12). The thickness of the cortical bone was higher, and the diameter of the implant was more comparing the model in figure 2.11. The differences between this model and the first model were muscle loads and the total force. Opener muscle loads were simulated in this second model with 2 MPa as pressure applied to several bottom nodes. The total force was applied to the implant at 20 ° from its long axis with 100 N. The fixation was done from the corner of the upper side of the cortical bone with X, Z directions, and also the bottom side of the cortical bone from just two nodes with X, Y, Z directions. The implant geometry was ⌀=4 mm and L=13 mm.
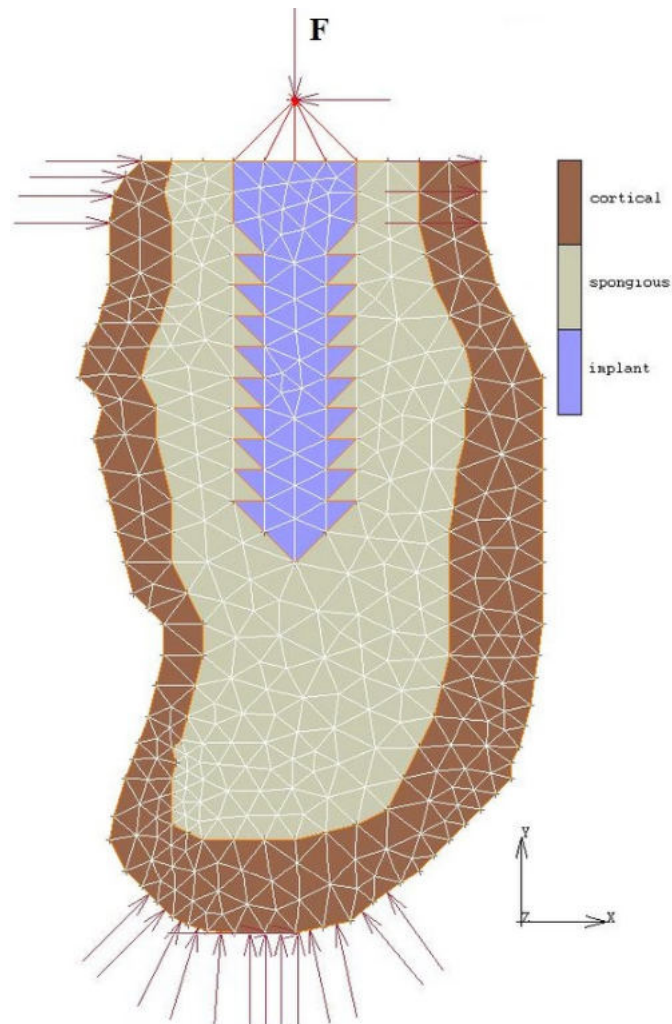
Figure 2.12: View of the second 2D FE model with more realistic geometry.

2.3.1.7 Influence of Osseointegration Phases

A 2D FE model of an implant in a bone segment was created. The bone segment consisted of a 2.0 mm layer of cortical bone surrounding a core of trabecular bone. A separate connective layer was modeled at the bone/implant interface, consisting of up to three different material components (see figure 2.13), to allow the simulation of the healing process. All these layers were done to simulate a full osseointegration.
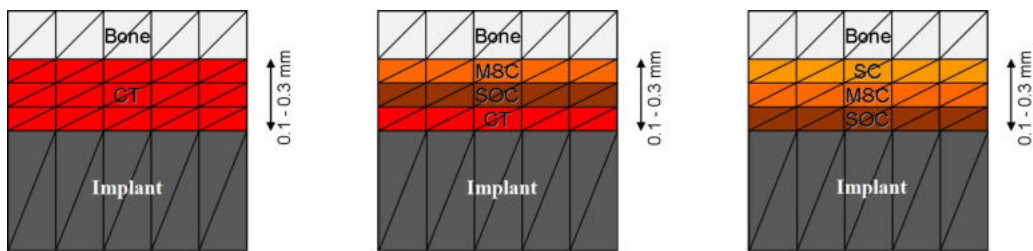
Figure 2.13: Representation of three different histological healing stages in the FE models, phase 1, phase 2, and phase 3, respectively (see Fig.2.4).

Initial FE model used in the simulations: A compressive pressure of 2.0 MPa on the mesial and distal side was used to simulate functional loading, like muscle pressure. In order to get a stable initial bone distribution, bone remodeling was performed for the whole bone and the connective layer using the "classical" remodeling. Elements were assigned to the next tissue group whenever they had reached the maximum density of the respective tissue type. Thereafter, the remodeling resulted in a further density increase in that element. The total thickness of the interface layer was varied from 0.1 to 0.3 mm. Three different healing phases were used. Depending on the healing state, up to three different sublayers with separate initial material properties were used. We created all tissue types around the implant and remodeled them too. The model was developed with different element edge lengths (EEL), namely: 1.0, 0.5, 0.2. The model EEL of 1.0 had 480 nodes, 892 elements, and it was fixed from the corner up and down of the cortical bone.

Material properties and remodeling parameters are shown in table 2.5. The Young's modulus listed here refers to the initial start value of the material at the beginning of the remodeling.

Material	Initial Young's modulus (MPa)	Poisson's ratio	Maximum Density (gcm-3)	Reference Stimulus (Jg-1)
CT	1	0.17	0.07	0.0000004
SOC	1,000	0.3	0.75	0.00002
MSC	6,000	0.3	1.40	0.00008
SC	10,000	0.3	1.74	0.0004

Table 2.5: Material and remodeling parameters used for the different tissue types during the healing stages [240].
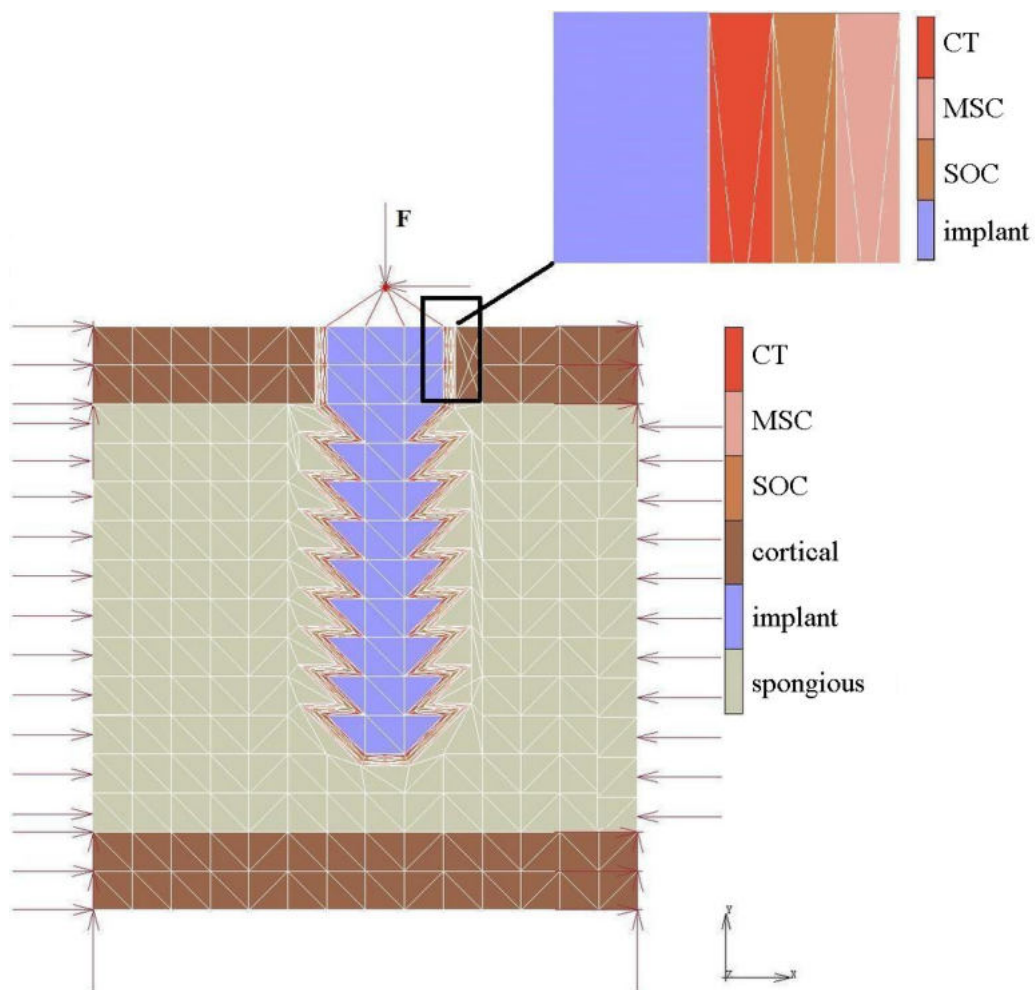
Figure 2.14: View of 2D FE model with different tissue types (see figure 2.13). As an example, Phase 2 is presented in this figure with tissue types CT, MSC and SOC.

52

2.3.1.8 Influence of Healing Phases with Homogeneous Bone

The 2D FE model was created with a bone segment that had a 1.0 mm layer of cortical bone surrounding a core of trabecular bone. The bone was considered to be an isotropic and homogeneous material with Young's modulus of 20 GPa for the cortical bone and Poisson's ratio of 0.3. In the region of the trabecular bone, a grid represented the spongious structure. To simulate the osseointegration state, a separate connective layer was modeled at the bone-implant interface, consisting of up to three different material compositions. Histologically, osseointegration consists of three phases of different tissue states, as in figure 2.13. Cortical, spongious bone, and all tissue types were remodeled during the simulation. The material used to design a dental implant was titanium with Young's modulus of 110 GPa and Poisson's ratio of 0.3.

Two different scenarios were used in this study to simulate bone remodeling theory around dental implants using 2D FE analysis:
1- A 2D FE model of a bone with an implant was developed without osseointegration. For this scenario, remodeling was performed for the whole bone using the "'classical"' remodeling, to get a stable initial bone distribution.
2- A 2D FE model of a bone with the implant and osseointegration phases was developed.

In Figure 2.15, the total thickness of the interface layer was varied from 0.1 to 0.3 mm. Depending on the healing state, up to three different sublayers with separate initial material properties were used. Elements were assigned to the next tissue group whenever they had reached the maximum density of the particular tissue type, and the remodeling resulted in a further density increase in that element.

In this study, different forces were applied on the implant with different angles at 0 ° and 20 ° from its long axis with 100, 200, 300, 500, 1,000 N, see figure 2.15 . The models were tested with different element edge length (EEL) as 0.2 mm and 0.5 mm. The dimensions of the whole model were 14 mm (length) x 15 mm (height). The implant was modeled with L=11 mm, ø= 3 mm. The FE mesh was constructed using triangle elements. Hence, the system comprised about 12,840 elements with 6,570 nodes: i.e., 1,200 elements for the implant, 5,200 for the cortical bone, and 4,100 for the cancellous bone. The mechanical parameters of cancellous bone (initial values before starting remodeling process) were E= 20, 50, 100, 300, 500, 1,000
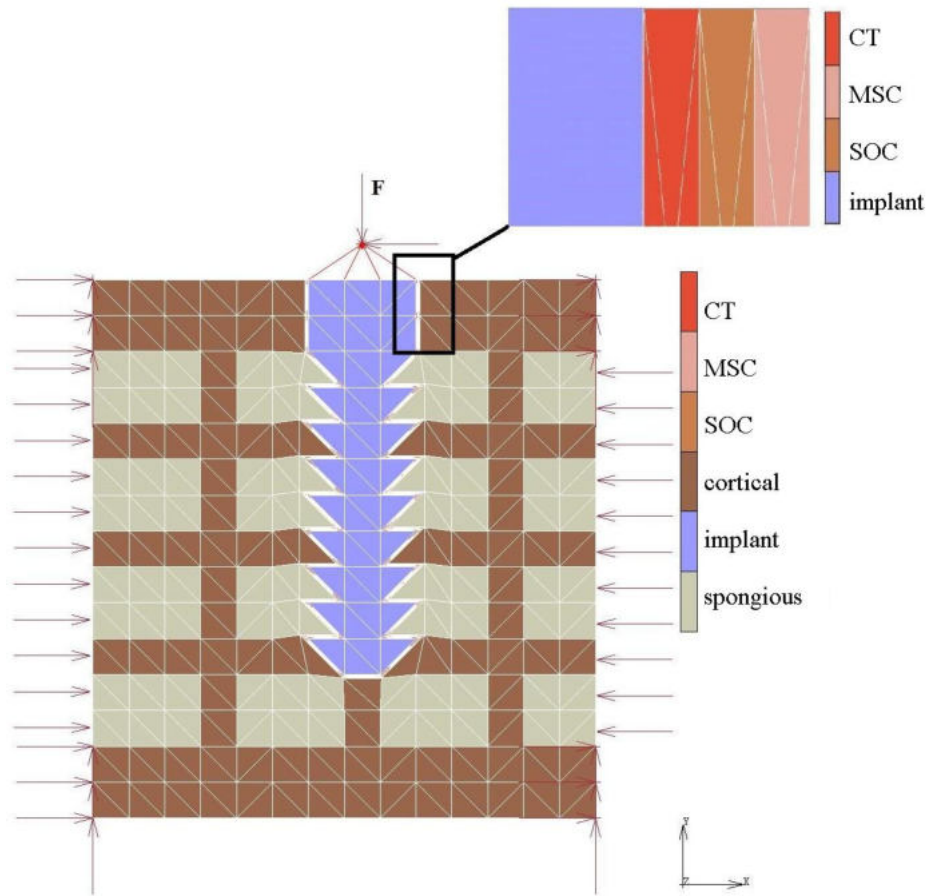
Figure 2.15: View of 2D FE model with homogeneous bone and with different tissue types (see figure 2.13). As an example, Phase 2 is presented in this figure with tissue types; CT, MSC and SOC.

MPa, and Poisson's ratio 0.3.

For simulating muscle loads, different forces were applied to the model to both lingual and labial sides with 1.0, 2.0, 3.0, 4.0, and 5.0 (MPa) as a tension and compression face load, respectively. Four different tissue types with three different phases were modeled between the implant-bone interface to simulate the healing phases. The thickness of the tissue layers also changed with different EELs as 1.0, 2.0, and 3.0 (mm). Tissue layers were initial connective tissue (CT), Soft Callus (SOC), intermediate stiffness callus (MSC), and stiff callus (SC). The material parameters of tissue layers is shown in table 2.5. The three different healing phases were created from these four tissue layers

(see figure 2.13). Material properties and remodeling parameters are shown in table 2.5 as used before.

2.3.1.9 Influence of Time Steps

A further 2D model was generated to simulate the effect of the different scaling factors with respect to the number of times steps. As different parameters, we defined the cortical and spongious bone around the implant, as shown in Fig. 2.16. That means there is no healing phases in this section. EEL was 0.5 mm. The total force was applied to the implant at 20 ° from its long axis with 100 N. Muscle loads were simulated with 2 MPa as compression from both labial and lingual sides of the model. Young's modulus of spongious bone was 300 MPa. Scaling factors were 0.33 and 0.01 with the number of time steps of 300 and 10,000, respectively.
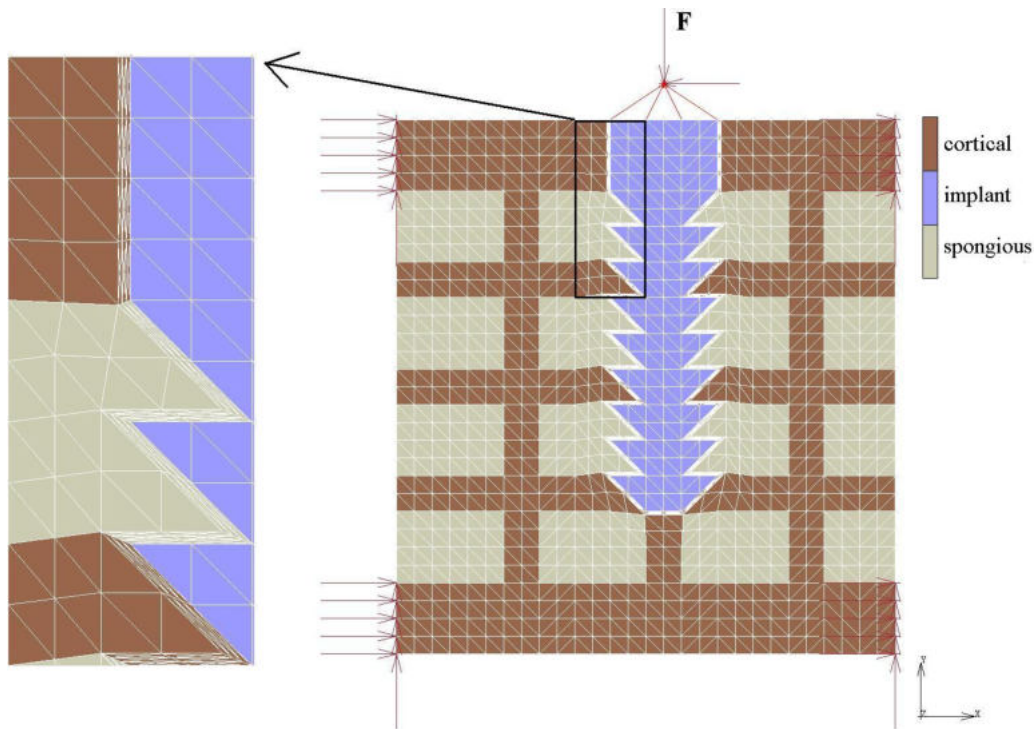
Figure 2.16: View of the material components in the 2D model to simulate the effect of the different time steps.

2.3.2 Sensitivity Tests with 3D Models

3D FE models were used in this section to simulate the mathematical model for bone remodeling with different sensitivity tests in more realistic models.

2.3.2.1 Influence of the Bone Remodeling Theory

A 3D FE model was created by implementing the mathematical expressions of the bone remodeling theory. The remodeling simulations performed in this section were based on the remodeling theory presented by Li et al. [146]. All spongious and cortical bone were remodeled during the simulations. The material components are shown in figure 2.17.
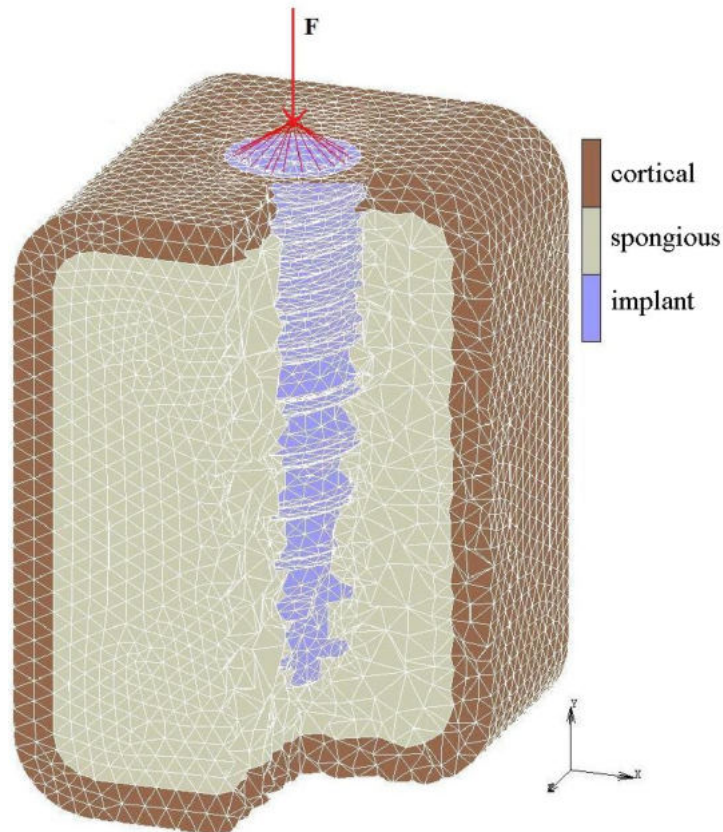
Figure 2.17: View of the material components in the 3D model.

The total force was applied to the implant, and the model was fixed from the nodes of the cortical bone, and some points of the spongious bone, see figure 2.18.
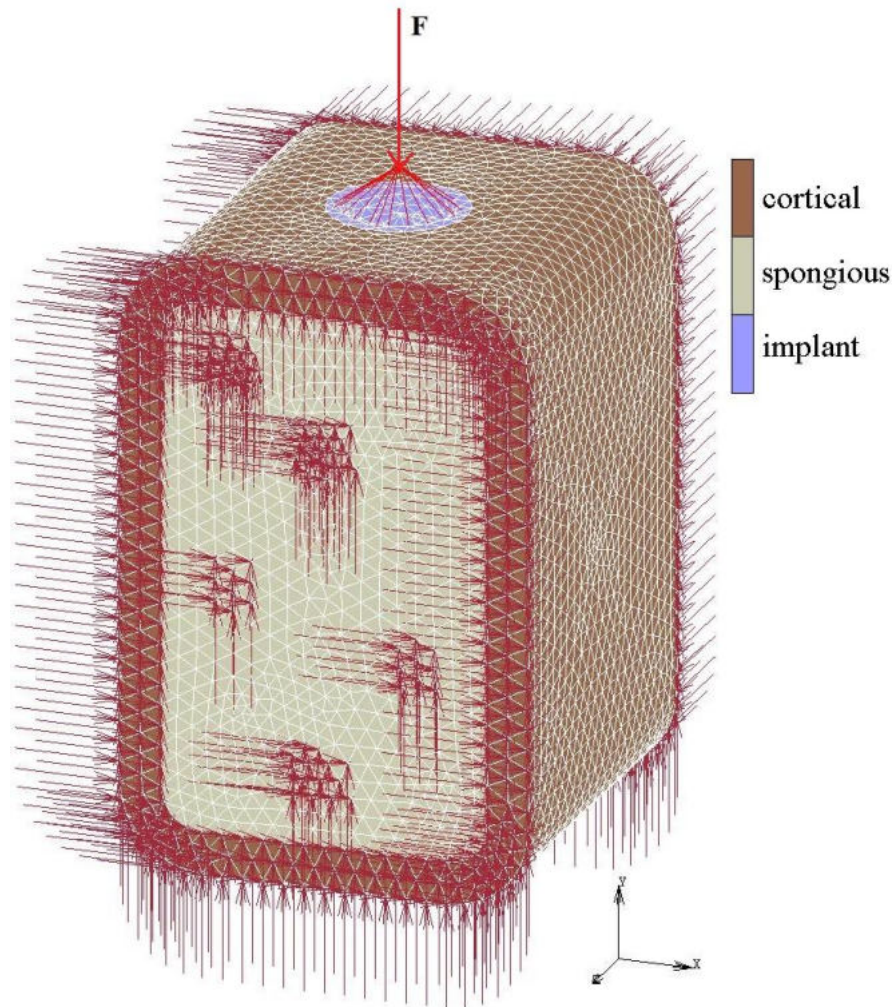
Figure 2.18: Boundary conditions of the 3D model.

The FE mesh was constructed using element type tetrahedral from the library. The model has 107,383 elements with 20,378 nodes: i.e., 17,076 elements for the implant, 36,408 for the cortical bone, and 53,899 for the cancellous bone. An idealized finite element model of the implant (ø 3.7 mm, L 13 mm) in a bone segment was created. The element size of the bone was 0.5 mm, and the mesh of the implant was 0.2 mm. The total model size was (10 mm x 15 mm x 10 mm). The *tioLogic*© ST implant was used in the model. The bone segment consisted of a 1.0 mm layer of cortical bone surrounding a core of cancellous bone. The bone remodeling parameters k, B, and D used from [146, 240] were as in previous sections:

From [146]: k= 0.0004 Jg^{-1}, B= 1.0 $(gcm^{-3})^2$ $MPa^{-1}(timeunit)^{-1}$, D= 60.00 $(gcm^{-3})^{-3}$ $MPa^{-2}(timeunit)^{-1}$,
From [240]: k= 0.0004 Jg^{-1}, B= 1.0 $(gcm^{-3})^2$ $MPa^{-1}(timeunit)^{-1}$, D= 19.48 $(gcm^{-3})^{-3}$ $MPa^{-2}(timeunit)^{-1}$.

The scaling factor was 0.33. The bone was considered to be isotropic material with Young's modulus of 20 GPa and 300-1,000 MPa for cortical and cancellous bone, respectively. Two force magnitudes were applied on the implant at 20 ° from its long axis: 100 N and 300 N.

2.3.2.2 Influence of the Muscle Forces

In this section, the effect of the muscle forces were simulated in the 3D FE model. Like the previous model, the numerical model consisted of 1.0 mm thick cortical bone surrounding a core of spongious bone. The bone was considered as isotropic and homogeneous material. The scaling factor was 0.33. Young's modulus of spongious bone was 1,000 MPa, and total forces were applied on the implant at 20 ° from its long axis of 100-300 N. Additionally, the cortical bone was subjected to a tension pressure on the lingual side and a compression pressure on the buccal side at the same time. Green and blue colors show muscle loads from labial and lingual sides, respectively (see figure 2.19). The 'dead zone' was used as 20 % of k, as suggested by Li et al. [146] and Hasan [240]. Bone remodeling parameters were used as below:

From [240]: k= 0.0004 Jg^{-1}, B= 1.0 $(gcm^{-3})^2$ $MPa^{-1}(timeunit)^{-1}$, D= 19.48 $(gcm^{-3})^{-3}$ $MPa^{-2}(timeunit)^{-1}$.

Another view to show the muscle loads from the opposite side of the model is shown in figure 2.20. As shown in the model, compression loads were applied to the model from the labial side, and tension loads were applied to the model from the lingual side.

Muscle pressures were between 0 and 5.0 MPa, as shown in table 2.6. The maximum time steps and scaling factors were 100 and 0.33, respectively.
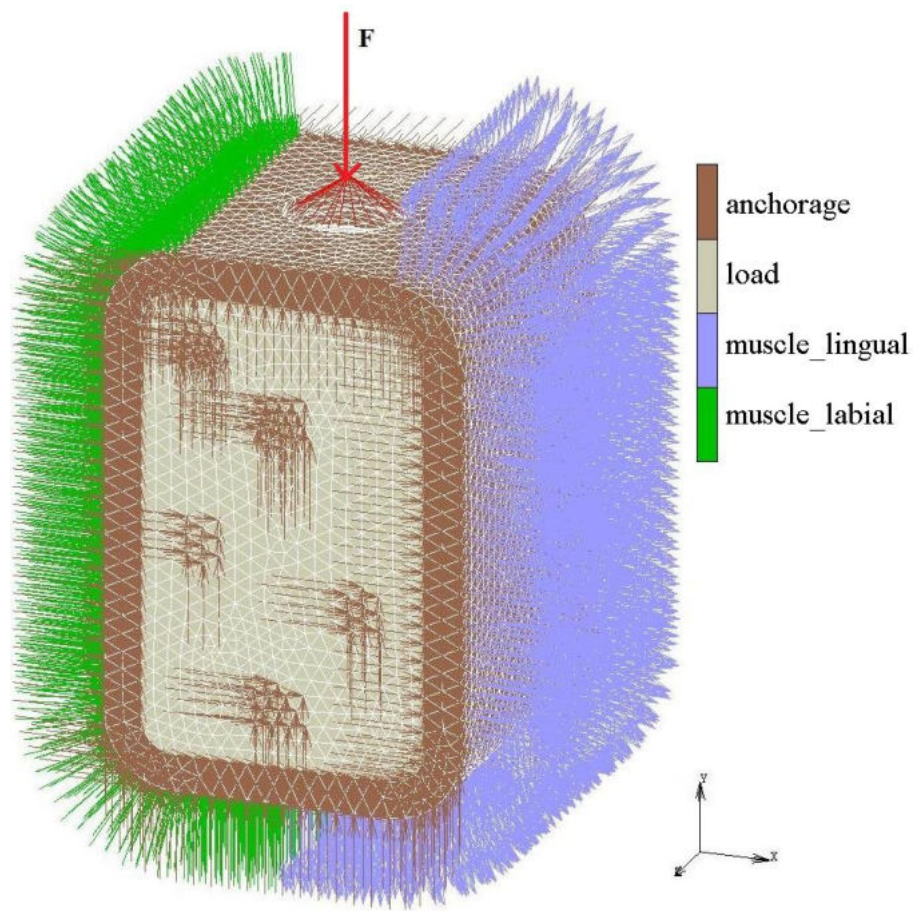
Figure 2.19: Muscle loads and boundary conditions in the 3D model.
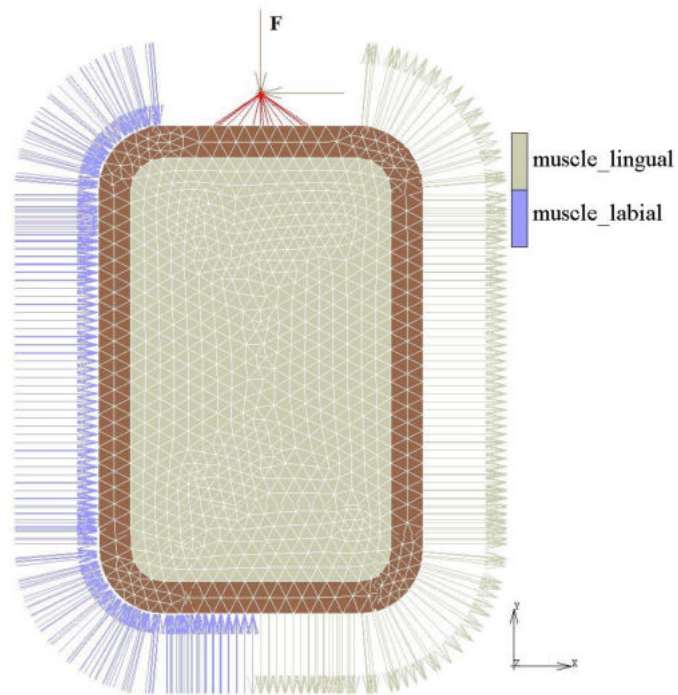
Figure 2.20: Another view of the muscle pressures and total force in the 3D model. The position of the muscle pressures are presented in this figure as compression and tension of labial and lingual sides, respectively.

	Compression (Labial Side)	Tension (Lingual Side)
Face Load (MPa)	0.5	-0.5
	0.7	-0.7
	1.0	-1.0
	1.5	-1.5
	2.0	-2.0
	2.5	-2.5
	3.0	-3.0
	4.0	-4.0
	5.0	-5.0
	3.0	0
	0	-3.0
	4.0	0
	0	-4.0
	5.0	0
	0	-5.0

Table 2.6: Types of face loads. Different face loads were applied to the models as compression and tension.

2.3.2.3   Influence of the Boundary Conditions

Previous models were fixed from the front and the back of the model from cortical and some points of the spongious bone. In this section, additionally, different fixations were applied to the model, e.g., at the lower part of the model from the cortical bone. The model is shown in figure 2.21. Hence, muscle loads were changed. Both muscle loads were applied to the model as compression, see figure 2.21. Muscle loads were 2 MPa for both sides. Two steps were done in this section:

1- Only spongious bone was remodeled during the simulations.
2- All bone components (cortical and spongious) were remodeled.
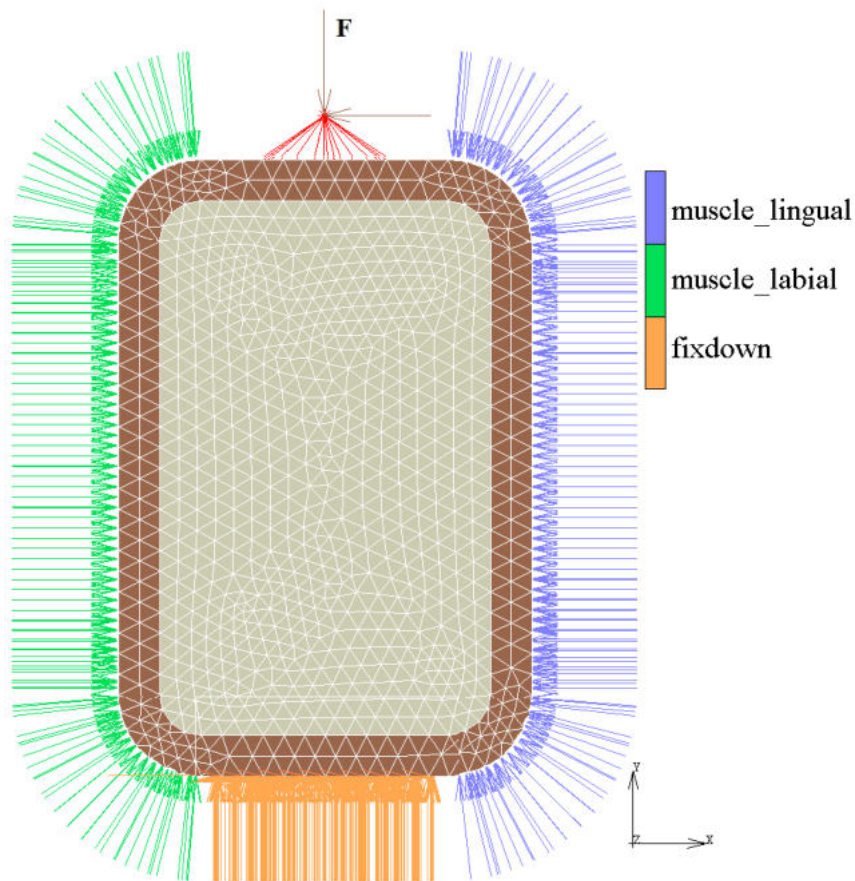
Figure 2.21: View of the boundary conditions in the 3D model.

Subsequently, the fixation was changed in the model. The upper and lower parts of the cortical bone were fixed from the outer lines, as shown in Fig. 2.22. Muscle pressures were 2.0 and 5.0 MPa as compression and tension.
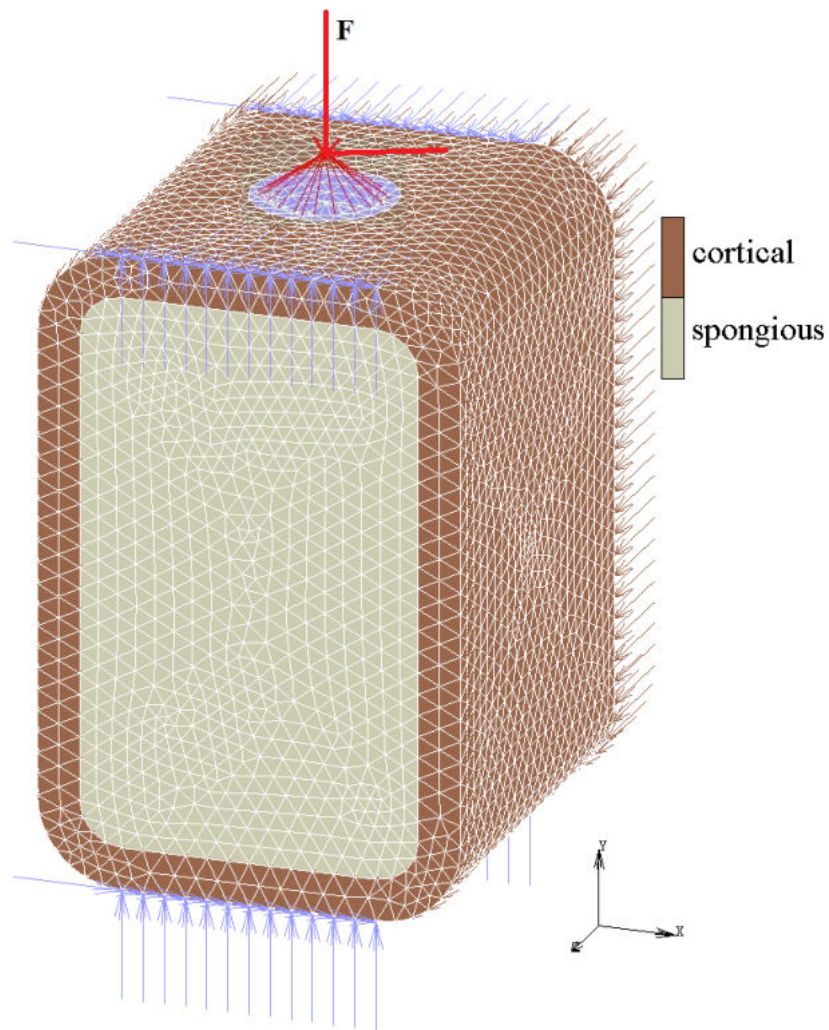
Figure 2.22: Different fixation conditions in the model.

2.3.2.4 Influence of the Element Size

Until now, the EEL was used as 1.0 mm. Maximum EEL was used in the simulations. This section aimed to see the effect of the EEL of 0.5 mm. The

model was meshed with EEL of 0.5 mm (see figure 2.23). The same boundary conditions were applied to the model except for muscle loads. Compression and tension muscle loads were applied to the model from both sides with 2 MPa. The model had 859,064 elements and 161,096 nodes. The scaling factor and maximum iterations were 0.33 and 100, respectively.
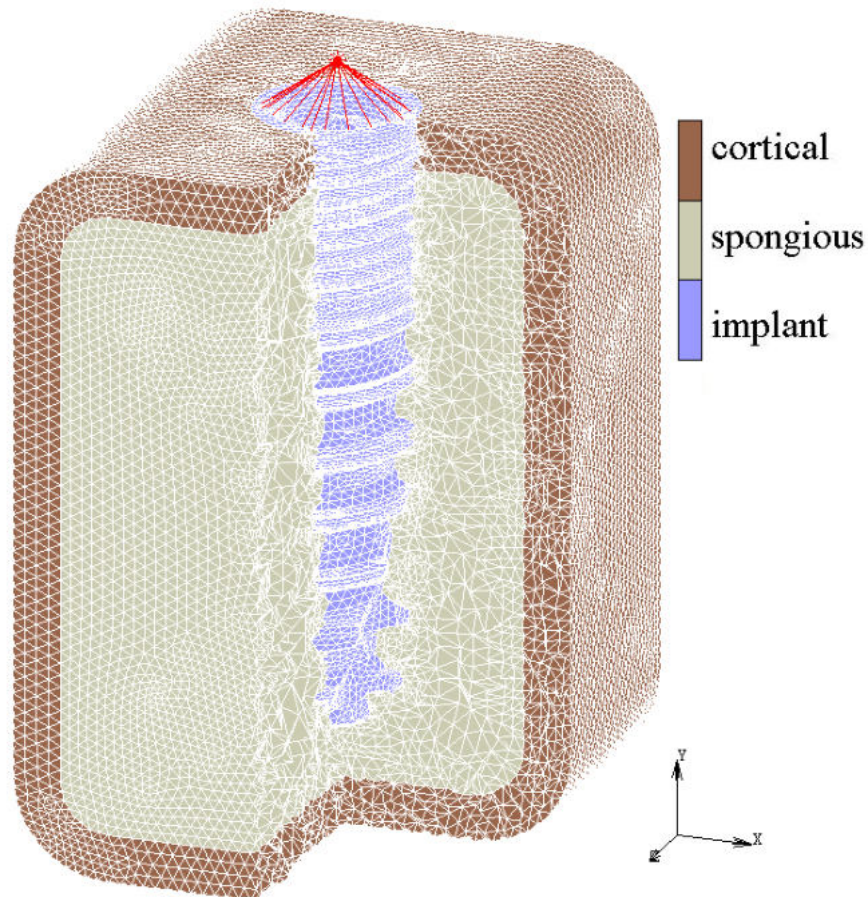
Figure 2.23: The view of the 3D model with reduced element size of 0.5 mm.

2.3.2.5 Influence of the Bending Force

Functional mastication loads are applied via the teeth. This is the reason why the mandibular bone is a unique structure. The functional loads create bending with maximal stresses in the mandibular bone. In this section, we wanted to simulate the effect of the bending of the mandible. The model had 292,804 elements with 52,211 nodes.
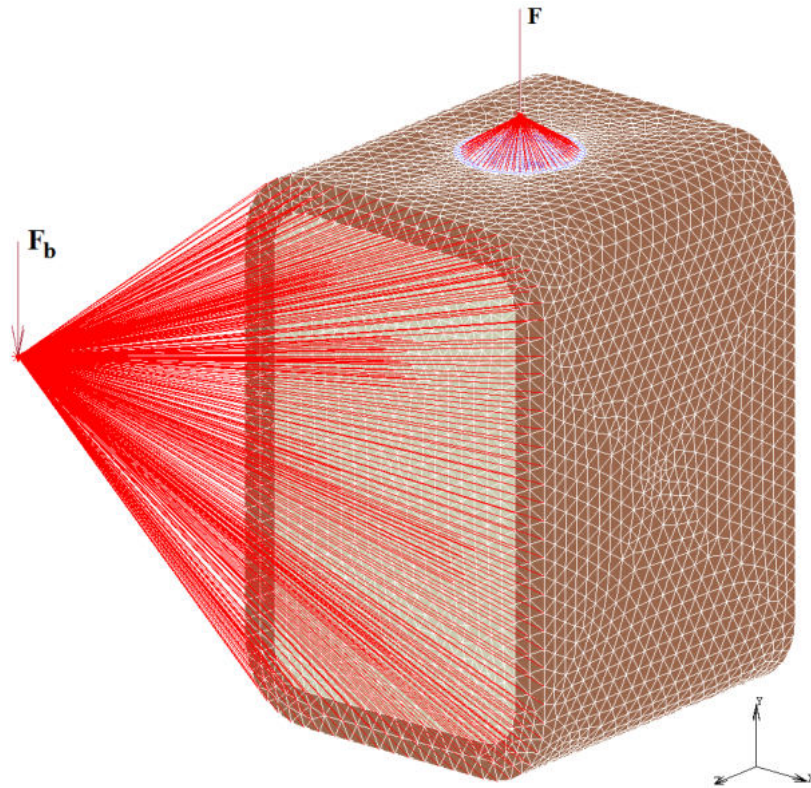
Figure 2.24: Total force (F) and bending force (F_b) were applied to the 3D model. F_b had connection with the nodes of the cortical and spongious bone.

Figure 2.24 shows the bending force in the model. A point was defined 20 cm far from the model, and this point had a connection with the nodes of that surface of the model with 10, 50, and 100 N from Y and Z directions. Different muscle loads were applied to the model as previous simulations from the labial as compression and lingual side as tension during the bending tests between 1.5-2.5 MPa. The fixation was applied at the back of the model.

2.3.2.6   Influence of the Fixation

The fixation is a significant effect for all simulations regarding its remarkable influence on bone deformation. We aimed to simulate a new fixation in the model to get the ideal conditions for the simulations. For this aim, the model was fixed from two points, which were created 20 cm far from the model. These two points were connected to the nodes on the surface of the model from both cortical and spongious bone; see figure 2.25.
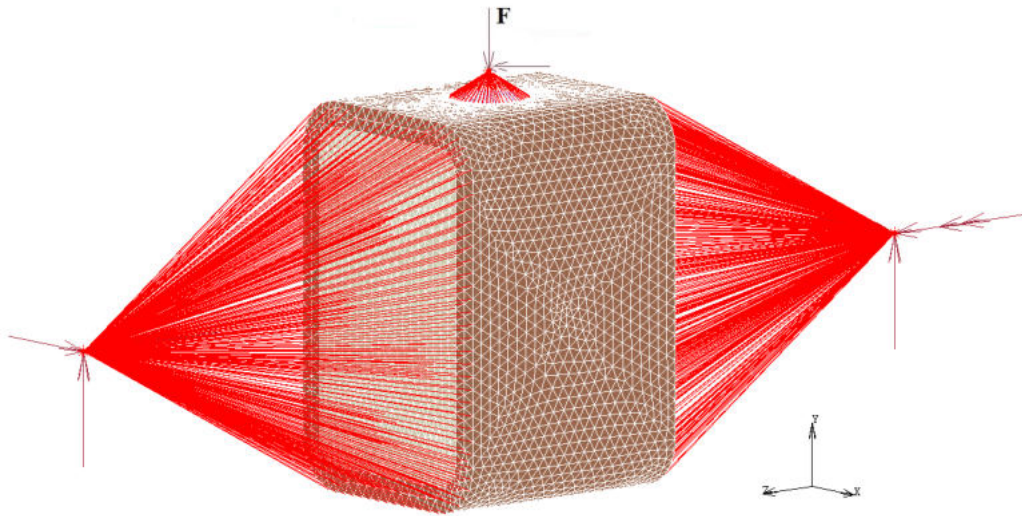
Figure 2.25: The view of the 3D model with different fixations from both sides.

The fixation was done from X, Y, and Z directions and rotation around the Z axis. The model was fixed and rotation was inhibited except for the front part, as seen in the figure. Additionally, muscle pressure was applied with 1.0, 1.5, 2.0, and 2.5 MPa to the model as previous simulations from the labial as compression and lingual side as tension. The total force was applied to the implant at 20 ° from its long axis with 100 N.

2.3.2.7 Influence of the Implant Geometry

Until now, the posterior tooth area was generated for all simulations. For comparing different parts of bone, the anterior tooth area was used in this section. Different boundary conditions and material properties were previously changed and applied to the models during the simulations. In this section, a mini dental implant was used to show the effect of the implant design on the bone remodeling process. Titanium mini-implant was used with Young's modulus of 110 GPa, see the mini implant model with ø=2.2 mm and L=15 mm in figure 2.2.

The bone was considered to be an isotropic and homogeneous material with Young's modulus of 20 GPa and 1,000 MPa for the cortical bone and spongious bone, respectively (see figure 2.26). Poisson's ratio was 0.3. The thickness of the cortical bone was 1.2 mm, and 2.66 mm for spongious bone. The length of the spongious bone was 14.6 mm. The thickness of the total
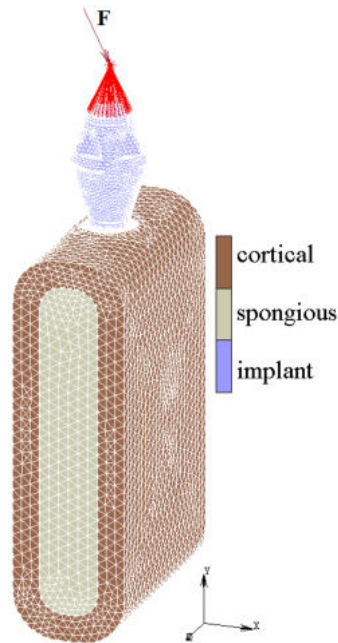
Figure 2.26: View of material properties of the 3D model with Dentaurum CITO mini ®implant. Dimensions of mini implant were ø=2.2 mm and L=15 mm.

model was 5 mm, and the length of the total model was 17 mm, except for the implant. Two steps were done in this section:

1. Step: Boundary conditions: The total force was applied to the implant from Y direction with 10, 50, 100, 150, 200, 300, and 500 N. The model was just fixed from both front and back sides from all cortical and spongious bone, see figure 2.27.

2. Step: The same model was used. Additionally, muscle loads were applied to the model with face loads of 1.0, 2.0, and 3.0 MPa as previous simulations from the labial similar to compression and lingual side as tension loads, see figure 2.28.

The scaling factor and maximum iterations were 0.33 and 100, respectively. The element size was 0.4 mm. The model had 886,112 elements with 156,327 nodes: i.e., 303,949 elements for the implant, 59,090 for the cortical bone, and 523,073 for the spongious bone.
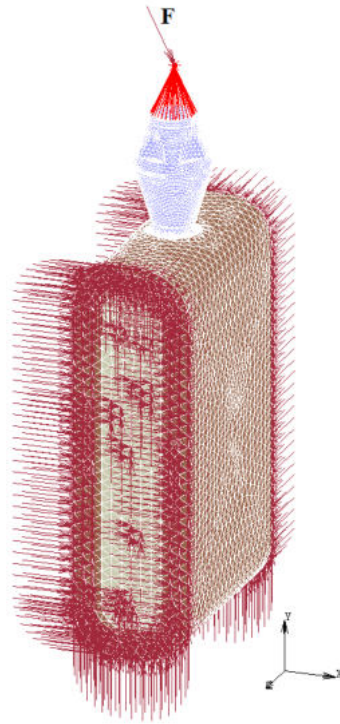
Figure 2.27: The boundary conditions of the model with mini implant.
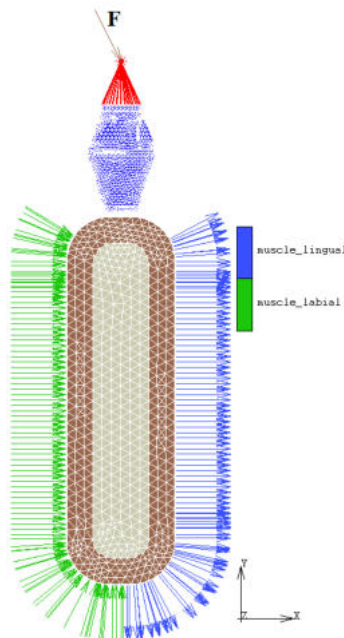
Figure 2.28: View of applied muscle pressure to the 3D model with mini implant, as compression and tension.

3 RESULTS

Bone remodeling simulations with both 2D (with and without osseointegration) and 3D (no osseointegration) FE models were performed, as explained in the previous section. The results of all sensitivity tests for all models are presented in this section. Different mechanical stimuli were applied to the models. The density change will also be presented in this section. The new density was calculated during the simulations when the mechanical stimulus was applied to the old density. Scaling factor is a variable to control the amount of density change per iteration while different maximum iterations were used for the simulations, like 100, 300, 500, 1,000, and 10,000.

3.1 Sensitivity Tests with 2D Models

Changes in bone density with the different mechanical parameters are presented after the different number of time steps depending on the simulations. Results for total deformation, stress, total strain, total strain-energy density, and total displacement between bone-implant interface were evaluated.

3.1.1 Influence of the Spongious Bone Stiffness

It is to be expected that the initial Young's modulus used to describe spongious bone before remodeling has at least a limited effect on the remodeling outcome. If the spongious bone elements start with a too low Young's modulus, this will probably result in a fast bone resorption due to overloading these elements, while with a too high Young's modulus we might see a quick resorption due to disuse. Thus we need to verify that we start with Young's modulus that is within a stable region, that is neither too low nor too high.

To verify this, a series of simulations was performed with different initial values for the Young's modulus of the spongious bone. Application of the bone remodeling algorithm in the 2D model is illustrated in figure 3.1. Three results of density changes are demonstrated with an initial Young's modulus of bone of 300, 700, and 1,000 MPa. These limits represent typical values of bone elasticity used in literature when a homogeneous spongious bone is simulated (e.g. [243]). There was resorption in the bone when Young's modulus was too small. Furthermore, the bone got too stiff when Young's modulus was higher than 1,000 MPa. Density distribution within the range of 0.0 to 1.74 g/cm^3 was used to demonstrate the results. In the yellow part,

density was higher than 1.74 g/cm^3. The lower part of the spongious bone had maximum density, with Young's modulus of 700 MPa comparing with 1,000 MPa. Similar results were obtained when the initial Young's modulus was in the range of 300 and 1000 MPa. An initial Young's modulus of 200 MPa and below resulted in a fast overload resorption. Based on these results, in the further steps of the sensitivity analysis two different Young's moduli of 300 and 1000 MPa were tested to represent this stable range.
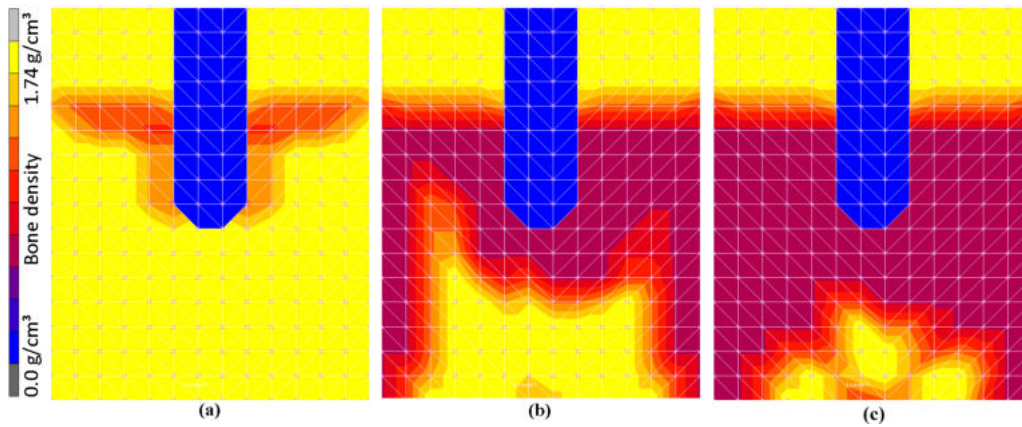
Figure 3.1: Density distribution of spongious bone with Young's modulus of (a) 300 MPa, (b) 700 MPa, and (c) 1,000 MPa.

3.1.2   Influence of the Element Size

Figure 3.2 shows the density distribution with a total force of 500 N. Bone resorption occured when the total force was below 500 N. Furthermore, overloading resorption was obtained when total force was above 500 N. The results with EEL 0.5 mm and 0.2 mm were used in the figure 3.2 to show the effect of the EEL in the same model under the same boundary conditions. The boundary conditions were the same as in figure 3.1 except of the total force and EEL. Maximum number of time steps was 100. As seen in the figure 3.2, 0.5 mm EEL showed very dense elements within the spongious bone, while 0.2 mm EEL showed interesting density variations resembling trabecular bone.
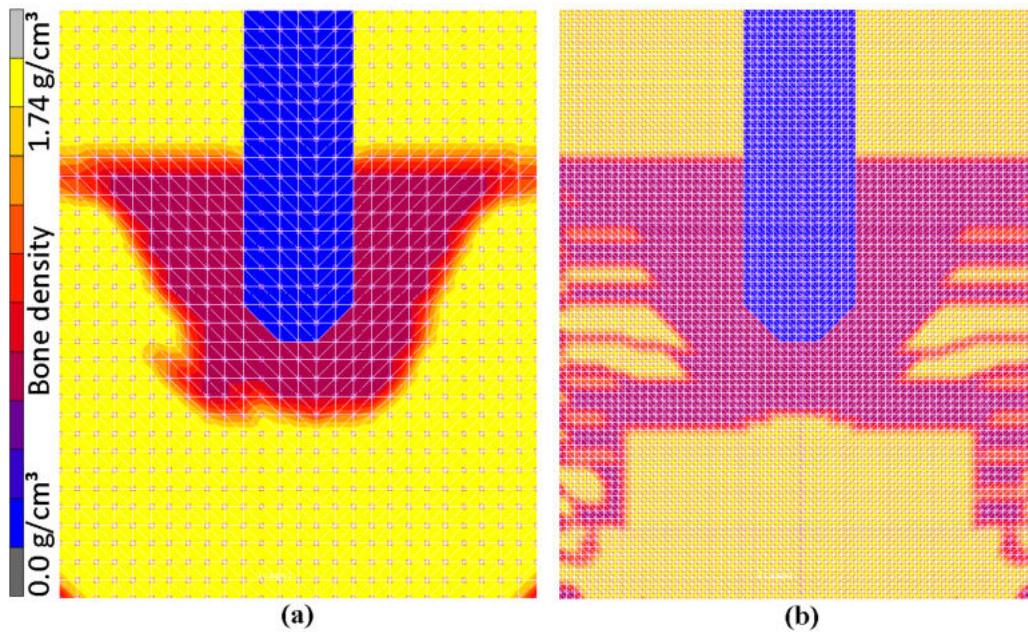
Figure 3.2: Density distribution with total force of 500 N, (a) with element edge lengths EEL of 0.5 mm, and (b) EEL of 0.2 mm.

3.1.3 Influence of the Cortical Bone

The effect of the extra cortical bone, which was added to the bottom of the model was simulated. Figure 3.3 shows the density changes with different parameters: (a) EEL with 0.5 mm and (b) EEL with 0.2 mm, respectively. Density distribution within the range of 0.0 to 1.74 g/cm^3 was used to demonstrate the results. The maximum number of time steps was 100. The cortical and spongious bone reached maximum density under both (a) element edge lengths of 0.5 mm, and (b) EEL of 0.2 mm. Bone resorption was obtained below the tip of the implant in both models.
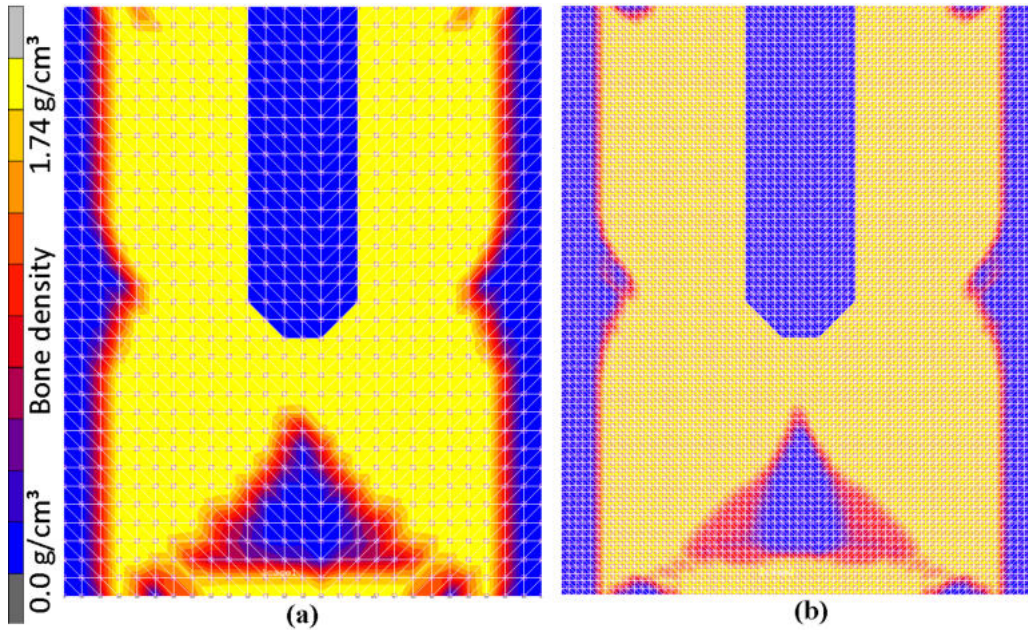
Figure 3.3: View of density distribution with total force of 100 N: (a) EEL of 0.5 mm, (b) EEL of 0.2 mm.

3.1.4   Influence of the Implant Geometry

Figure 3.4 shows the density distribution after the first and the maximum iterations which was done with 100 in the bone remodeling simulations. The maximum number of time steps was 100. The muscle pressure was 5 MPa in this simulation. Blue parts are resorption in the sides of the bone due to overloading. The red parts are showing bone formation, which generally takes place in spongious bone and around the implant.

Furthermore, figure 3.5 shows the density changes with the effect of the different muscle loads. Opener muscle loads were of 5 N applied to the model. Additionally, two different muscle loads were applied to the model from both sides as (a) compression, and (b) tension of 5 MPa. Total force on the implant was 100 N during the simulation. New bone formation was observed around the implant and also on some part of the spongious bone in both (a) and (b). The cortical bone was reduced in density under tension, which is shown in (b).

71
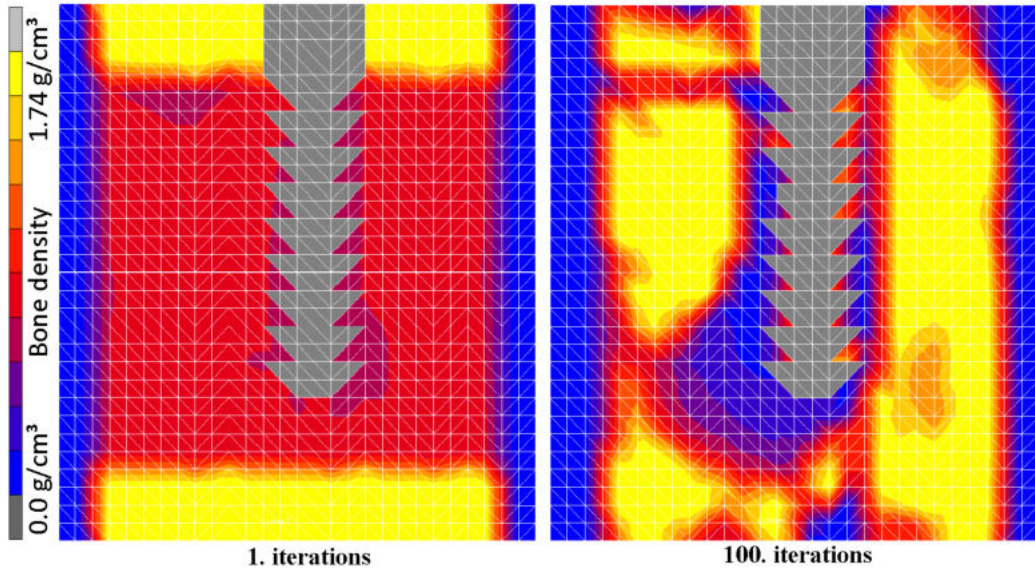
Figure 3.4: View of density changes under total force on the implant of 200 N, muscle pressure of 5 MPa and EEL of 0.5 mm.
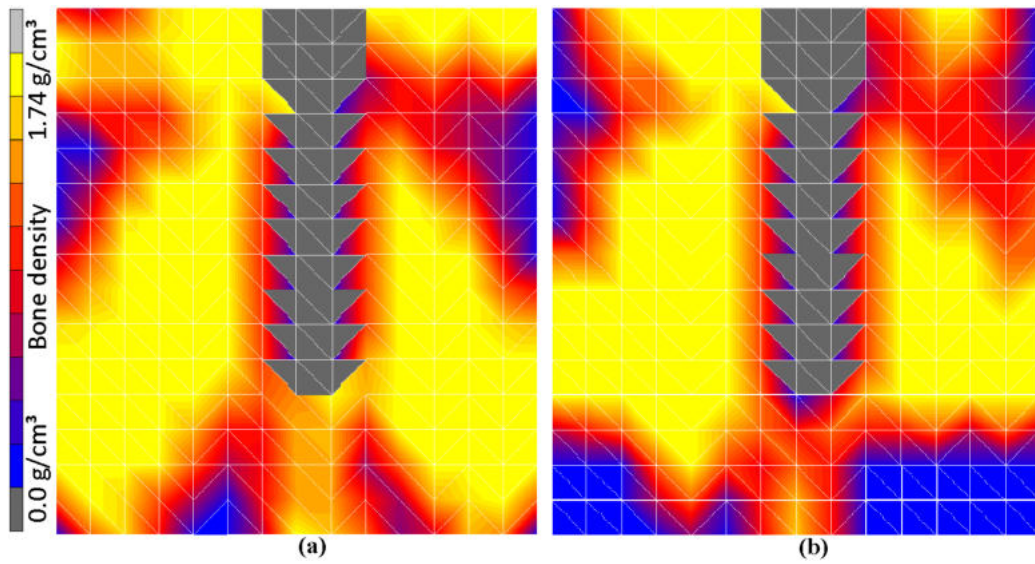
Figure 3.5: The effect of the opener muscle loads of 5 N with different muscle pressures as (a) compression and (b) tension to both sides of the model of 5 MPa. Total force on the implant was 100 N.

3.1.5 Influence of the Thickness of Bone

The extended models were studied in this section. Figure 3.6 shows the results of two different simulations. Varying boundary conditions were applied to those models with different total force, EEL, muscle loads, and also different Young's modulus of spongious bone. Figure 3.6, (a) shows the effect of Young's modulus of spongious of 100 MPa, (b) with Young's modulus of spongious of 350 MPa. New bone formation was observed in part of the spongious bone and around the implant in (a) and on the other hand, spongious bone reached the maximum value in (b). Despite, overload resorption occured in both models on the cortical bone.
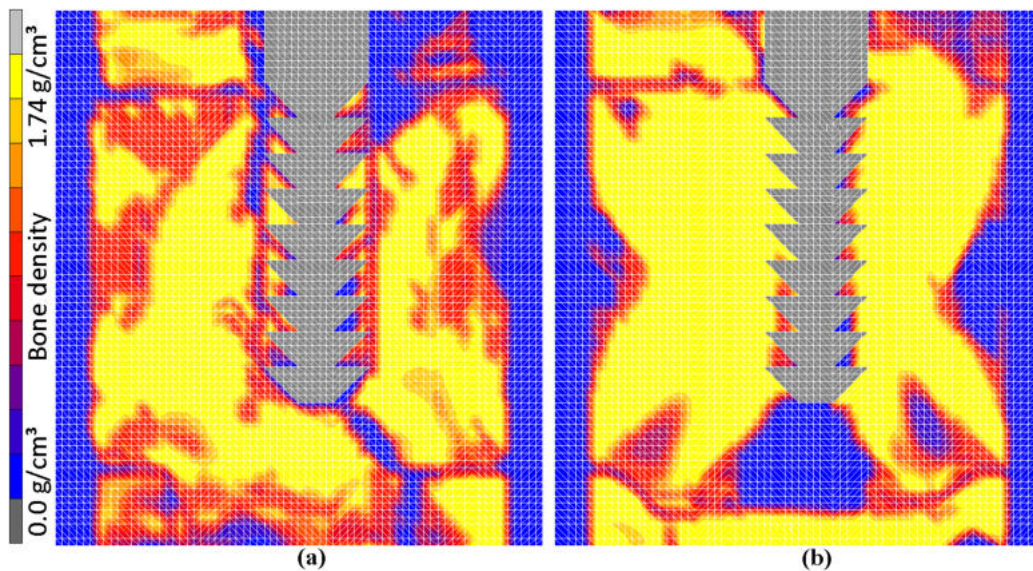
Figure 3.6: The effect of Young's modulus of spongious bone (a) with 100 MPa, (b) with 350 MPa.

3.1.6 Influence of the Different Bone Models

3.1.6.1 First Model of Bone

Figure 3.7 shows the effect of the different muscle loads on the model with realistic geometry, which is longer and bigger than other models. Bone formation was obtained around the implant and the sides of both models (a) and (b). The density reaches a steady-state in the bottom part of both models.
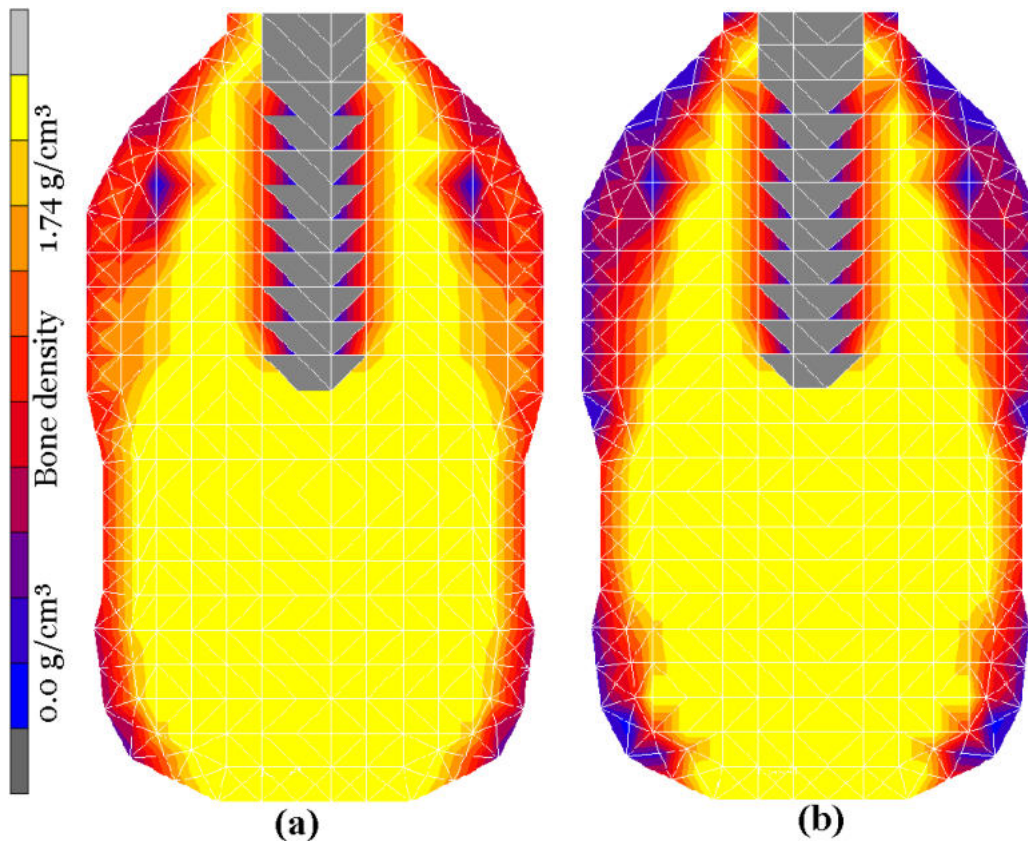
Figure 3.7: The effect of the muscle pressures: (a) with 5 MPa, (b) with 15 MPa.

3.1.6.2   Second Model of Bone

In Fig. 3.8, first and maximum iterations are presented to show the density changes. EEL was 0.2 mm, opener muscle faces were applied with 2 MPa as compression. Young's modulus of spongious bone was 1,000 MPa. Some new bone formation occurred around the implant. Lower part of spongious bone reached the maximum density. Furthermore, overloading resorption was obtained in the right part of cortical bone. The aim of these last two sections was to simulate the effect of the different bone models which were used in the literature [244]. We wanted to model the real bone shape with implant. Nevertheless, we did not get significant results with a spongious structure in the models as seen in the Fig. 3.7 and 3.8. That's why the further sections were done with basic 2D bone models as previous sections.

74
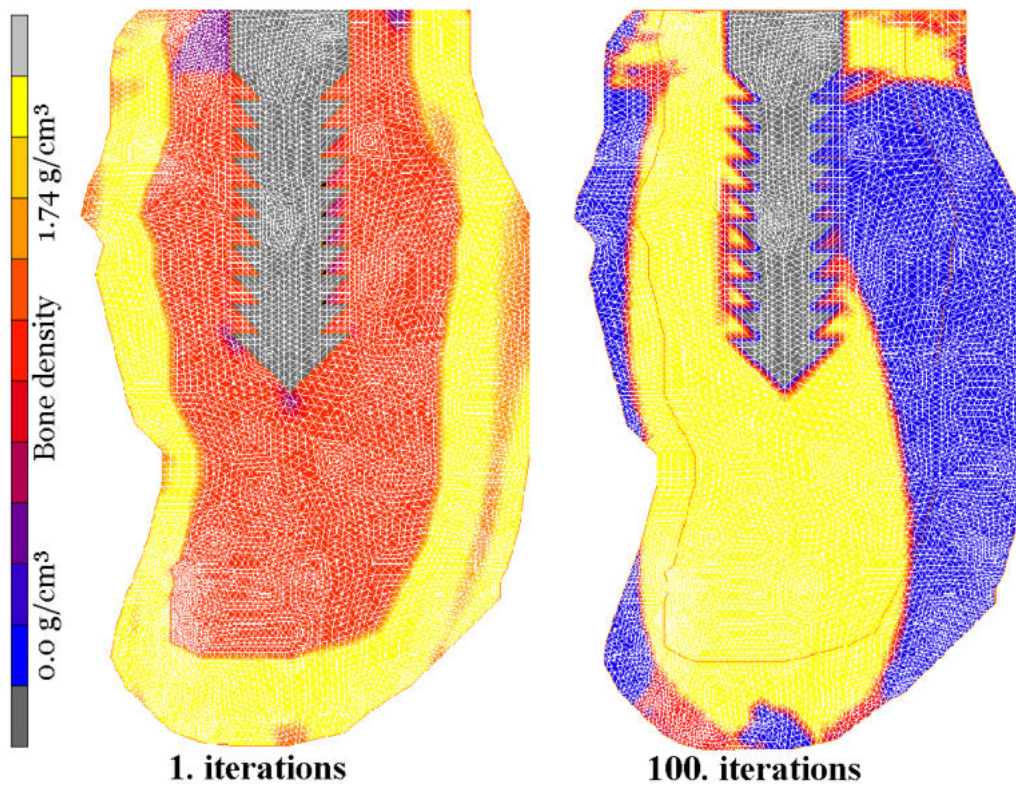
Figure 3.8: Variation of the initial bone stiffness for spongious bone from 1. iteration and maximum (100th) iterations. Number of time steps presents as iterations.

3.1.7 Influence of the Osseointegration Phases

Total force was applied at the implant of 100 N and Young's modulus of spongious bone of 1 GPa. Muscle force was applied as compression from both sides of the model with 2 MPa. CT, SOC, and MSC were used in these simulations for simulating osseointegration. All tissue types were remodeled during the simulations as cortical and spongious bone. Figure 3.9, 3.10, and 3.11 show totally nine different results of bone remodeling simulations with EEL 0.2 with phase 1, phase 2, and phase 3, respectively. Each figure shows the influence of the thickness of the tissue types with 0.1 mm, 0.2 mm, and 0.3 mm.

New bone formation occurred around the implant with 0.1 mm in Fig. 3.9. On the other hand, overloading resorption was obtained around the im-

plant with 0.2 mm and 0.3 mm in Fig. 3.9. Furthermore, the results with 0.2 mm were better than 0.1 and 0.3 mm on the left side of the implant neck. Bone resorption was obtained below the tip of the implant with 0.2 and 0.3 mm comparing with 0.1 mm. These results show that osseointegration was achieved with the thickness of the tissue types with 0.1 mm better than 0.2 mm and 0.3 mm.

Conversely, bone formation was obtained at the neck of the implant with 0.2 and 0.3 mm in Fig. 3.10. On the other side, bone resorption occurred at the neck of the implant with 0.1 mm. Bone resorption was obtained in cortical bone near the left side of the implant neck and on the right side of the implant body in cortical and spongious bone with 0.3 mm. Besides, nice bone formation results was obtained around the implant body and below the implant tip with 0.1 mm.

Osseointegration was achieved with the thickest layers, i.e., 0.2 mm and 0.3 mm in phase 3 in Fig. 3.11. Bone resorption occurred on the left side of the implant neck with 0.1 mm. Bone reached maximum density in all thicknesses in phase 3. The optimal bone healing was observed with phase 3 comparing phase 1 and phase 2. Phase 1 and phase 2 did not achieve good results like phase 3. Because, phase 1 and phase 2 had softy tissue types and phase 3 had stiff materials.
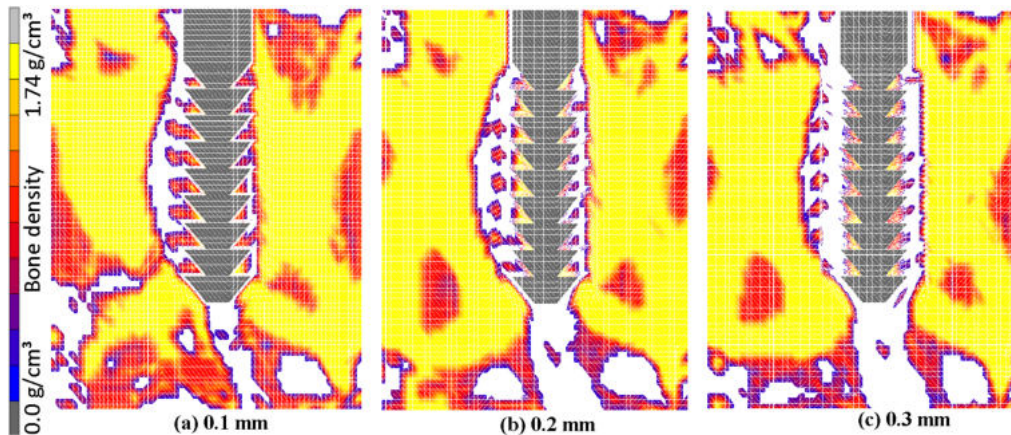
Figure 3.9: Influence of the thickness of the tissue types with 0.1 mm, 0.2 mm, and 0.3 mm after 100th iterations in phase 1.
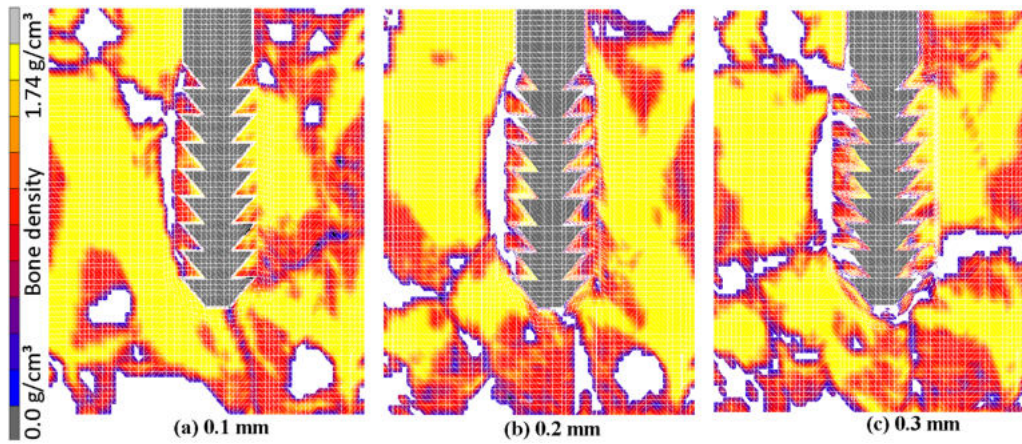
Figure 3.10: Influence of the thickness of the tissue types with 0.1 mm, 0.2 mm, and 0.3 mm after 100th iterations in phase 2.
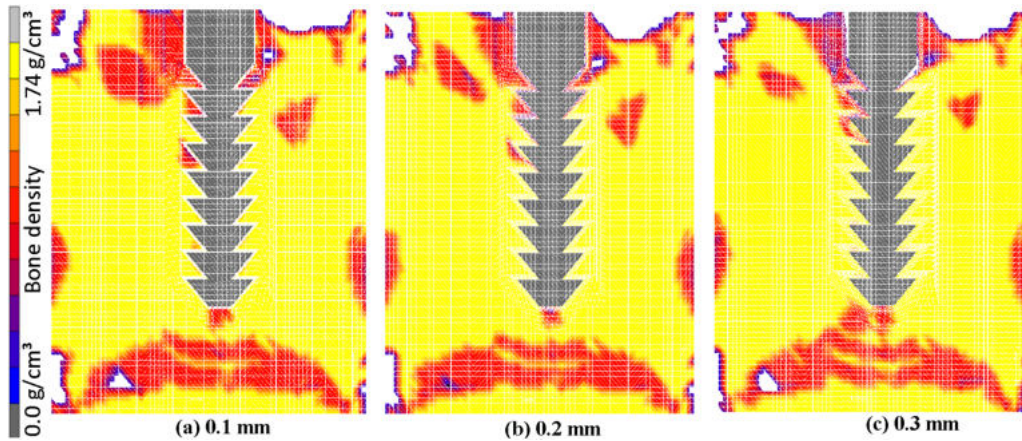
Figure 3.11: Influence of the thickness of the tissue types with 0.1 mm, 0.2 mm, and 0.3 mm after 100th iterations in phase 3.

The following paragraphs deal with the changes of different model results over the course of the iterative simulation process. The course of the mean density change, of the mean values of the strain energy density and of the mean value of the stresses in the bone are shown as curve plots versus the number of simulation cycles in Fig. 3.12, 3.13, and 3.14 for all three osseointegration phases. All results are presented with an EEL of 0.2 mm. Different thicknesses of tissue types of 0.1 mm, 0.2 mm, and 0.3 mm are presented in the graphs.

The mean values of the density changes in the whole model over the course of each iteration step are presented in Fig. 3.12. Most changes occur within the first 10 steps for all graphs, then it stabilizes to an almost constant level. After time step 25, density change was stable around zero in the graphics. The highest density changes were observed in the first steps of Phase 3, independent of the thickness of the osseointegration layer.

The mean values of the strain energy density for three different thicknesses of tissue types are presented in Fig. 3.13. Higher SED changes were observed in Phase 2 and Phase 3 at the beginning of time steps comparing with Phase 1. At the beginning of the simulations, SED decreased in phase 1 and phase 2. After that, the it increased in all phases and thicknesses. Nearby time steps 10, positive change obtained for all Phases in all thicknesses. Most changes observed within the first 20 steps for all graphs, then it stabilizes to an almost constant level. After time step 50, SED was stable in the graphics. Furthermore, there was an small curve with 0.3 mm in phase 2 at the time steps 80 and then it stabilizes too.

The mean values of the Equivalent von Mises stress are presented in Fig. 3.14 with three different phases and thicknesses of tissue types. The initial stress value was approximately 8 MPa, which rose to a maximum value of 16 MPa at time steps 10, then declined back to the initial value at time steps 15 and remained constant after that in Phase 1 and Phase 2. The peak stress value was obtained in time steps 10 in Phase 1 and Phase 2. More interesting behavior was observed for a stress rate as represented by the curve of Phase 3 in all graphics. Phase 3 has no high stress change after time steps 10 comparing Phase 1 and Phase 2.
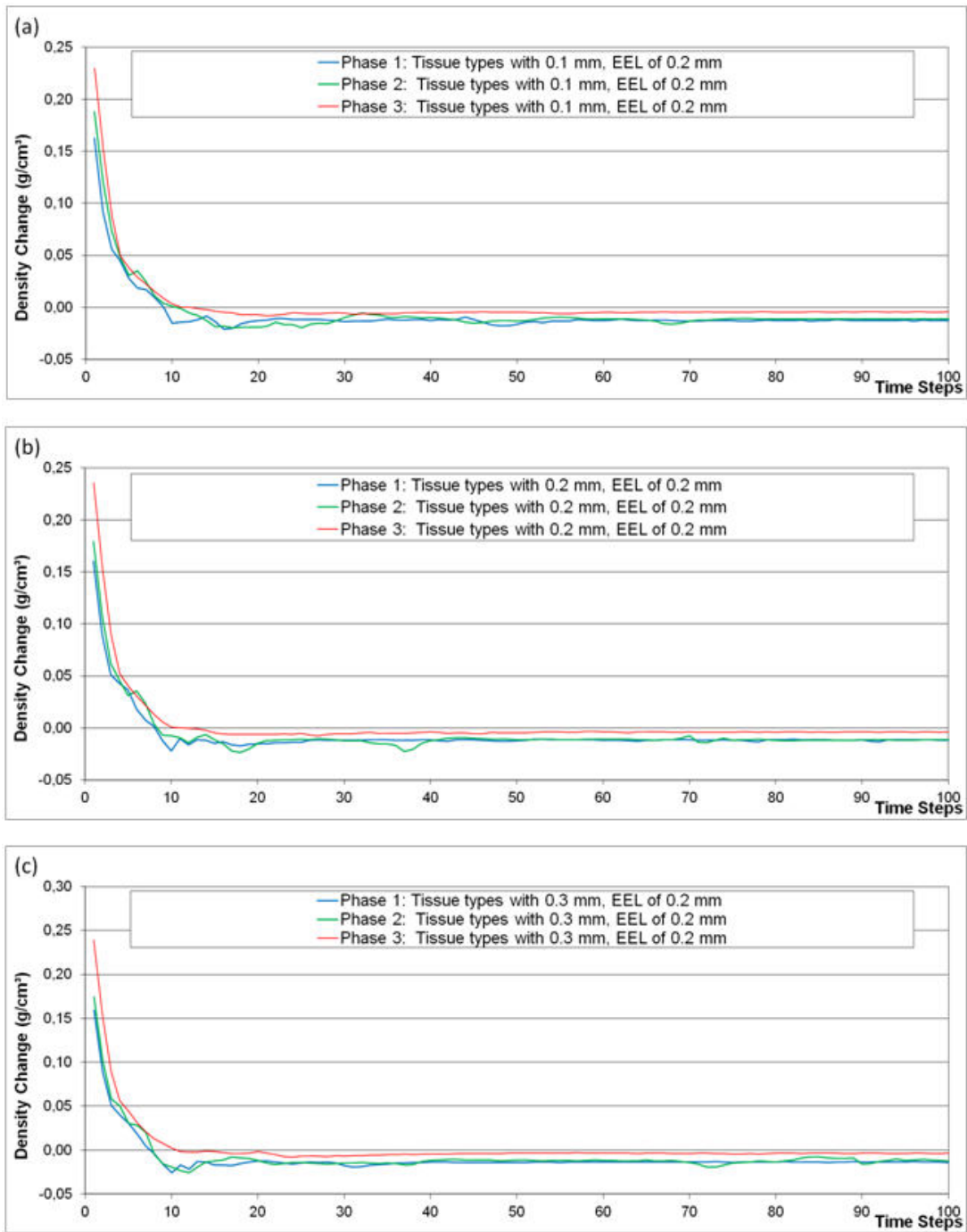
Figure 3.12: Density change histories under different osseointegration phases: Phase 1, Phase 2, and Phase 3 with tissue thickness of a) 0.1, b) 0.2, and c) 0.3 mm.
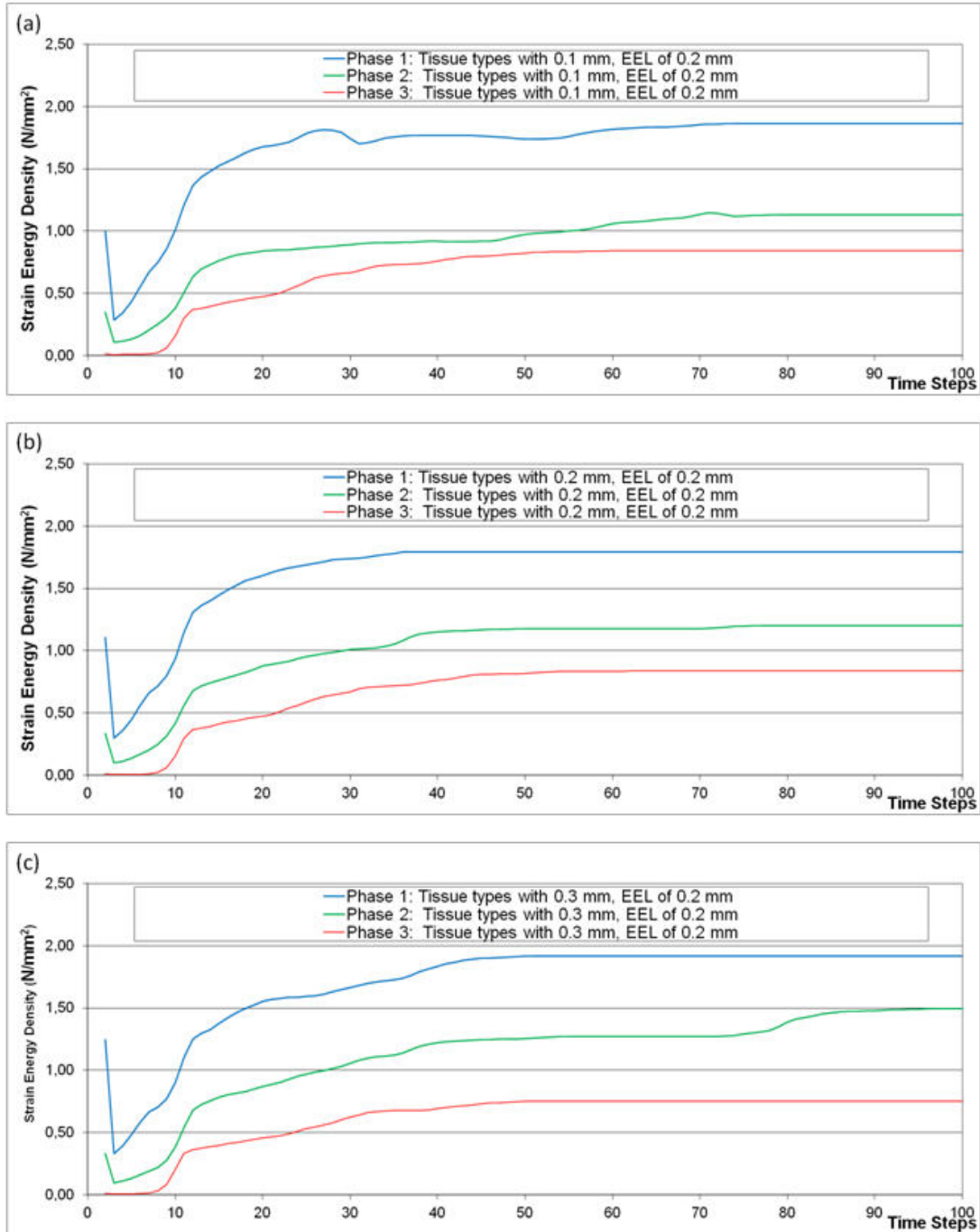
Figure 3.13: Strain energy density in Phase 1, Phase 2, and Phase 3 with tissue thickness of a) 0.1, b) 0.2, and c) 0.3 mm.

80
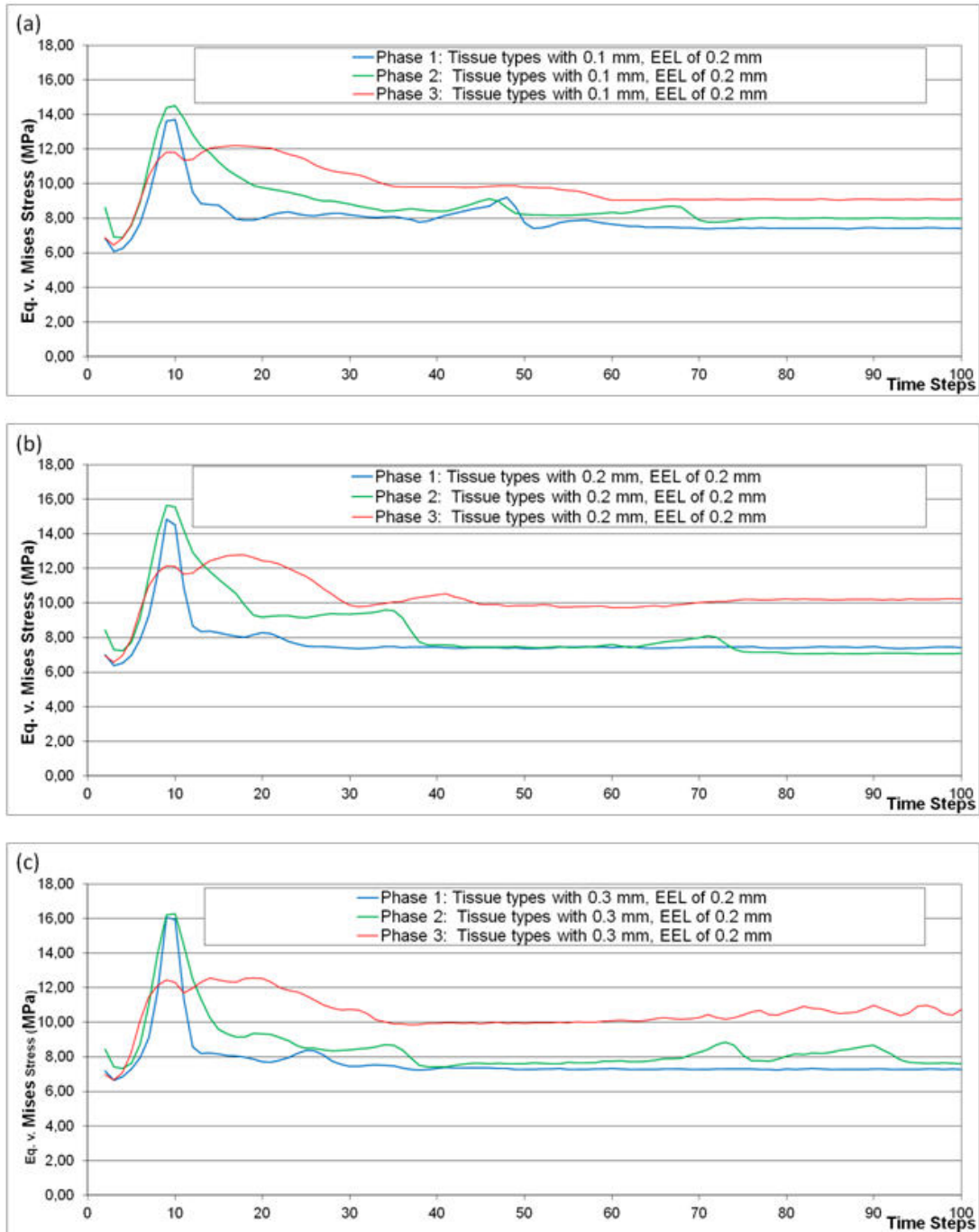
Figure 3.14: Equivalent von Mises stress in Phase 1, Phase 2, and Phase 3 with tissue thickness of a) 0.1, b) 0.2, and c) 0.3 mm.

81

3.1.8 Influence of Healing Phases with Homogeneous Bone

1- Simulations without healing phases

The first scenario was developed without healing phases. In figure 3.15, the model was created with an EEL of 0.2 mm, and muscle pressure was applied with 2 MPa. The maximum number of time steps was 300, becasue bone resorption was obtained with less time steps. The effect of Young's modulus of spongious bone is shown in figure 3.15, with 20 MPa and 300 MPa. Bone formation was obtained with Young's modulus of 300 MPa around the implant and neck of the implant comparing with Young's modulus of 20 MPa. But overloading resorption occurred in the lower part of the model in cortical and spongious bone with Young's modulus of 300 MPa, see Fig.3.15 (b).
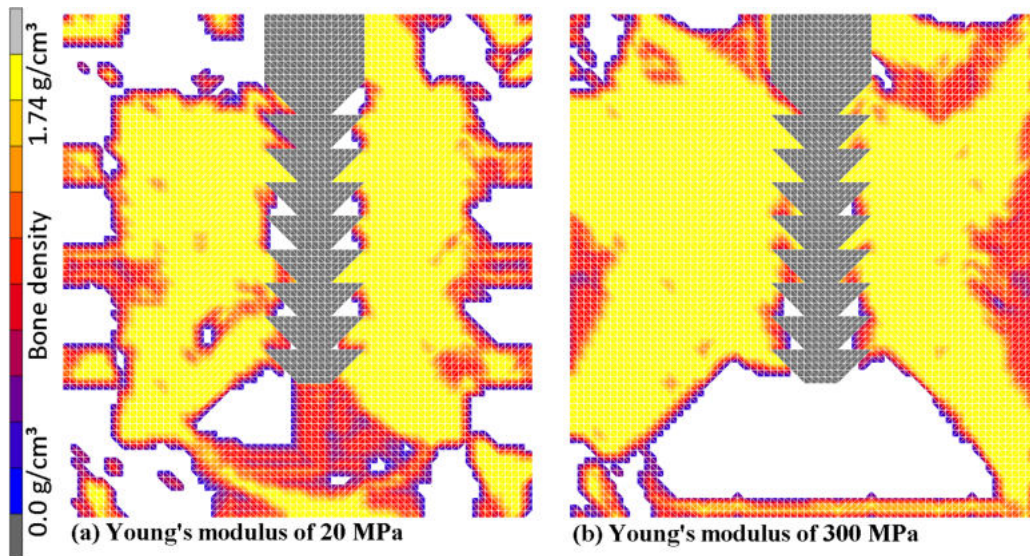
Figure 3.15: Variation of the initial Young's modulus of spongious bone with 20 and 300 MPa.

2- Simulations with healing phases

In the region of the trabecular bone, a grid represented the spongious bone. This was a different between this section and section 3.1.7. The following images show the bone density distribution after 300 time steps of bone remodeling of the healing phase for the three different healing states and the three different healing layer thicknesses. The bone density in all images is colour-coded to the same scale shown in figure 3.16. Figures 3.16, 3.17, and 3.18 are presented with EEL of 0.5 mm.

Osseointegration was achieved for a thickness of 0.1 mm in Phase 1, see Fig. 3.16, which corresponds to clinical observations. In the later healing stages, the thickness of the healing layer showed less influence. On the other side, new bone formation occurred around the implant with the thickness of 0.1 and 0.3 mm in Phase 2, see Fig. 3.17. Bone resorption was observed on the left side of the implant body with 0.2 mm. Furthermore, bone resorption occurred on the left side of the implant neck with 0.3 mm, see Fig. 3.17. Besides, bone reached maximum density around the implant with 0.2 and 0.3 mm comparing 0.1 mm, see Fig. 3.18. Bone resorption was obtained on the left side of the implant tip with 0.3 mm.
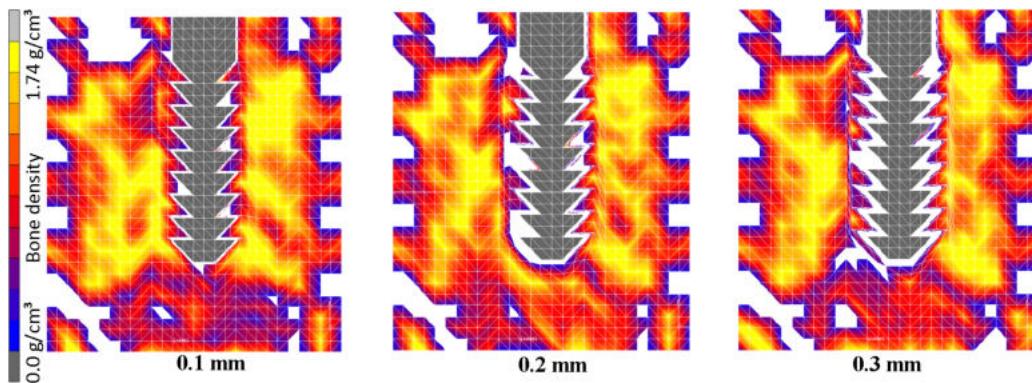
Figure 3.16: Phase 1- Immediately after implant insertion to two weeks, EEL of 0.5 mm. Better bone formation was obtained with thickness of 0.1 mm, comparing with 0.2 and 0.3 mm.
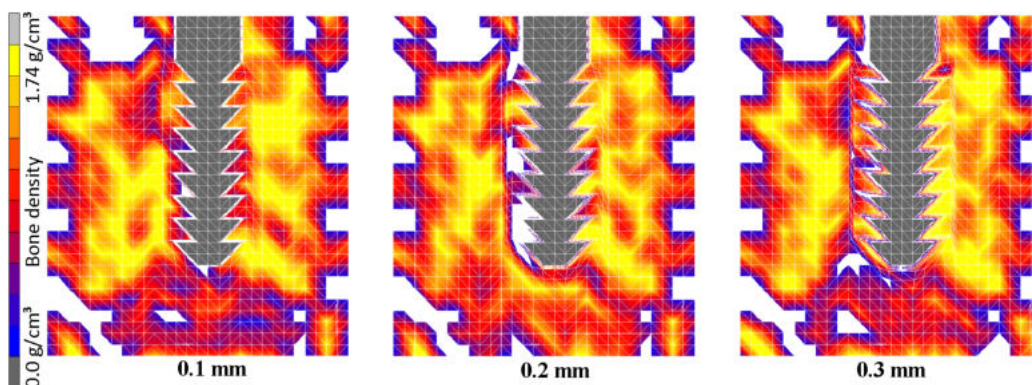
Figure 3.17: Phase 2- After two months, EEL of 0.5 mm. Bone formation occurred around the implant with a thickness of 0.1 mm.
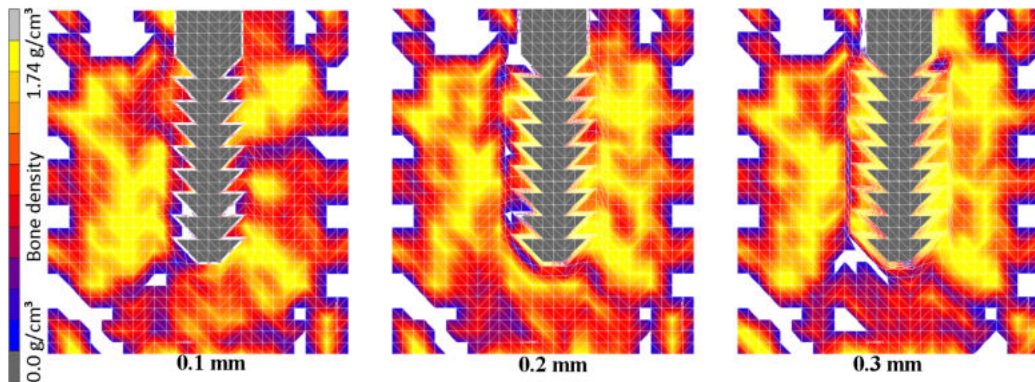
Figure 3.18: Phase 3- After four months, EEL of 0.5 mm. More dense bone was obtained with increasing the thickness of the layer. These could be explained with tissue layers in phase 3 having high Young's Modulus.

Figures 3.19, 3.20, and 3.21 show simulation results with EEL of 0.2 mm. Osseointegration was achieved with a thickness of 0.1 mm in the early loading phase 1 and phase 2, which corresponds to clinical observations. The thickness of the healing layer of 0.3 mm did not deliver nice result in phase 1 and phase 2. Only in phase 3, nice bone formation was observed with 0.3 mm, see Fig. 3.21. Comparing the muscle loads on the model, the bone density reached the maximum value on the cortical bone and outside of the spongious bone at 3 MPa.
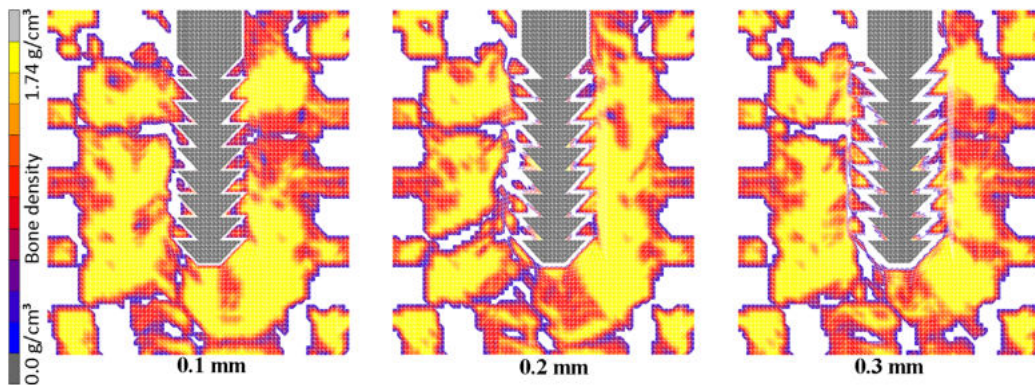
Figure 3.19: Phase 1- Immediately after implant insertion to two weeks, EEL of 0.2 mm. Bone resorption increased around the implant with increasing the thickness of the layer.
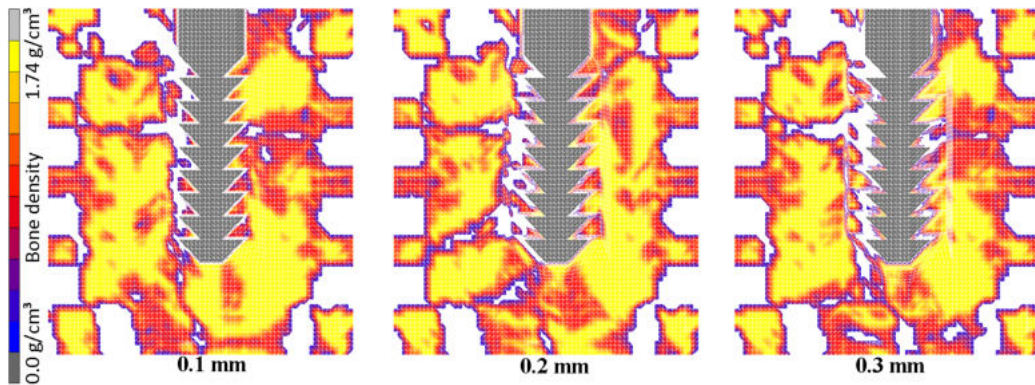
Figure 3.20: Phase 2- Situation after two months, EEL of 0.2 mm. Bone formation decreased when the thickness of layer increased.
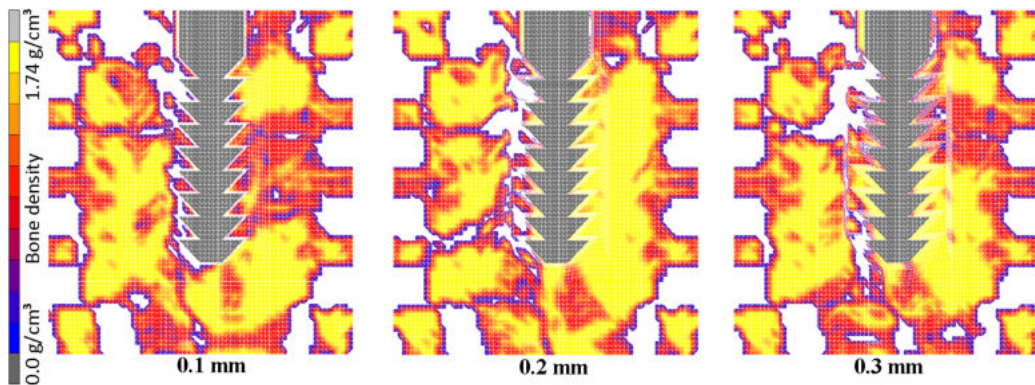
Figure 3.21: Phase 3- Situation after four months, EEL of 0.2 mm. Bone density reached the maximum value around the implant with increasing the thickness of the layer. Bone formation increased when the thickness of layer increased.

3.1.9 Influence of Time steps

Further parameters were varied during the bone remodeling simulations in this section. One of them was changing the scaling factor of 0.33 and 0.01 with the number of time steps of 300 and 10,000, respectively. The scaling factor is the percentage of applying density to the model. The critical scaling factor is that factor, at which the resulting maximum possible density change is too small to move the current element from its current material group into an adjacent material group. The aim of this section was comparing different scaling factors during the osseointegration. The total force was applied to the implant at 20 ° from its long axis with 100 N. Muscle loads

were simulated as 2 MPa of compression from both, labial and lingual sides of the model. Young's modulus of spongious was 300 MPa. Bone was too stiff when we used Young's modulus above 300 MPa during these simulations.

Fig. 3.22 shows the results of maximum time steps of 300. The scaling factor was 0.33 for this simulation. Bone resorption occurred on the left upper side of the model in cortical bone and also in the lower part of the model directly under the tip of the implant.

Fig. 3.23 shows the results with scaling factor 0.01. The maximum time steps were 10,000. Bone formation was observed in both cortical and spongious bone, especially around the implant. The upper part of the model reached the maximum density in the area of the cortical bone after approximately 300 time steps. There was no significant change obtained in the bone between the time steps 300 and 10,000. Comparing these two results show that with more time steps bone formation is increased. Increasing the speed of the simulation with time steps and scaling factor increases the bone resorption.

As a result, more bone formation was observed with scaling factor of 0.01 in Fig. 3.23 compared with scaling factor 0.33 in Fig. 3.22. Bone resorption was obtained below the implant tip in the results with scaling factor of 0.33, see Fig. 3.22 although bone formation was observed with scaling factor of 0.01, see Fig. 3.23.
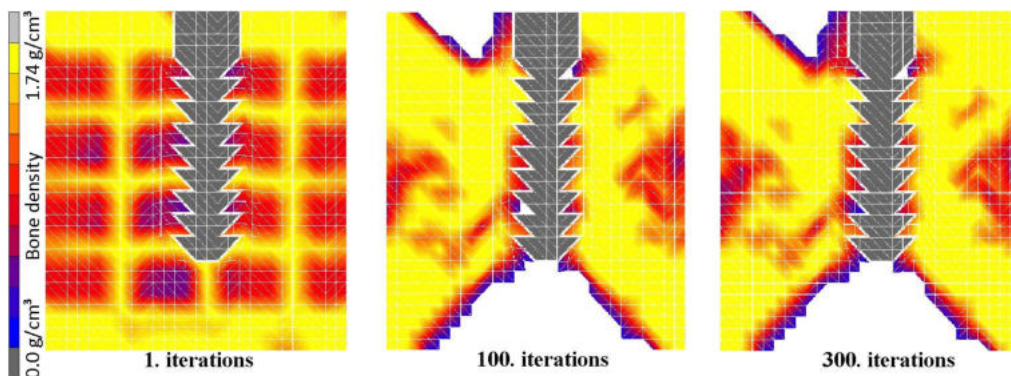
Figure 3.22: View of the results to show the effect of the maximum 300 time steps.
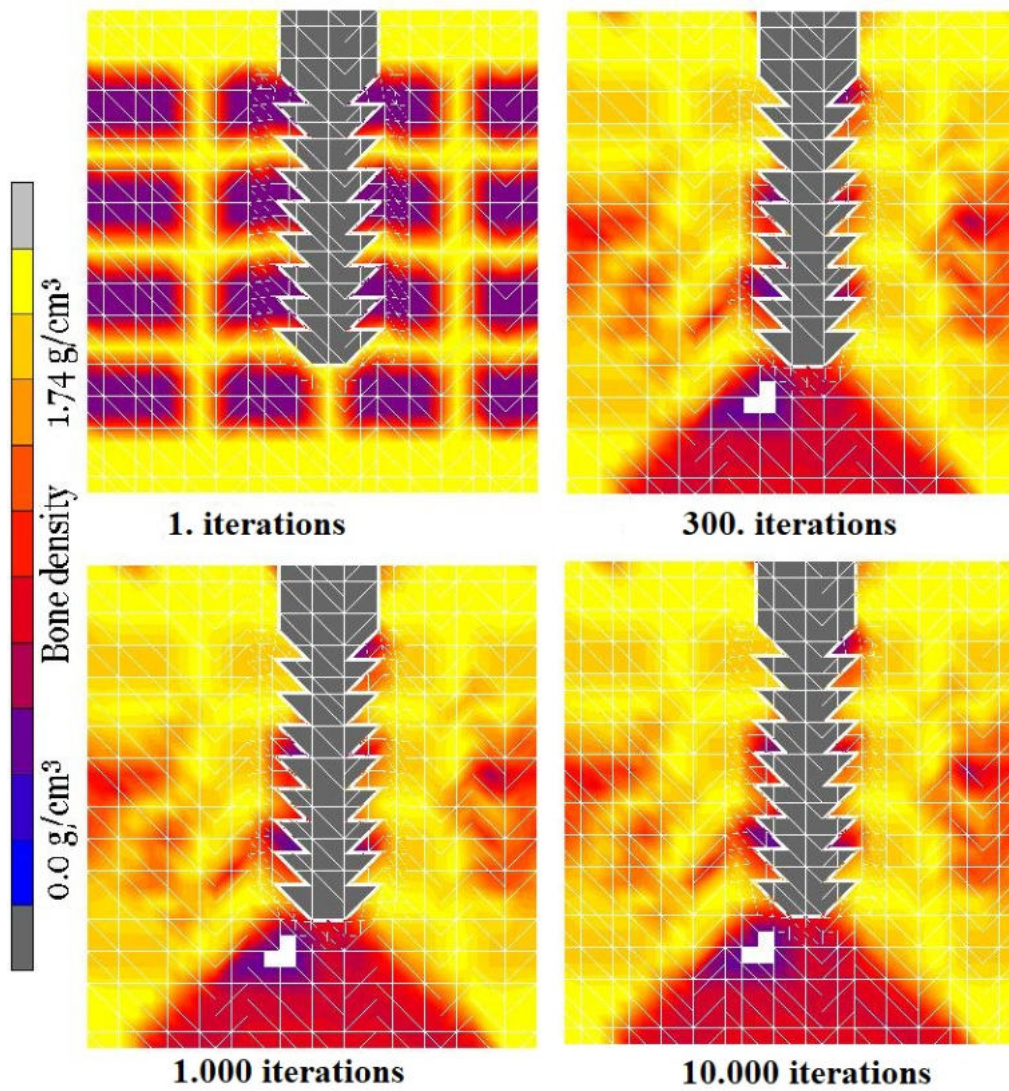
Figure 3.23: Sequence of bone remodeling results of 1, 300, 1,000 and 10,000 time steps.

3.2 Sensitivity Tests with 3D Models

Bone density distribution with the different mechanical parameters is presented after 1, 25, 100, and 300 time steps. Results for total deformation, and resulting stresses (stress, total strain, total strain energy density, total displacement between bone-implant interface) were evaluated.

3.2.1 Influence of the Bone Remodeling Theory

A longitudinal cross-section of 0.1 mm thickness throughout the bone and application of the bone remodeling algorithm in a simplified 3D model is shown in figure 3.24. Bone density increased around the implant with the time steps. The outer of the model reached steady state, generally in cortical bone.

Figure 3.25 presents the strain distribution with different time steps, respectively. The maximum equivalent strain recorded for the bone around the implant is shown after 25. iteration. There were also several strain areas both buccally and lingually and also around implant threads. However, areas of lower strain values were also seen around several threads, and the implant's neck of 100.iterations. However, there was no change results with 300. iterations.
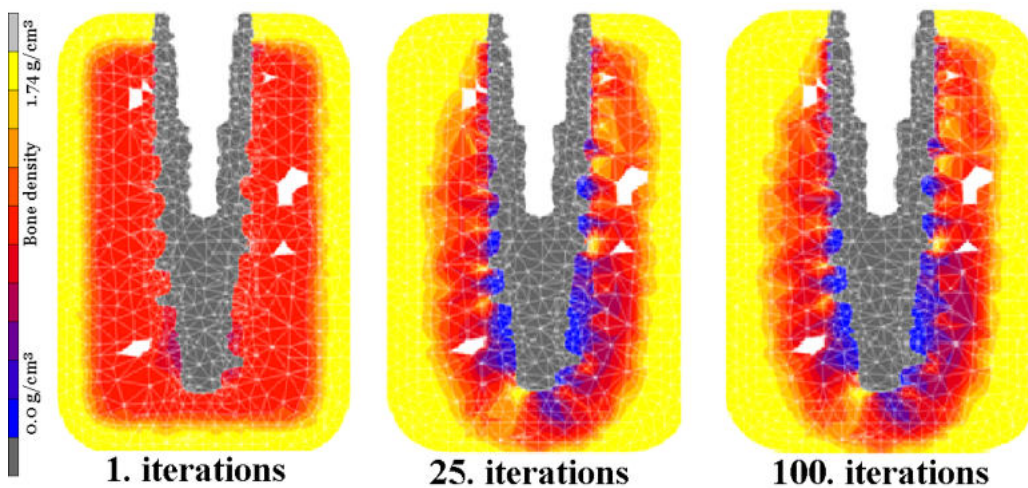
Figure 3.24: A cut through the model shows the density distribution after 1, 25, and 100th iterations in 3D models.

88
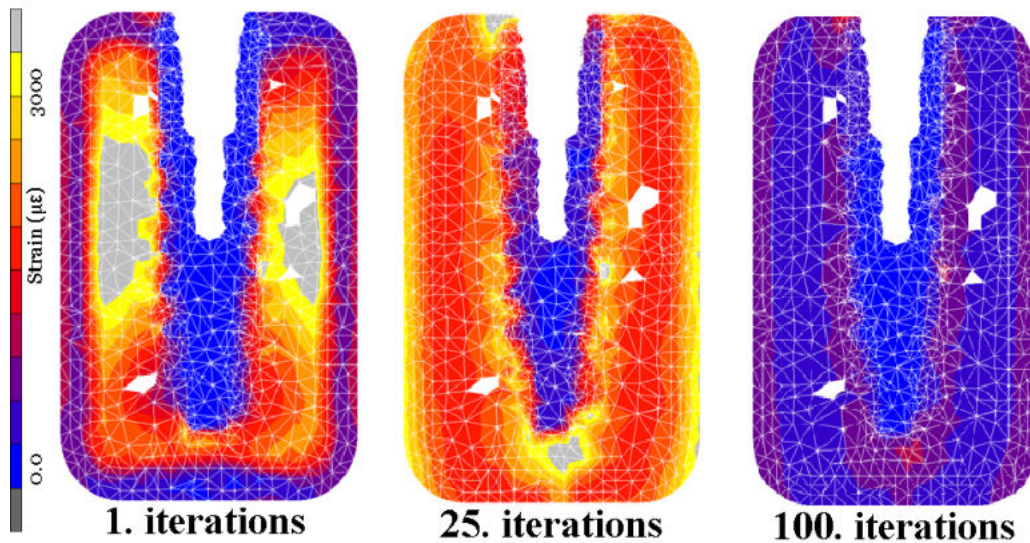
Figure 3.25: Distribution of the equivalent of total strain ($\mu\varepsilon$) after 1, 25, and 100 iterations in 3D models.

3.2.2 Influence of the Muscle Forces

The influence of muscle forces are presented in figure 3.26 and figure 3.27. Figure 3.26 and figure 3.27 present bone formation under different muscle forces between 0.5 and 2.5 MPa. Density distribution within the range of 0.4 to 1.74 g/cm^3 was used to demonstrate the results. A total force of 100 N was applied to the implant at 20 ° from its long axis. Muscle forces were applied on the lingual and labial sides, as compression and tension. Young's modulus of spongious bone was 300 MPa. More bone formation was obtained with muscle forces up to 2.5 MPa, which means that bone density increases when the muscle force increases.

Figure 3.28 shows the results of effect of the muscle force of 1.5 MPa which is presented also in Fig. 3.27. The aim to show this figure was presenting the different views of muscle force 1.5 MPa, a cut through the model on the left side, and total model with all bone on the rigth side are presented in Fig. 3.28. Only densities within the range of 0.4 to 1.74 g/cm^3 are presented below. Bone formation was observed in cortical and spongious bone in the model. Good connection was obtained between bone and implant on the middle thread of the implant and the neck of the implant. Bone resorption was highly increased with the muscle loads higher than 4.0 MPa. That explained that the ideal muscle loads should be between 1.5 and 4.0 MPa for

the bone remodeling simulations during the remodeling process.
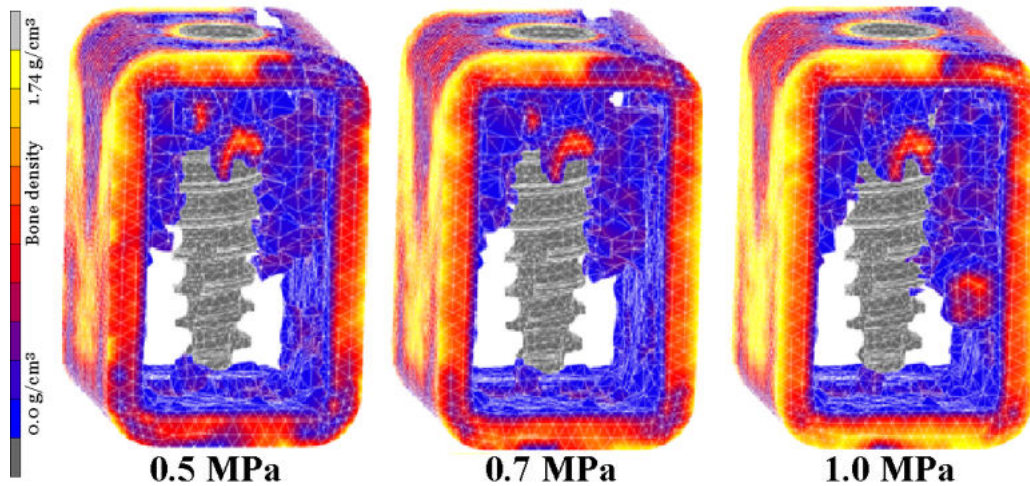
Figure 3.26: Variation of muscle pressure: 0.5 - 1.0 MPa in 3D models.
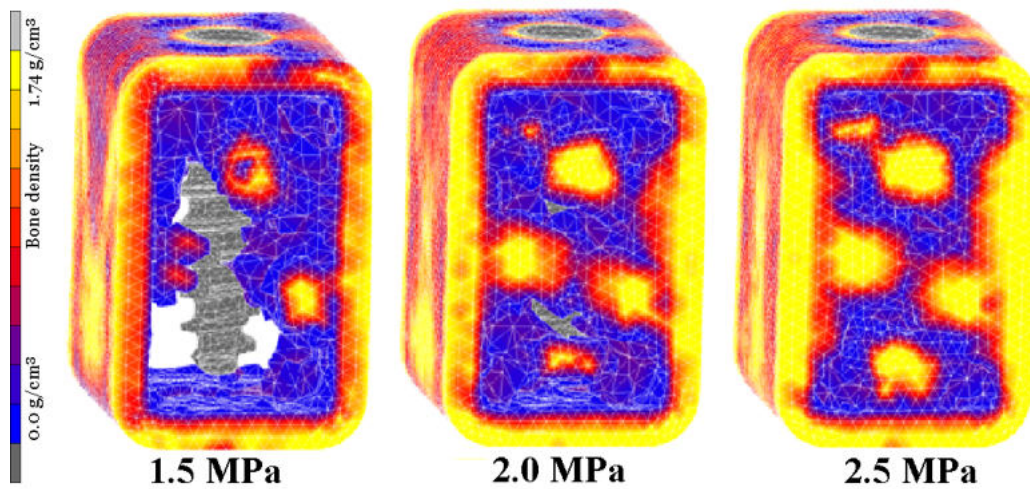
Figure 3.27: Variation of muscle pressure: 1.5 - 2.5 MPa in 3D models.

3.2.3 Influence of the Boundary Conditions

Two steps were done in this section:

1. Only the spongious bone was remodeled during the simulations.
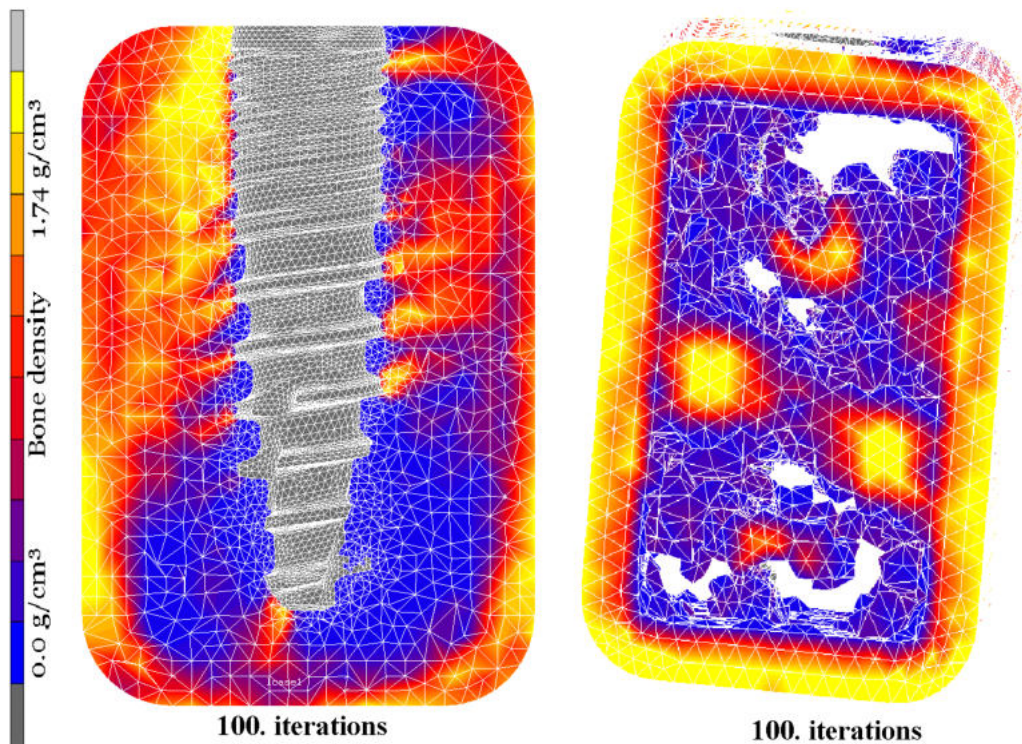
Figure 3.28: Variation of muscle pressure of 1.5 MPa using extra fixation nodes under the model.

2. The whole bone (cortical and spongious) was remodeled.

1. Remodeling of spongious bone

Figures 3.29, 3.30 and 3.31 show density distributions after 1 and 100 time steps. A longitudinal cross section of 0.1 mm thickness throughout the bone and application of the bone remodeling algorithm in a simplified 3D model is shown in these figures. Spongious bone was remodeled during the simulations in this section. Muscle forces were applied with 2 MPa from lingual and labial sides as compression to both sides, and as compression on the one side with tension on the other side. Figures 3.30 and 3.31 were fixed bottom of the model from cortical bone. The additional difference between these two models was the muscle forces. Figure 3.30 had muscle forces as compression from both lingual and labial sides with 2 MPa. Figure 3.31 had muscle loads as compression from lingual and tension from labial sides with 2 MPa.

The density distributions for Fig. 3.29 and Fig. 3.30 were similar around the neck of the implant. Density reached the maximum value on the tip of the implant in spongious bone in Fig. 3.30 and Fig. 3.31. This can be explained with the effect of the fixation conditions which was done from the lower part of the cortical bone. Besides, good connection was obtained between spongious bone and implant on the middle screw pitches of the implant in all three results, see Fig. 3.29, 3.30 and 3.31.

Significantly, new bone formation observed more on the lingual side than on the labial side in these three simulations. Similar results were obtained by Hasan [240]. In our study, more bone formation occurred in the area of the implant tip with more fixation nodes from the lower part of the cortical bone than the normal fixation which were just done with some point of spongious bone and outsides of cortical bone see Fig. 3.30 and Fig. 3.31. That means the fixation of the model is not only affecting the density but also plays a vital role around the implant.

Further, the difference between the compression and tension forces was also simulated. Figure 3.30 and 3.31 present the effect of the compression and tension muscle forces. Comparing both figures, new bone formation occurred at some point of the spongious bone when compression force applied to the model in both lingual and labial sides, see 3.30. Besides this, bone resorption was obtained in the middle part of the implant surface when compression force and tension forces at the same time applied in labial and lingual sides, respectively.
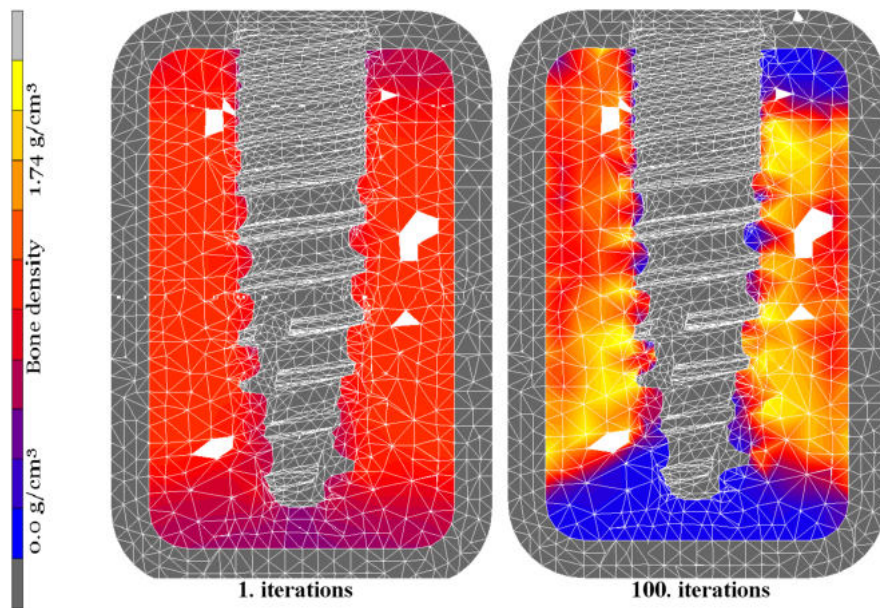
Figure 3.29: Density distribution after 1 and 100 iterations in 3D models. Muscle forces: compression from lingual and labial sides with 2 MPa.
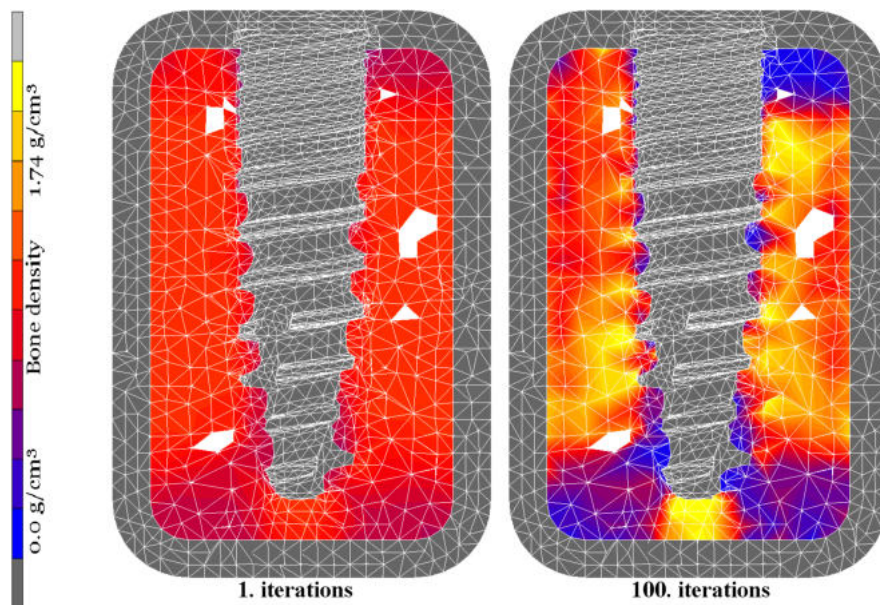
Figure 3.30: Density distribution after 1 and 100 iterations in 3D models. Additionally, model was fixed from the bottom of cortical bone. Muscle forces: compression from lingual and labial sides with 2 MPa.
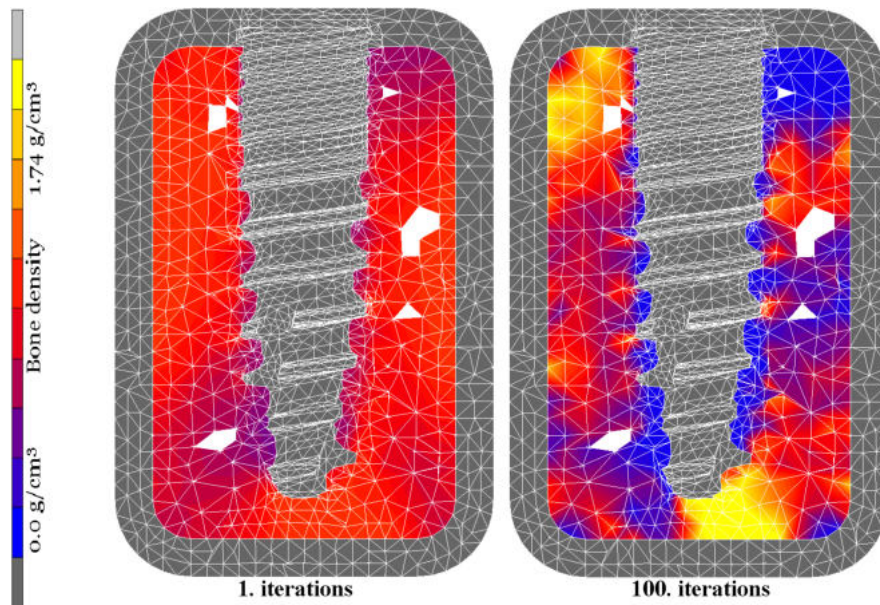
Figure 3.31: Density distribution after 1 and 100 iterations in 3D models. Additionally, model was fixed from the bottom of cortical bone. Muscle loads: compression from lingual and tension from labial sides with 2 MPa.

2. Remodeling of the whole bone

Figures 3.32, 3.33 and 3.34 show density distributions after maximum time steps of 100 iterations. All cortical and spongious bone were remodeled during the simulations in this section. Muscle loads were applied with face loads of 2 MPa from lingual and labial sides. Two views are presented in each figure. On the left side is a view of a longitudinal cross-section of 1.0 mm thickness throughout the bone. On the right side, the whole model without implant presented to show the bone formation in all cortical and spongious bone.

Spongious and cortical bone had bone formation at the neck and the middle part of the implant in Fig. 3.32. Bone resorption occurred around the head of the implant in spongious bone in Fig. 3.32. Fig. 3.33 and 3.34 show an ideal bone formation in all cortical and spongious bone especially around the whole implant body. Part of the bone reached the maximum density under the head of the implant in Fig. 3.34. The way of applying muscle loads to the model could have affected the results for lower density distribution at the left-below part of the model in spongious and cortical bone in Fig. 3.34.

On these figures, a nice view of bone formation can be observed in all of the models with cortical bone, spongious bone, and also around the implant. That can be explained by that all bone has to be in the remodeling process under the mechanical stimulus. After changing the fixation conditions, the density distribution changed as well.

Comparing the 1. and 2. steps in this section: more bone formation was obtained in both cortical and spongious bone and also around the whole implant body when the cortical bone also remodeled with spongious bone during the simulations.
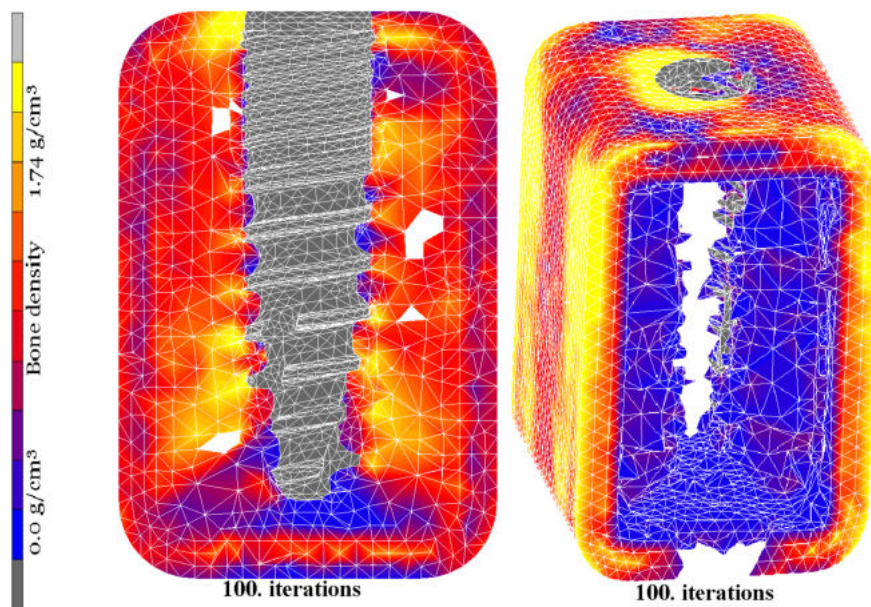
Figure 3.32: Density distribution after 100th iteration in 3D models. Muscle force: compression from lingual and labial sides with 2 MPa.
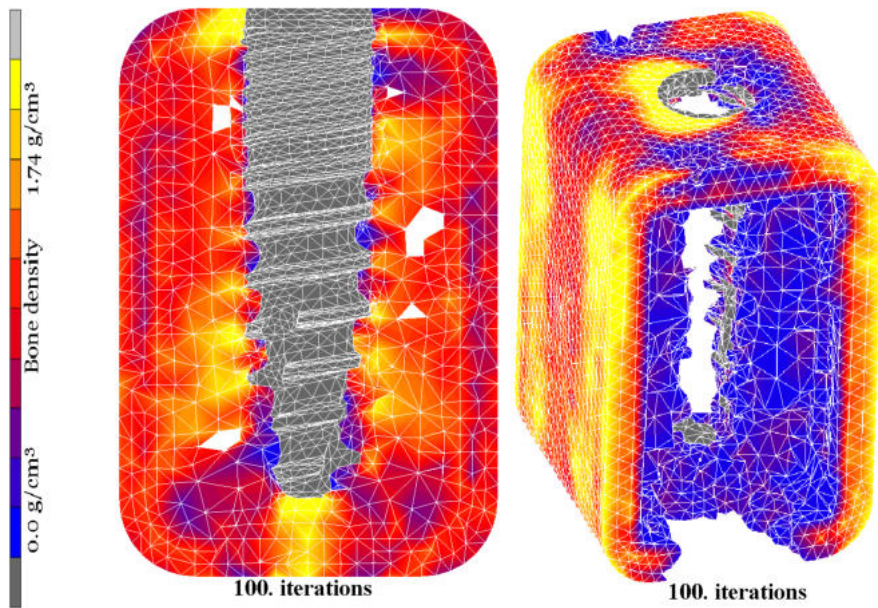
Figure 3.33: Density distribution after 100th iteration in 3D models. Additionally, model was fixed from the bottom of cortical bone. Muscle force: compression from lingual and labial sides with 2 MPa.
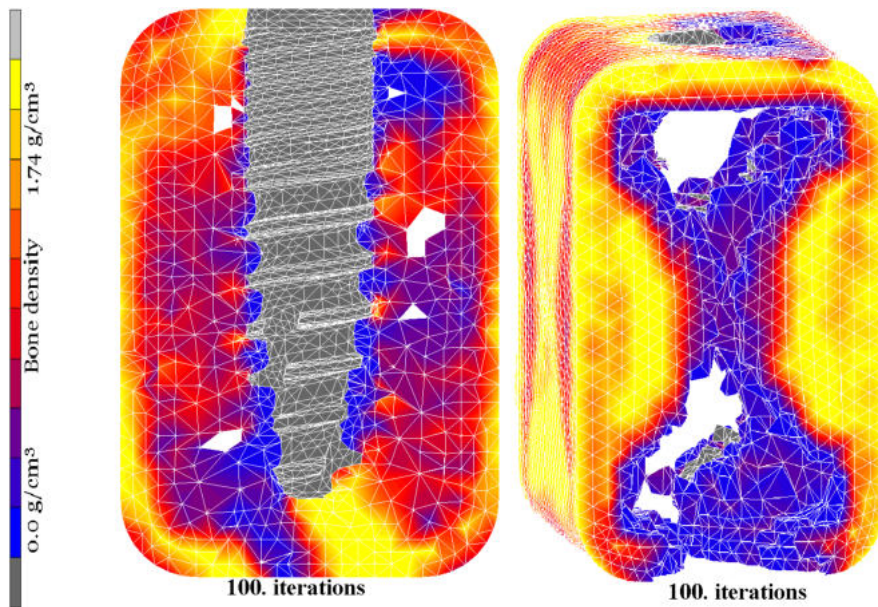
Figure 3.34: Density distribution after 100th iterations in 3D models. Additionally, model was fixed from the bottom of cortical bone. Muscle force: compression from lingual and tension from labial sides with 2 MPa.

3.2.4 Influence of the Element Size

The previous simulations were done with an EEL of 1.0 mm. For this section, the model was meshed with an EEL of 0.5 mm to compare with previous results. Figure 3.35 shows the density distribution from the 1. time steps and the maximum 100. time steps. The whole model is also presented in figure 3.35 to show the inner and outside of the cortical and spongious bone. New bone formation is observed around the implant.

Comparing the Fig. 3.32 and Fig. 3.35: the differences between these two simulations were EEL and muscle loads. Fig. 3.35 was generated with EEL of 0.5 mm and muscle loads were applied with face loads as compression and tension from labial and lingual sides. On the other hand, muscle loads were applied as compression from both labial and lingual sides in Fig. 3.32. More bone formation was obtained in spongious bone and around the implant in Fig. 3.35. Part of cortical bone reached maximum density in Fig. 3.35. Despite, there was an overload resorption under the head of the implant in spongious bone in Fig. 3.32, bone reached the maximum density in the same area in Fig. 3.35.
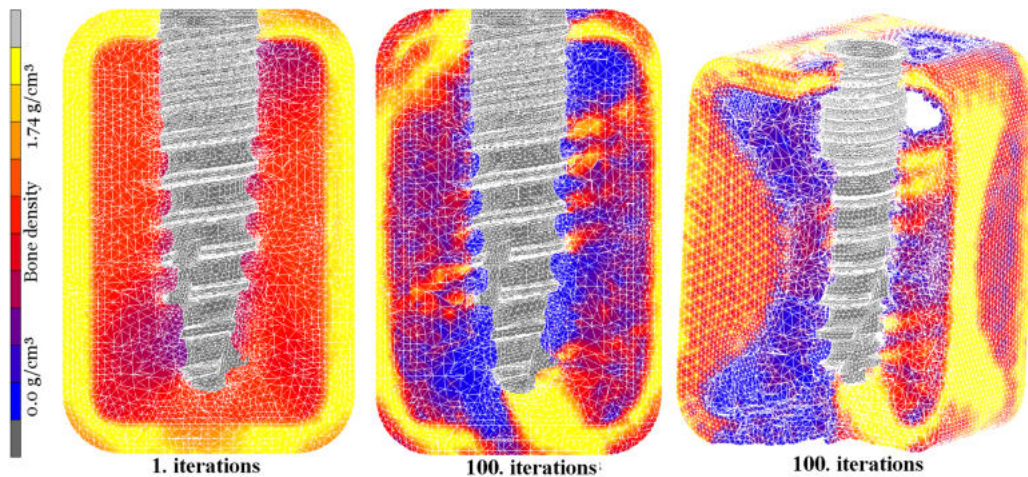
Figure 3.35: View of density distribution after 1 and 100th iteration in 3D models. The mesh of the model was generated with EEL of 0.5 mm. Model was fixed from the bottom of cortical bone. Muscle loads were applied with the face loads as compression from lingual and tension from labial sides of 2 MPa.

3.2.5 Influence of the Bending Force

Bending forces were applied to the models which were meshed with EEL of 1.0 mm. The total force was applied to the implant at 20 ° from its long axis with 100 N for all simulations. As a different parameter, the fixation was applied to the backside of the model.

Figure 3.36 presents the results of bending force of -10 N in Z direction with muscle loads of 1.5 MPa for compression and tension on lingual and labial sides. Figure 3.37 shows density changes with bending force of -100 N in Z direction with muscle loads of 1.5 MPa as compression and tension from both labial and lingual sides. The density increased when the bending force increased too. Bone formation was obtained between bone and implant pitches in both figures 3.36 and 3.37. Cortical bone reached maximum density in Fig. 3.37 comparing Fig. 3.36.

In the grand scheme of these results, a reveal interesting bone formation observed between the bone and implant pitches in the bone remodeling simulations. This was also observed with muscle loads of 1.5 MPa in Fig. 3.27. All boundary conditions except bending forces were the same for all these three figures 3.27, 3.36 and 3.37. There was overload resorption on the lower part of the spongious bone in Fig. 3.27 comparing the results with bending forces. The bending forces significantly could mean impact on the bone formation during the bone remodeling simulations. With increasing bending loads from 10 to 100 in Z direction, bone reached maximum density in the cortical bone, see Figure 3.36 and figure 3.37.
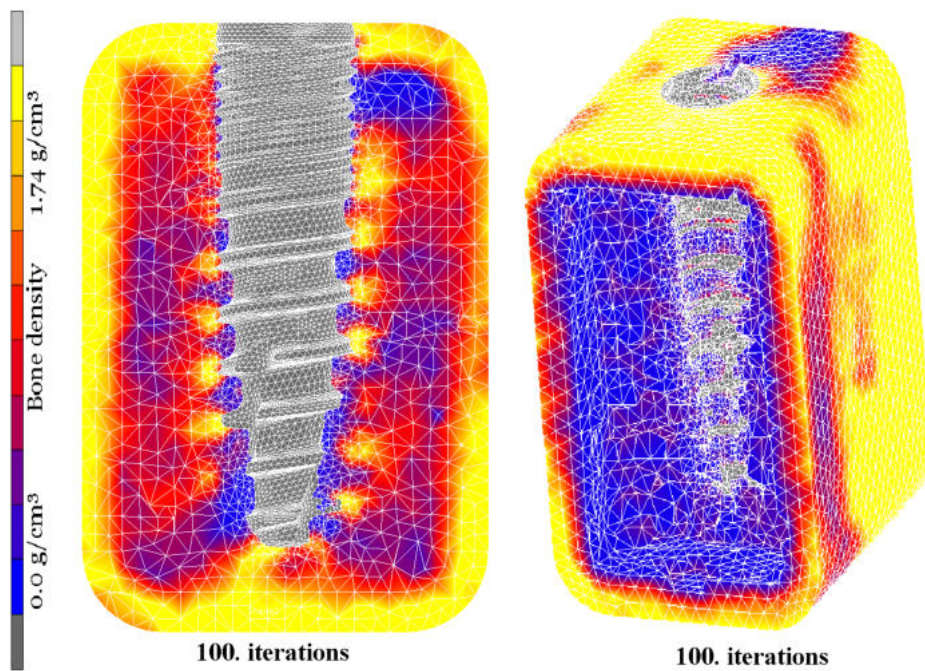
Figure 3.36: Density distribution with bending force of -10 N in Z direction.
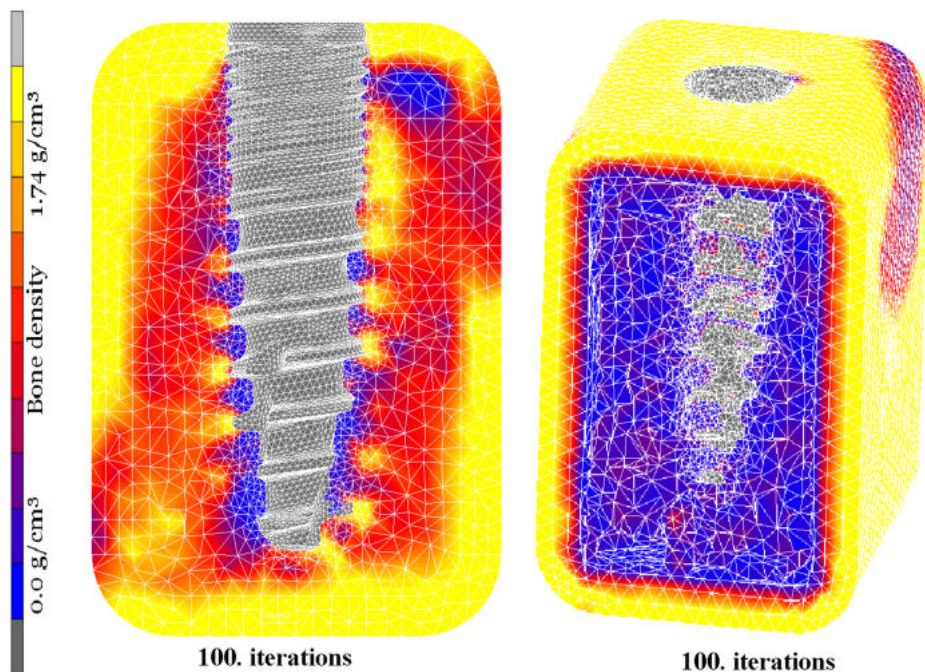
Figure 3.37: Density distribution with bending force of -100 N in Z direction.

99

As the next step, the bending forces were additionally applied to the model at the same time in the Y direction and the Z direction.

The EEL was 1.0, and density distributions after maximum time steps of 100th iterations were presented in this section. All cortical and spongious bone were remodeled during the bone remodeling simulations. Muscle loads were applied with face loads of 1.5 MPa from labial and lingual sides as compression and tension, respectively. Additionally, as a different parameter, the fixation was used to the backside of the model. There are two views that are presented in each figure. On the left side is a view of a longitudinal cross-section of 1.0 mm thickness throughout the bone. On the right side, the whole model without implant is presented to show the bone formation in all cortical and spongious bone.

Figure 3.38 shows the density changes with the effect of the different bending forces, i.e. -10 N from Z direction and -50 N from Y direction. Bone formation occurred in this simulation. Muscle loads were used as 1.5 MPa as compression and tension. Density distribution presented in figure 3.39 with the effect of the different bending forces, i.e. -10 N from Z direction and -100 N from Y direction. Density reached the maximum value in part of the cortical bone. The bone resorption occurred in the some point of the middle thread of the implant when the bending forces were applied to the model in both Z and Y directions, see figure 3.38 and figure 3.39.

In addition to boundary conditions, bending forces were applied in Z direction and in Y direction in figures 3.38 and 3.39 comparing with Fig. 3.27. More actively bone formation was obtained in both cortical and spongious bone in Fig. 3.38 and 3.39 in comparison with Fig. 3.27. Maximum density observed in part of cortical bone in both Fig. 3.38 and 3.39 beside Fig. 3.27. Bending forces in both Z and Y directions could have lead to it.

Comparing the results of figures 3.27, 3.36 and 3.39: the best bone formation was obtained in figure 3.36 and the reason can be explained with the bending force of -10 N in the Z direction. Pitches of the implant had good connection with the spongious bone in this figure comparing with figures 3.27 and 3.39. Resulting in thicker cortical bone in the corner of the model reached the maximum density in Fig. 3.39 by comparison with figures 3.27 and 3.36. Extra bending force of -100 N in Y direction could have caused this influence.
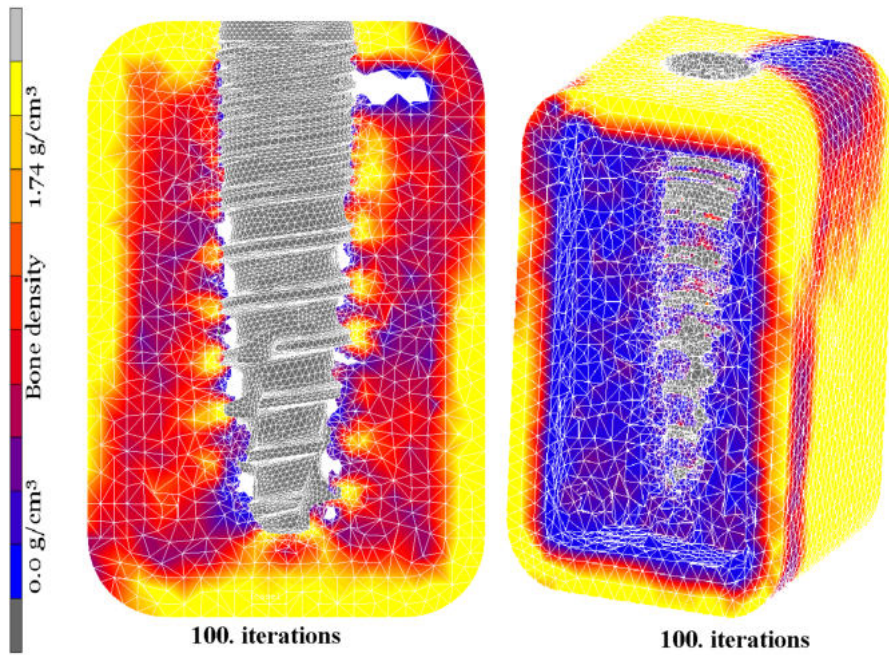
Figure 3.38: Density distribution with bending force of -10 N in Z direction and -50 N in Y direction.
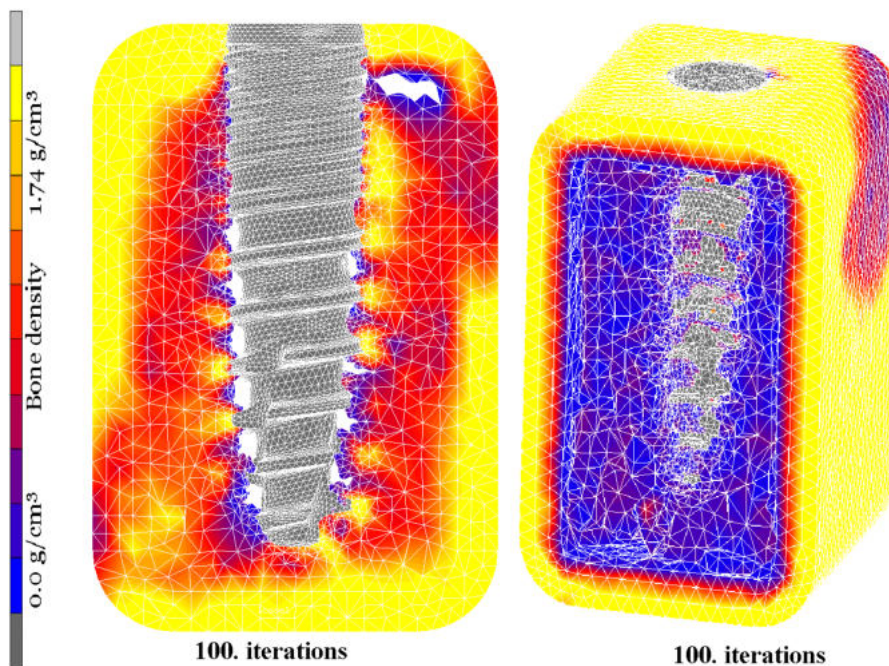
Figure 3.39: Density distribution with bending force of -10 N in Z direction and -100 N in Y direction.

3.2.6 Influence of the Fixation

The effect of the different fixations is presented in figure 3.40. The model was fixed from two points, which were created 20 cm far from the model. The connection between these two nodes and bone was made with the node in the surface of the bone.

As a result, the bone formation was obtained on the right upper side of the implant with muscle loads of 1.5 MPa in both compression and tension from the lingual and labial sides, respectively. On the other hand, the outer edge of the cortical bone reached maximum density, as shown in Fig. 3.40 with yellow color. Overloading resorption observed on the lower - left side of the implant in the spongious bone. The effect of the different fixation could lead to bone resorption, as shown in the figure.
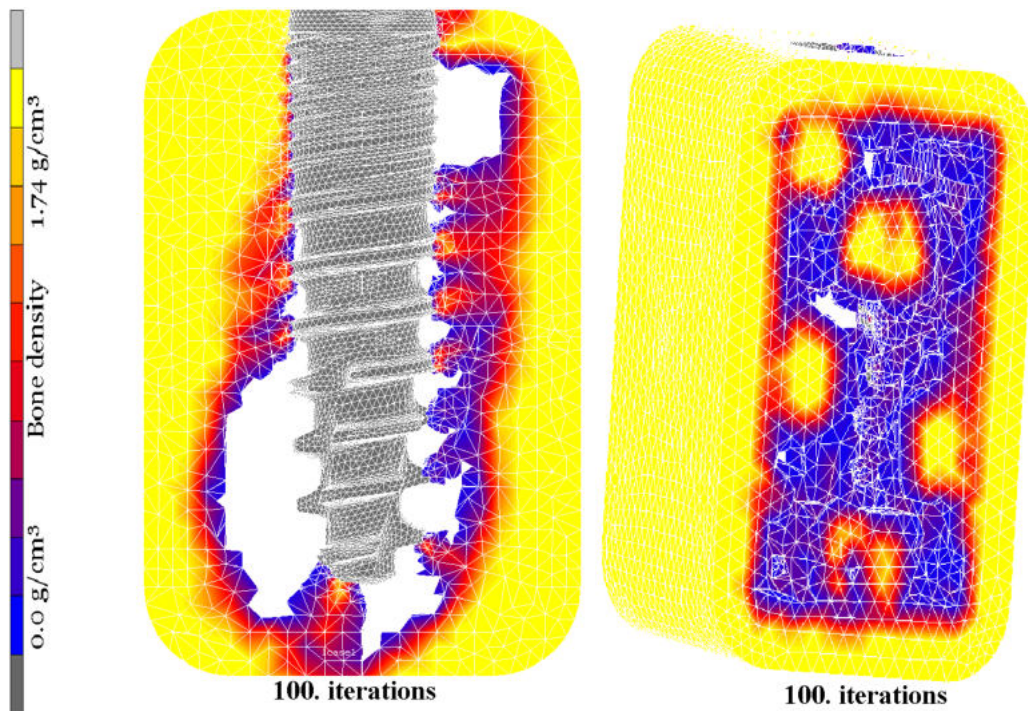
Figure 3.40: View of density distribution with different fixation. Muscle loads of 1.5 MPa: compression and tension in labial and lingual sides, respectively. EEL was 1.0.

3.2.6.1   Influence of the Implant Geometry

The effect of the mini dental implant under different muscle loads were simulated. Figure 3.41 shows the density distribution of muscle loads with 1 MPa as compression and tension from both sides of the model. There was no new bone around the implant and in spongious bone area under muscle loads of 1 MPa. Less muscle loads could have caused this bone formation in spongious bone.

The figure 3.42 shows results of density changes in mini dental implant under muscle loads with 3 MPa as compression and tension. Higher muscle loads lead to new bone formation around the implant. Furthermore, density reached the maximum values in cortical bone parts, which are shown in yellow color.

As compare the figures 3.41 and 3.42: Sufficient muscle loads play an important role in bone formation. Additionally, comparing the Fig. 3.27 and Fig. 3.42: As seen in these two results, there two different implant geometry and two different total force applied each model with also different muscle loads. These results showed us that sufficiently applying total force and muscle loads assisted new bone formation even the geometry of the implant and bone were different in these simulations.
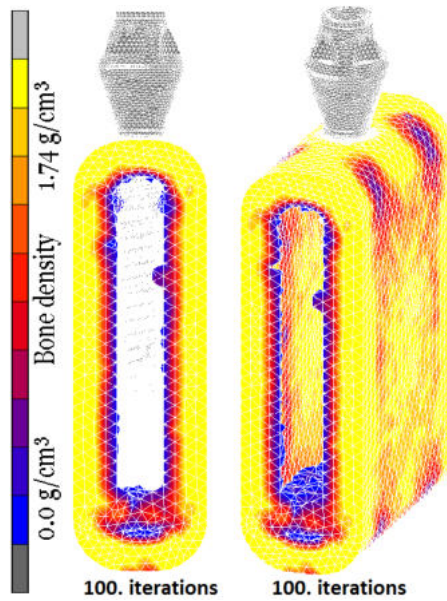
Figure 3.41: Density distribution with effect of muscle loads of 1 MPa as compression and tension in labial and lingual sides in mini implant. Total force was applied to the implant from Y direction with 10 N.
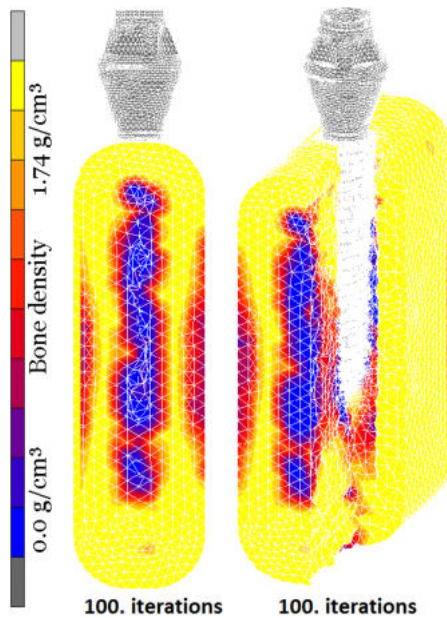
Figure 3.42: Results of density distribution with effect of muscle loads of 3 MPa as compression and tension in labial and lingual sides in mini implant. Total force was applied to this model as 10 N from Y direction.

104

4 DISCUSSION

4.1 Micro-Mobility of Dental Implants during Osseointegration

The goal of this study was to investigate the change of the implant stability in different phases of osseointegration while taking into account the ongoing bone remodeling processes. 2D FE models were used, which consisted of the dental implant with cortical and trabecular bone during different healing phases. A separate connective layer was modeled at the bone/implant interface, consisting of up to three different material components to allow the simulation of the healing process. Remodeling was simulated in 100, 300, and 10,000 time steps.

Different factors might affect the implant stability, such as implant design, the biomechanical properties of the local bone, and the preparation technique of the implant bed [245]. A previous study showed that the degree of the implant insertion is also important for implant stability [246]. Loading conditions, patient selection, and geometry of implant are important criteria for a successful loading procedure [236]. Many researchers have investigated micromotion using FEA to standardize the dental implant stability [247, 248]. Besides, another study showed that the important effect of high implant success rates and the successful osseointegration is the initial stability [249]. Furthermore, Hasan in 2011 compared the displacement of two implant designs, Tiolox® and tioLogic©. The mean displacements were 151 µm for Tiolox® and 145 µm for tioLogic© [240]. Some previous studies have worked on maintaining a constant displacement (micromotion) of the implant relative to the surrounding healing tissue [106, 250, 251].

In this study, implant stability was investigated during osseointegration. Results in figure 4.1 show the determined displacements in initial as well as the final iteration. Phase 1 showed the highest mobility compared to the other phases. Comparing the thicknesses of the osseointegration layer from phase 1, the displacement increased with the layer thicknesses. Using the 0.1 mm thickness model in the early phase as a reference, the horizontal and vertical mobility increased by 35 % and 18 %, respectively, in the 0.3 mm thickness model in the same healing phase. With ongoing healing, the later healing stages showed reduced mobility. Compared to the first healing phase, the vertical movement was reduced by 11 % in the second phase, and by 16 % in the third phase. Implant stability is an essential factor for long-term

implant treatment. This study shows how implant mobility and, in turn, the implant stability changes with different osseointegration phases and different layers around the dental implant during the bone remodeling simulation.
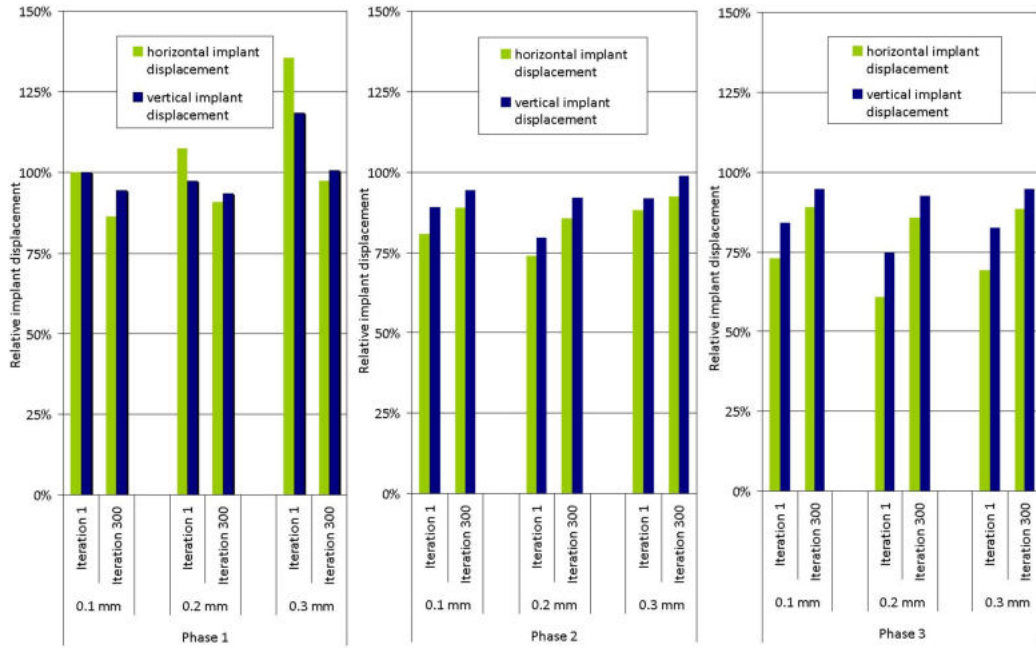
Figure 4.1: Horizontal and vertical implant displacements with healing phases in 2D FE models. The layer of 0.1 mm thickness model in phase 1 was used as a reference to compare the other thicknesses and phases in percentage.

4.2 Sensitivity Tests

The healing process of dental implants after insertion is complex. It was assumed that implant healing is comparable to indirect fracture healing of long bones. Hence, the aim of the present study was to simulate the remodeling process of the bone bed surrounding dental implants, considering different tissue layers until the osseointegrated state is reached. Some simplifications and assumptions were made and implemented in FEA owing to the complicated nature of the dental implant scheme to provide a reasonable approximation of the geometry, material, boundary conditions, and loading [252, 253]. All analyses were done based on the FEM results for stress and strain distributions in the jaw bone around dental implants and implant stability. The bone density changes as a function of the mechanical stimulus

are described from the remodeling theory as presented by Li et al. [146] and as extended in previous work by Hasan [240]. Different boundary conditions and bone remodeling parameters were applied to both 2D and 3D FE models. Additionally, various implant geometries were used with 2D FE simulations. For the implant geometry, two different implants were used for 3D FE analysis, i.e., tiologic© and a mini dental implant.

Several FEA studies have been done with the supporting bones using 2D as a rectangular block with the implant as a cylindrical object [254], and 3D models treated the mandible as an arch with rectangular section [255]. The interfacial stress gradients decrease with increasing diameter of implant and length at the cancellous region. On the other hand, interfacial stresses decrease with increase in the diameter of the implant at the cortical bone [162]. Changing the implant thread design can change the stress patterns in the surrounding bone, principally at the area of spongious bone of an osseointegrated implant [162, 256]. Large-thread implant designs improved bone anchorage mechanically and histologically compared with small-thread implants [257]. Furthermore, not only the length of the implant pitches and configuration but also the condition of bone may have an important influence on the stress dissipation [258]. Different thread designs might lead to different remodeling patterns [148, 258]. An important point should be noted that the first thread at the coronal part of the implant adjacent to the cortical bone bears more stress than the second and the third threads. All these results are based on animal and FE studies [254]. The stress distribution at the bone-implant interface is affected by the length and diameter of the implants [259]. Another numerical study showed that the behavior of the implants is affected by the design of length, diameter, density, and type of implant-abutment interface [260].

The effective connection between an implant and its surrounding bone is created from different mechanical factors. One of the basic key factors is the implant design. Besides, the optimal implant design itself can improve the bone formation and the stability of the implant. In the present study, different implant designs were used during the remodeling simulations in 2D and 3D models. FE simulations were done with threaded and non-threaded implants in 2D models. More new bone formation was obtained with threaded implants. The biomechanical behavior of implant design factors significantly influences density distribution at the cervical crestal bone region, which were defined in the models as cortical bone. However, due to the limitations of the idealized model geometry in the 2D model, it was not possible to obtain the perfect and anatomically correct structure in 2D FE models. Furthermore,

two implant designs were used during 3D FE simulations. A mini implant design was compared with the standard tioLogic© implant. In figure 3.42, the density distribution with the effect of muscle loads of 3 MPa is presented using the mini implant. Comparing tioLogic© implant and mini implant, higher stress values were observed with the mini implant. Another point should be noted that this study showed a high risk of overloading of bone for mini implants. Additionally, more homogeneous distribution was obtained with tioLogic© implants than with mini implants.

Besides, many studies have been performed using three different types of material properties in FE modeling; isotropic and orthotropic [261], transversely isotropic [262]. Young's modulus and Poisson's ratio are required for isotropic materials because isotropic means that the material properties are identical in all directions. Most of the studies are done with homogeneous, isotropic, and linear elastic materials [263]. The bone nonetheless reacts like an anisotropic material [264] and shows different mechanical behaviors in different directions [255]. In particular, the bone loss phenomenon is connected with the decrease in cancellous and cortical bone of bone density and mineral content. The cancellous bone density in the mandible does not reduce significantly with age. In reality, the cancellous bone density in the basal portion of the mandible tends to increase after tooth loss [265].

The sensitivity of the applied model was tested in response to various mechanical environments, started by developing ideal bone models surrounding a dental implant with different material properties. The remodeling models were simulated using the variation of the initial stiffness of spongious bone by increasing Young's modulus from 100 MPa to 1,000 MPa, keeping that of the cortical bone constant (20 GPa). The modification of Young's modulus of chosen components within the spongious bone area was investigated. With a very low stiffness of the spongious bone of 100 MPa, the highest new bone formation was obtained around the implant and in most areas of spongious bone. However, outside of the cortical bone reached the maximum density, which was color-coded with blue in the figure 3.6. Most probably, this could happen because of overloading. Furthermore, a continuous increase of the stiffness of spongious bone from 350 MPa up to 1,000 MPa caused the more dense bone in the model during the remodeling simulations. That's why cortical and spongious bone reached the maximum density with high Young's modulus. As presented in figure 3.7 and figure 3.8, the highest density was observed in general in spongious bone. That could perhaps be caused by the use of a long bone model. Bone formation was obtained around the implant in these figures.

Various boundary conditions have been used in FE models, e.g., kinematical boundary conditions of 2D triangular element and a quadratic 3D tetrahedral element [253, 254]. A more realistic FE model was developed with masticatory muscles, the ligaments and the movements of temporomandibular joints [266].

During our sensitivity tests, numerous EELs were applied to 2D and 3D models. Different density distributions and density changes were obtained with different EEL, from the small one represented by 0.2 mm and with a large length, which was selected to be 1.0 mm in 2D results. The model with larger EEL was less complex than with the small EEL. Small EEL increased the number of elements in the model, resulting in a more complex model. More dense bone was observed in the area of the cortical and spongious bone with the large EEL. As expected from the previous studies, most of the models had more bone formation when analyzed with a higher EEL. Furthermore, figure 3.35 shows the effect of the EEL of 0.5 mm in 3D model. New bone formation was obtained out of the cortical bone and the inner side of the spongious bone and around the implant.

Further boundary conditions were applied to the 3D models. The fixation situations are the significant effects during the simulations. Different fixations applied to the models are shown in figure 2.18 and figure 2.22. Additionally, a tension face load of 2 MPa was applied on the periphery of the cortical bone on one half, which is known as the buccal side, and compression face load on the other half, which is known as lingual side. Then the muscle loads were applied to the model as compression and tension at the same time to the model.

As explained in the previous paragraph, the fixation is a major effect for all simulations. New fixation conditions were developed in the 3D model to get the ideal conditions for the bone remodeling simulations. Two points were defined far from the model on both sides, and then the model was fixed from these two points with the cortical and spongious bone, as shown in figure 2.25. The influence of this fixation conditions is presented in the figure 3.40. Hence, various muscle loads were applied to the model from 1.0 MPa up to 2.5 MPa as compression and tension to both labial and lingual sides, respectively. The density reached maximum values in the cortical bone and the part of the spongious bone. On the other hand, some new bone formation obtained on some parts around the implant. In addition, bone resorption was observed on the lower left side of the implant in figure 3.40. That could be

perhaps due to the overloading while the cortical bone reached the maximum density.

Osseointegration has been simulated from several researchers using FEA, which show that cortical and spongious bones are ideally bonded to the surface of the implant. This theory matches the clinical conditions. Various boundary conditions at the bone-implant interface were applied in FE simulations, which offer a variety of frictional contact algorithms [259, 267]. FE models to explore the impact of bone loss on mechanical reactions have been created [160–162]. The most popularly used forms of elements in 2D and 3D dental structures are triangular and tetrahedral elements with two and three degrees of freedom at each node, either linear or quadratic. The quadratic forms support more realistic modeling the distribution of strain and stress [268].

In this section, the influence of the total load on the implant was tested on the remodeling model using 3D models with a *tioLogic*$^©$ implant. The distribution of the density increased with the time steps. Cortical bone reached maximum density from the 1. and until 100th iterations. The cortical bone, which was near the neck of the implant, reached the maximum density as well. On the contrary, new bone formation was observed in the area of the spongious bone and around the implant except for the neck of the implant. Increasing a total load of more than 300 N increased the stress too during the simulations. That led to a more dense bone density in the model.

Strain distribution was investigated in this section to show how the total strain changes over the time steps during the remodeling process. Figure 3.25 shows the strain distribution after iterations in 3D models. The maximum equivalent of total strain was observed in the outer part the cortical bone in 25. iteration. The implant had less strain during the simulations. Low strain was observed in all bone and the implant in 100th iterations. From a biomechanical perspective, continuously increasing load leads to deficient strain after specific time steps, see figure 3.25.

Many researchers have studied the effect of muscle loads. The range of the masticatory forces differs over a wide range. In the study by Bozkaya et al., the range of the masticatory forces were between 200 N and 900 N [269]. It was reported that for a complete denture, the occlusal component of the masticatory force is between 75 N and 200 N, and for implant-supported denture is between 40 N and 400 N [270]. Furthermore, the complete range of occlusal forces reported is between 200 N and 3,500 N [271]. Lian and

coworkers investigated bone remodeling in dental implants using 2D FEA. In terms of areas of bone formation and resorption, the overall pattern of density distribution was affected by increased masticatory forces. There is no significant change observed with the total mass of bone tissue [272].

In this study, the influence of the muscle loads were investigated using 2D and 3D FE models. With the small muscle loads more bone resorption was observed on the lower part of the model as well as around the implant, see figure 3.26. New bone formation was obtained by using the muscle loads between 1.5 and 2.5 MPa, see figure 3.27. Density changes can be seen in this figure in the cortical and spongious parts. Besides, cortical bone reached maximum density with 2.5 MPa of muscle force. Bone resorption takes place in the last two and three threads of the implant because of the overloading. The point should be noted that these two simulations were done with remodeling only the spongious bone.

The cortical and spongious bone were remodeled in the next simulation to compare the results with just a remodeled spongious bone. Figure 3.28 shows the results of effect of the muscle force of 1.5 MPa. Bone formation was observed on the left upper side of the model, which contains the cortical and spongious bone. Good connection was obtained between bone and implant on the middle thread of the implant. Bone resorption was observed on the lower part of the model. Bone resorption was highly increased with muscle loads above 4.0 MPa. This explained that the ideal muscle loads should be between 1.5 and 4.0 MPa for the bone remodeling simulations. The difference between compression and tension forces was also simulated. Figure 3.30 and 3.31 present the effect of the compression and tension muscle loads. As it is seen in both figures, new bone formation occurred at some point of the spongious bone when just compression force was applied to the model in both lingual and labial sides; see 3.30. Besides this, bone resorption was obtained in the middle part of the implant surface when the compression and tension forces were applied in labial and lingual sides, respectively. The effect of bending force was also investigated using 3D models. The muscle force was assumed to be 1.5 MPa during these steps. Bone formation was observed around the implant and in the area of spongious bone. With increasing bending loads from 10 to 100 N in Z direction, more dense bone was obtained in the cortical parts, see Figure 3.36 and figure 3.37. The bone resorption occurred in the some point of the middle thread of the implant when bending force was applied to the model in both, Z and Y directions, see figure 3.38 and figure 3.39.

4.3 Comparison to Literature

A computational model was proposed to clarify the bone remodeling processes at a mechanical level [273, 274]. The point to be noted is that despite the importance only relatively few studies exist to predict the reconstruction of the dental bone with the FEM. Only a few studies on this topic can be found [146, 148, 158, 159, 161, 240, 275]. Since there are only few studies in literature involving dental implant induced remodeling, the available dental bone remodeling algorithms are still incomplete. Therefore, additional research and validation in this area required for further advancement [268]. Many researchers have investigated bone remodeling.

In 2007, the use of long-term bone remodeling principles in dental bone remodeling seemed to be a feasible path endorsed by Li and his co-works [146]. In his study, a mathematical model for simulating the dental bone remodeling process under mechanical stimulus was developed, and this algorithm was applied to FEM. A quadratic method was used by Li et al. to account for the overloading effect for dental implant induced bone remodeling. The quadratic curve is shown in figure 1.15, which presents the density change. The dashed line is the traditional change of density rate against the applied SED, while the solid line shows the new density change rate against the applied load. The bone density was slightly improved in the mandible owing to the extra mechanical stimulus given by the occlusal load. These results were observable in also some clinical studies, as reported in the study of Li et al. Bone overload resorption can be explained from the new model. Hence this effect was absent in most of the current models. The capacity of the new mathematical model was proven to simulate bone overload resorption using the FE method. In the results of the study, overload resorption was observed around the neck of the implant, which represents very low density. This finding can sometimes be seen in clinical situations. Clinically, bone loss after implant insertion initially happens quickly, then slows down after a while. Hence, the density of bone increased slightly at the deeper area into the mandible because of the additional mechanical stimulus supplied by the occlusal load. The point to be noted was that all bone elements were given the same material parameters, which might not be realistic, because bone has different types of threshold and critical stresses [146].

Frost developed the mechanostat theory to evaluate the change in bone density by using the biomechanical feedback system. Frost suggested that a minimum effective strain should be in the range of 0.01 % - 0.15 %. That means the bone resorption happens when the strain is equivalent to $100\mu\varepsilon$

or less. Bone will grow when the strain is equivalent to $1,500\mu\varepsilon$ or higher, as shown in figure 1.15 [36, 41]. The realistic bone remodeling process is presented in figure 1.15. Frost proposed that the strain should be between 0.03 % and 0.3 % to initiate bone remodeling. Bone density will decrease when the strain below these values. The equations of mechanostat theory were used in the study of orthodontic tooth movements [34]. In bone remodeling algorithm, the SED has been extensively used as the mechanical stimulus [121, 199]. Later on, SED has been used with the topic of dental implant induced bone remodeling projects [146, 159]. Cheong did another study, using a new bone remodeling algorithm with finite element simulations to model bone ingrowth in 2018. SED was used as the driver for remodeling in the FEA models. There was an inverse ratio between implant material and bone ingrowth, reducing implant material stiffness increases bone ingrowth. Using lower elastic modulus could promote increased bone remodeling [276].

Hasan and colleagues investigated the computational simulation of internal bone remodeling around dental implants based on applying a selected mathematical remodeling model. Sensitivity analysis was done in response to different mechanical environments, i.e., EEL, different boundary conditions, and loads. High density was obtained with small EEL within the cancellous bone, whereas a minimal change in density occurred with large EEL. More stable density distributions around the outer regions of cortical bone were received with the higher load applied on the cortical. In the vertical axis force range a from 250 to 300 N, a stable behavior of the cortical bone density was achieved. Within a short time, the significant change in bone density was obtained with the enormous magnitude of the lateral force combined with a sudden increase in the bone stresses [157].

Local stress and strain in a fracture gap were studied with three healing stages using FEM and than compared with an animal fracture model. Low strains were observed in the first healing stage in all areas along the periosteal and endosteal surface. Besides, large strains were found in the area of cortical gap and around the cortical edges. High strains were observed in comparison in longitudinal direction at the center of the remaining periosteal surface. Only with the low strains and low hydrostatic pressure, intramembranous bone formation occurred. A mechanical environment is required for an intramembranous bone formation by osteoid apposition from osteoblasts. The FE studies are mandatory to simulate the generality of new tissue differentiation theory further [277]. The point to note was that there are some limitations on an investigation based on a FEM. Material properties, loading conditions or geometry are important parameters for a quality of the FE

analysis [278].

A study investigated the biomechanical response of peri-implant bone in rabbits and the results were compared with FE models in 2014. The authors found that bone formation occurred with 2.0 MPa stress, bone resorption with higher then 4.0 MPa stresses [279]. Korabi and coworkers applied a new theory (the failure envelope concept) to dental implants. As reported by Korabi, more bone will be achieved when the implant is osseointegrated. Nonetheless, the failure envelope will be increased, and bone resorption will be increased if the bone implant contact is reduced, and the lateral load levels are dominant [275]. Irandoust and Muftu investigated bone remodeling around early loaded dental implant systems using 2D models to understand long-term osseointegration. There was no linear correlation between the mechanical load and the evaluation of tissue type around dental implants. However, to explain the long-term adaptation of internal bone density and potential regions of bone resorption, only the tissue-healing phase is not enough to get information [280]. Lin and coworkers presented that the cancellous bone reaches the steady-state of bone remodeling at an earlier stage than the cortical bone. The ratio of bone remodeling can be improved with the influence of the osseointegration [281]. The stress decreased with increasing layer thickness when the stress transferred more uniformly in the dental implants with nanoporous structures [282]. Kurniawan and coworkers have been worked with osseointegrated dental implants. They reported that the highest stress observed in the crustal area of the cortical bone. Lower strain and higher stress obtained with a higher degree of osseointegration. According to the study, solid and more osseointegrated peri-implant bone is desirable for minimum strain and stress [283]. The overload resorption observed only in the case of low initial density [244].

The long-term success of implant treatment is influenced by the mechanical conditions applied to the implant during osseointegration. The present study describes a progressive healing process by iteratively changing the element material properties. Histologically, osseointegration consists of three phases of different tissue states and thus three different osseointegration phases with three different thicknesses were developed to simulate the healing process using 2D models. Phase 1 represents the process immediately after implant insertion to two weeks: Haematoma, connective tissue (CT). Phase 2 is the situation after two months: Intermediate stiffness callus (MSC), Soft callus (SOC), Connective tissue (CT). Phase 3 is after four months: Stiff callus (SC), Intermediate stiffness callus (MSC), Soft callus (SOC). These three phases were developed with different thicknesses of 0.1, 0.2, and 0.3

114

mm to investigate the influence of the thickness of osseointegration layer during the remodeling process. Different EELs were simulated during the simulations. A compressive pressure of 2.0 MPa on the labial and lingual side was used to simulate functional loading like muscle pressure. To get a stable initial bone distribution, bone remodeling was performed for the whole bone and the connective layer using the classical remodeling. Figure 3.10 represents the density distribution of phase 2 with different thickness of tissue layers. Positive remodeling and increased density were obtained in part of the spongious bone and, in particular, around the implant. Increasing the thickness of tissue layers increased the density changes too. Phase 1 and phase 3 could not achieve good bone formation around the implant. That could be explained in phase 1 has soft material. Phase 3 was too dense for these boundary conditions.

As the next steps, in the region of the trabecular bone, a grid represented the spongious structure in the 2D model. Two scenarios were used in this section;

1- Simulations without osseointegration

This scenario was used without tissue layers between bone and implant interface using different forces, EEL, Young's modulus of bone and muscle loads to get a stable initial bone distribution. The effect of two different young's moduli of spongious bone is shown in figure 3.15. Good connection was achieved between implant and bone by using low Young's modulus of spongious bone. Bone resorption was observed in the lower part of the implant with high young's modulus of spongious bone.

2- Simulations with osseointegration

As second scenario, the tissue types were added between implant and bone to simulate the osseointegration. All three healing phases were used as previous sections. In this scenario, different EEL, young's modulus of spongious, muscle loads, and total forces were used to see the influence of different boundary conditions on osseointegration. Figures 3.16, 3.17, and 3.18 represent the density distribution of phase 1, phase 2, and phase 3, respectively. The EEL was 0.5 mm in these figures. Figure 3.16 shows that the bone resorption occurred in all thicknesses around the implant. Increasing the thickness also increased bone resorption around the implant. On the other side, figure 3.17 is representing a positive remodeling, and the best density changes almost in all thicknesses. More dense density obtained with phase 3 around the implant of thickness 0.2 and 0.3 mm ,see figure 3.18.

As a next step, EEL was set to 0.2 mm. Figure 3.19 shows density distribution of phase 1. Osseointegration was observed just with 0.1 mm, and this result corresponds to clinical observations. Bone resorption was observed around the implant with 0.3 mm. Besides, bone formation obtained with all thicknesses in 3.20. Bone resorption obtained in part of the spongious bone of the left side of the implant. The reason for this could be that the total forces were applied to the model from the right side. In the figure 3.21, a favorable bone formation occurred with 0.1 and 0.3 mm. The density reached the maximum on the right side of the implant with 0.2 mm. Additionally, bone formation obtained around the neck of the implant in phase 2 and phase 3 with EEL, see 3.20, and 3.21.

4.4   Future Perspectives

The analyses of the 2D and 3D FE models were performed under different mechanical conditions and bone remodeling parameters for the bone remodeling around dental implants. Also, osseointegration phases were simulated using 2D FE models under various loading conditions and different bone remodeling parameters using bone remodeling theories around the dental implant. The bone remodeling algorithm could be successfully applied to the 2D model as well as to the 3D model. However, due to the limitations of the idealized model geometry in the 2D model, it was not possible to obtain an anatomically correct structure consisting of an outer cortical layer and an inner trabecular structure. Similar boundary conditions can be applied in future 3D modeling to investigate the different osseointegration phases around the different dental implants.

References

[1] Marlene Mengoni. *On the development of an integrated bone remodeling law for orthodontic tooth movements models using the Finite Element Method.* PhD thesis, University of Liege, 2012.

[2] H. Gray. Anatomy of the human body. *Lea and Fiebiger, Philadelphia,* 1918.

[3] A. Vanheudsen. Anatomie de l'appareil masticateur, cours de 2ème bachelier sciences dentaires. *Universitéde Liege,* 2008.

[4] F.C. Mclean and M.R. Urist. Bone. *Chicago, Univ. Chicago,* 1968.

[5] S.C. Cowin. Bone Mechanics Handbook. *CRC Press LLC,* Second Edition, 2001.

[6] S.C. Cowin and D.H. Hegedus. Bone remodeling I: theory of adaptive elasticity. *Journal of Elasticity,* 6:313–326, 1976.

[7] L.J. Schutte. An Agent-based Model for Evaluating Cellular Mechanisms of Bone Remodeling. *Thesis, Carnegie Mellon University Pittsburgh, PA,* 2012.

[8] Peter J Bishop, Scott A Hocknull, Christofer J Clemente, John R Hutchinson, Andrew A Farke, Belinda R Beck, Rod S Barrett, and David G Lloyd. Cancellous bone and theropod dinosaur locomotion. part i-an examination of cancellous bone architecture in the hindlimb bones of theropods. *PeerJ.,* 6:e5778, 2018.

[9] Andrew J. Burghardt, Thomas M. Link, and Sharmila Majumdar. High-resolution computed tomography for clinical imaging of bone microarchitecture. *Clinical Orthopaedics and Related Research,* 469:2179–2193, 2011.

[10] Jessica Marie O'Neal. The effects of aging and remodeling on bone quality and microdamage. *Georgia Institute of Technology,* 2011.

[11] Roger Zebaze and Ego Seeman. Cortical bone: A challenging geography. *Journal of Bone and Mineral Research,* 30:24–29, 2015.

[12] H.M. Frost. Bone remodelling dynamics. *Springfield, IL: Charles C. Thomas,* 1963.

[13] J. Wolff. Das gesetz der transformation der knochen. *Hirschwald Verlag, Berlin*, 1892.

[14] G.S. Beaupre, T.E. Orr, and D.R. Carter. An approach for time-dependent bone modeling and remodeling—theoretical development. *Journal of Orthopaedic Research*, 8:651–661, 1990a.

[15] D.R. Carter. Mechanical loading history and skeletal biology. *Journal of Biomechanics*, 20:1095–1109, 1987.

[16] Stephen C. Cowin and Keykhosrow Firoozbakhsh. Bone remodeling of diaphysial surfaces under constant load: Theoretical predictions. *Journal of Biomechanics*, 14:471 – 484, 1981.

[17] Naval Architecture and Jasna Leder Horina. Modelling of Initiation of Bone Remodelling due to Orthodontic Treatment Modelling of Initiation of Bone Remodelling due to Orthodontic Treatment. *PhD thesis, University of Zagreb*, 2015.

[18] H M Frost. Skeletal Structural Adaptations to Mechanical Usage (SATMU): 1 . Redefining Wolff ' s Law : The Bone Modeling Problem. *The Anatomical Record*, 413:403–413, 1990a.

[19] A.M. Parfitt. Quantum concept of bone remodeling and turnover: implications for the pathogenesis of osteoporosis. *Calcified Tissue International*, 28:1 – 5, 1979.

[20] H.M. Frost. The law of bone structure. *Charles C. Thomas, Springfield*, 1964.

[21] J.H. Dimitrios and I.I. Androulakis. Bone remodeling. *Annals of the New York Academy of Sciences*, 1092:385–396, 2006.

[22] Nick Little, Benedict Rogers, and Mark Flannery. Bone formation, remodelling and healing. *Surgery (Oxford)*, 29:141 – 145, 2011.

[23] A. M. Parfitt. The mechanism of coupling: a role for the vasculature. *Bone*, 26:319–323, 2000.

[24] E. F. Eriksen, L. Mosekilde, and F. Melsen. Effect of sodium fluoride, calcium, phosphate, and vitamin D2 on trabecular bone balance and remodeling in osteoporotics. *Bone*, 6:381–389, 1985.

[25] A.M. Parfitt. The physiologic and clinical significance of bone histomorphomstric data. in bone histomorphometry: Techniques and interpretations, ed. rr recker. *Boca Raton, FL: CRC Press*, pages 143 – 244, 1983.

[26] Alexander G. Robling, Alesha B. Castillo, and Charles H. Turner. Biomechanical and Molecular Regulation of Bone Remodeling. *Annual Review of Biomedical Engineering*, 8:455–498, 2006.

[27] E.R. Weibel. Stereological methods, vol. 2: Theoretical foundations. *Academic Press, New York*, 1980.

[28] A.E. Goodship, L.E. Lanyon, and H. McFie. Functional adaptation of bone to increased stress. an experimental study. *The Journal of Bone and Joint Surgery*, 61:539–546, 1979.

[29] I. A F Stokes. Mechanical effects on skeletal growth. *Journal of Musculoskeletal Neuronal Interactions*, 2:277–280, 2002.

[30] Dennis R Carter, Gary S Beaupre, Nickolas J. Giori, and Jill A. Helms. Mechanobiology of skeletal regeneration. *Clinical orthopaedics and related research*, 1998.

[31] D. Thompson. On growth and form. *Journal of Orthod*, 53:881 – 903, 1952.

[32] C. Andrew L. Bassett. Biologic significance of piezoelectricity. *Calcified Tissue Research*, 1:252–272, 1968.

[33] C.A.L. Bassett. Biophysical principles affecting bone structure. *In the Biochemistry and Physiology of Bone, 2nd ed., vol. III (ed. G. H. Bourne) London: Academic Press.*, pages 1 – 77, 1971.

[34] H M Frost. Bone " Mass " and the " Mechanostat ": A Proposal. *The Anatomical Record*, 219:1 – 9, 1987a.

[35] H.M. Frost. The mechanostat: a proposed pathogenic mechanism of osteoporoses and the bone mass effects of mechanical and nonmechanical agents. *Journal of Bone and Mineral Research*, 2:73 – 85, 1987b.

[36] Harold M. Frost. Bone's Mechanostat: A 2003 Update. *Anatomical Record - Part A Discoveries in Molecular, Cellular, and Evolutionary Biology*, 275:1081–1101, 2003.

[37] S.C. Cowin. Wolff's law of trabecular architecture at remodeling equilibrium. *Journal of Biomechanical Engineering*, 108:83 – 88, 1986.

[38] John Currey. The Mechanical adaptations of Bones. *Princeton University Press*, pages 141–142, 1984.

[39] C.T. Rubin. Skeletal strain and the functional significance of bone architecture. *Calcified Tissue International [Suppl.]*, 36:11 – 18, 1984.

[40] W.S. Jee and H.M. Frost. Skeletal adaptations during growth. *Triangle*, 31:77–88, 1992.

[41] H.M. Frost. The regional acceleratory phenomenon: a review. *Henry Ford Hosp Med J.*, 31:3 – 9, 1983.

[42] H.F. DeLuca, H.M. Frost, W.S.S. Jee, Jr. C.C. Johnston, and A.M. Parfitt. Osteoporosis. recent advances in pathogenesis and treatment. *University Park Press, Baltimore*, 1981.

[43] B. Frame and Jr. J.T. Potts. Clinical disorders of bone and mineral metabolism. *Excerpta Medica, Oxford*, 1983.

[44] R.P. Heaney, R.R. Recker, and P.D. Saville. Menopausal changes in bone remodeling. *Journal Lab. Clin. Med.*, 92:964–970, 1978.

[45] L.E. Lanyon. Functional strain as a determinant for bone remodeling. *Calcified Tissue International [Supl.]*, 36:56–61, 1984.

[46] P. Lips. Metabolic causes and prevention of femoral neck fractures. *PhD Thesis. University of Amsterdam*, 1982.

[47] P. Minnaire. L'osteoporose d'immobilization. donnbes biologiques et histologiques quantitatives. *PhD Thesis. Ediprim, Lyon*, 1973.

[48] H. Uhthoff. Current concepts of bone fragility. *Springer-Verlag, Berlin*, 1986.

[49] R.R. Recker. Bone histomorphometry. techniques and interpretation. *C.R.C. Press, Boca Raton*, 1983.

[50] E.L. Smith, P.E. Smith, C.J. Ensign, and M.M. Shea. Bone involution decrease in exercising middle-aged women. *Calcif. Tissue Int. [Suppl.]*, 36:129 – 138, 1984.

[51] G.D. Whedon. Disuse osteoporosis: Physiological aspects. *Calcified Tissue International [Suppl.]*, 36:146 – 150, 1984.

120

[52] T.J. Wronski and E.R. Morev. Skeletal abnormalities in rats induced by simulated weightlessness. *Metabolic Bone Disease and Related Research*, 4:69 – 76, 1982.

[53] T.J. Wronski and E.R. Morev. Inhibition of cortical and trabecular bone formation in the long bones of immobilized monkeys. *Clinical Orthopaedics and related research*, 181:269– 276, 1983a.

[54] T.J. Wronski and E.R. Morev. Effect of spaceflight on periosteal bone formation in rats. *American Journal of Physiology.*, 13:305– 309, 1983b.

[55] T.J. Wronski, C.C. Walsh, and L.A. Ignaszewski. Histologic evidence for osteopenia and increased bone turnover in ovariectomized rats. *Bone*, 7:119 – 124, 1986.

[56] D.R. Young, W.J. Niklowitz, R.J. Brown, and W.S.S. Jee. Immobilization-associated osteoporosis in primates. *Bone*, 7:109 – 118, 1986.

[57] H. M. Frost. Vital biomechanics: Proposed general concepts for skeletal adaptations to mechanical usage. *Calcified Tissue International*, 42:145–156, May 1987c.

[58] D.M. Raab-Cullen, M.P. Akhter, D.B. Kimmel, and R.R. Recker. Periosteal bone formation stimulated by externally induced bending strains. *Journal of Bone and Mineral Research*, 9:1143–1152, 8 1994.

[59] C.H. Turner, M.R. Forwood, J.Y. Rho, and T. Yoshikawa. Mechanical loading thresholds for lamellar and woven bone formation. *Journal of Bone and Mineral Research*, 9:87–97, 1994.

[60] Clinton Rubin, A Simon Turner, Steven Bain, Craig Mallinckrodt, and Kenneth Mcleod. Low mechanical signals strengthen long bones. *Nature*, 412, 2001.

[61] Mark R Forwood, L I Li, Wendy L Kelly, and Michael B Bennett. Mechanical Loading. *Journal of Bone and Mineral Research*, 16:2284– 2290, 2001.

[62] Sundar Srinivasan, David A. Weimer, Steven C. Agans, Steven D. Bain, and Ted S. Gross. Low-magnitude mechanical loading becomes osteogenic when rest is inserted between each load cycle. *Journal of Bone and Mineral Research*, 17:1613–1620, 2002.

[63] Karla Lee, Helen Jessop, Rosemary Suswillo, Gul Zaman, Lance Lanyon, Mary P Ryan, and David E Williams. Bone adaptation requires oestrogen receptor $-\alpha$. *Nature*, 424:389–390, 2003.

[64] Roberto L. De Souza, Maiko Matsuura, Felix Eckstein, Simon C.F. Rawlinson, Lance E. Lanyon, and Andrew A. Pitsillides. Non-invasive axial loading of mouse tibiae increases cortical bone formation and modifies trabecular organization: A new model to study cortical and cancellous compartments in a single loaded element. *Bone*, 37:810 – 818, 2005a.

[65] H. Hagino, M. Kuraoka, Y. Kameyama, T. Okano, and R. Teshima. Effect of a selective agonist for prostaglandin E receptor subtype EP4 (ONO-4819) on the cortical bone response to mechanical loading. *Bone*, 36:444–453, 2005.

[66] King-Hing William Lau, Sonia Kapur, Chandrasekhar Kesavan, and David J. Baylink. Up-regulation of the Wnt, Estrogen Receptor, Insulin-like Growth Factor-I, and Bone Morphogenetic Protein Pathways in C57BL/6J Osteoblasts as Opposed to C3H/HeJ Osteoblasts in Part Contributes to the Differential Anabolic Response to Fluid Shear. *The journal of biological chemistry*, 281:9576 – 9588, 2006.

[67] John A. Robinson, Moitreyee Chatterjee-Kishore, Paul J. Yaworsky, Diane M. Cullen, Weiguang Zhao, Christine Li, Yogendra Kharode, Linda Sauter, Philip Babij, Eugene L. Brown, Andrew A. Hill, Mohammed P. Akhter, Mark L. Johnson, Robert R. Recker, Barry S. Komm, and Frederick J. Bex. Wnt/β-catenin signaling is a normal physiological response to mechanical loading in bone. *Journal of Biological Chemistry*, 281:31720–31728, 2006.

[68] A.G. Torrance, J.R. Mosley, F.R. Suswillo, and L.E. Lanyon. Noninvasive loading of the rat ulna in vivo induces a strain-related modeling response uncomplicated by trauma or periostal pressure. *Calcified Tissue International*, 54:241 – 247, 1994.

[69] M P Akhter, D M Cullen, E A Pedersen, D B Kimmel, and R R Recker. Orthopedic Surgical Forum Bone Response to In Vivo Mechanical Loading in Two Breeds of Mice. *New York*, 63:442–449, 1998.

[70] K. C.L. Lee, A. Maxwell, and L. E. Lanyon. Validation of a technique for studying functional adaptation of the mouse ulna in response to mechanical loading. *Bone*, 31:407–412, 2002.

[71] Ted S Gross, Sundar Srinivasan, Chung C Liu, Thomas L Clemens, and Steven D Bain. Noninvasive loading of the murine tibia: an in vivo model for the study of mechanotransduction. *Journal of Bone and Mineral Research*, 17:493–501, 2002.

[72] Roberto L. De Souza, Andrew A. Pitsillides, Lance E. Lanyon, Timothy M. Skerry, and Chantal Chenu. Sympathetic nervous system does not mediate the load-induced cortical new bone formation. *Journal of Bone and Mineral Research*, 20:2159–2168, 2005b.

[73] J. C. Fritton, E. R. Myers, T. M. Wright, and M. C H Van Der Meulen. Loading induces site-specific increases in mineral content assessed by microcomputed tomography of the mouse tibia. *Bone*, 36:1030–1038, 2005.

[74] Ping Zhang, Shigeo M Tanaka, Hui Jiang, Min Su, and Hiroki Yokota. Diaphyseal bone formation in murine tibiae in response to knee loading. *Journal of Applied Physiology*, 100:1452–1459, 2006.

[75] Massimo Marenzana, Roberto L. De Souza, and Chantal Chenu. Blockade of beta-adrenergic signaling does not influence the bone mechano-adaptive response in mice. *Bone*, 41:206–215, 2007.

[76] J. Christopher Fritton, Elizabeth R. Myers, Timothy M. Wright, and Marjolein C.H. Van Der Meulen. Bone mass is preserved and cancellous architecture altered due to cyclic loading of the mouse tibia after orchidectomy. *Journal of Bone and Mineral Research*, 23:663–671, 2008.

[77] Toshihiro Sugiyama, Leanne K. Saxon, Gul Zaman, Alaa Moustafa, Andrew Sunters, Joanna S. Price, and Lance E. Lanyon. Mechanical loading enhances the anabolic effects of intermittent parathyroid hormone (1-34) on trabecular and cortical bone in mice. *Bone*, 43:238–248, 2008.

[78] M.J. Perry, L.K. Parry, V.J. Burton, S. Gheduzzi, J.N. Beresford, V.F. Humphrey, and T.M. Skerry. Ultrasound mimics the effect of mechanical loading on bone formation in vivo on rat ulnae. *Medical Engineering and Physics*, 31:42 – 47, 2009.

[79] Alaa Moustafa, Toshihiro Sugiyama, Leanne K. Saxon, Gul Zaman, Andrew Sunters, Victoria J. Armstrong, Behzad Javaheri, Lance E. Lanyon, and Joanna S. Price. The mouse fibula as a suitable bone for the study of functional adaptation to mechanical loading. *Bone*, 44:930–935, 2009.

[80] A. I. Pearce, R. G. Richards, S. Milz, E. Schneider, and S. G. Pearce. Animal models for implant biomaterial research in bone: A review. *European Cells and Materials*, 13:1–10, 2007.

[81] Susannah J. Sample, Mary Behan, Lesley Smith, William E. Oldenhoff, Mark D. Markel, Vicki L. Kalscheur, Zhengling Hao, Vjekoslav Miletic, and Peter Muir. Functional adaptation to loading of a single bone is neuronally regulated and involves multiple bones. *Journal of Bone and Mineral Research*, 23:1372–1381, 2008.

[82] J. Hert, M. Liskova, and B. Landrgot. Influence of the long-term continuous bending on the bone. *Folia Morphol*, 17:389–399, 1969.

[83] J. Hert, M. Liskova, and M. Landa. Reaction of bone to mechanical stimuli. part i. continuous and intermittent loading of tibia in rabbit. *Folia Morphol*, 19:290–300, 1971.

[84] M. Liskova and J. Hert. Reaction of bone to mechanical stimuli. part ii. periosteal and endosteal reaction of tibial diaphysis in rabbit to intermittent loading. *Folia Morphol*, 19:301 – 317, 1971.

[85] A. E. Churches, C. R. Howlett, K. J. Waldron, and G. W. Ward. The response of living bone to controlled time-varying loading: Method and preliminary results. *Journal of Biomechanics*, 12:35–45, 1979.

[86] J.A. OConnor, L.E. Lanyon, and H. MacFie. The influence of strain rate on adaptive bone remodelling. *Journal of Biomechanics*, 15:767 – 781, 1982.

[87] C.T. Rubin and L.E. Lanyon. Bone remodelling in response to applied dynamic loads. *Orthop Trans*, 5:2 – 37, 1981.

[88] C.T. Rubin and L.E. Lanyon. Regulation of bone formation by applied dynamic loads. *Journal of Bone and Joint Surgery*, 66:397 – 402, 1984.

[89] Clinton T Rubin and Lance E Lanyon. Regulation of Bone Mass by Mechanical Strain Magnitude. *Calcified Tissue International*, pages 411–417, 1985.

[90] Clinton T Rubin and Lance E Lanyon. Osteoregulatory Nature. *Journal of Orthopaedics Research*, pages 300–310, 1987.

[91] Toshihiro Sugiyama, Joanna S. Price, and Lance E. Lanyon. Functional adaptation to mechanical loading in both cortical and cancellous bone

is controlled locally and is confined to the loaded bones. *Bone*, 46:314–321, 2010.

[92] Floor M. Lambers, Friederike A. Schulte, Gisela Kuhn, Duncan J. Webster, and Ralph Müller. Mouse tail vertebrae adapt to cyclic mechanical loading by increasing bone formation rate and decreasing bone resorption rate as shown by time-lapsed in vivo imaging of dynamic bone morphometry. *Bone*, 49:1340–1350, 2011.

[93] H. Maeda, D. B. Kimmel, D. M. Raab, and N. E. Lane. Musculoskeletal recovery following hindlimb immobilization in adult female rats. *Bone*, 14:153–159, 1993.

[94] S. Bourrin, S. Palle, R. Vico, and C. Alexandre. Effects of physical-training on bone adaptation in 3 zones of the rat tibia. *Journal of Bone and Mineral Research*, 10:1745 – 1752, 1995.

[95] A.J. Kaneps, S.M. Stover, and N.E. Lane. . changes in canine cortical and cancellous bone mechanical properties following immobilization and remobilization with exercise. *Bone*, 21:419–423, 1997.

[96] A. Kiuchi, Y. Arai, and S. Katsuta. Detraining effects on bone mass in young male rats. *International Journal of Sports Medicine*, 19:245–249, 1998.

[97] Laurence Vico, M. H. Lafage, and Christian Alexandre. Effects of gravitational changes on the bone system in vivo and in vitro. *European Space Agency, (Special Publication) ESA SP*, 22:107–114, 1998.

[98] R.T. Hart, D.T. Davy, and K.G. Heiple. A predictive model for strain-induced remodelling in long bones. transactions of the 1983. *Orthop Res Society*, 71, 1983.

[99] C.R. Hassler, E.F. Rybicki, K.D. Cummings, and L.C. Clark. Quantification of bone stresses during remodelling. *Journal of Biomechanics*, 13:185–190, 1980.

[100] J.B. Meade, S.C. Cowin, J.J. Klawitter, H.B. Skinner, and W.C. Buskirk. Short term modelling due to hyperphysiological stress. *Transactions of the 1983. Orthop Res Society*, 62, 1981.

[101] Alireza Rahimi, Reinhard Klein, Ludger Keilig, Marcus Abboud, Gerhard Wahl, and Christoph Bourauel. Development and design of a novel

loading device for the investigation of bone adaptation around immediately loaded dental implants using the reindeer antler as implant bed. *Journal of Biomechanics*, 42:2415–2418, 2009.

[102] Annette I. Birkhold, Hajar Razi, Georg N. Duda, Richard Weinkamer, Sara Checa, and Bettina M. Willie. Mineralizing surface is the main target of mechanical stimulation independent of age: 3D dynamic in vivo morphometry. *Bone*, 66:15–25, 2014.

[103] Toru Ogawa, Xiaolei Zhang, Ignace Naert, Peter Vermaelen, Christophe M. Deroose, Keiichi Sasaki, and Joke Duyck. The effect of whole-body vibration on peri-implant bone healing in rats. *Clinical Oral Implants Research*, 22:302–307, 2011.

[104] Friederike A. Schulte, Davide Ruffoni, Floor M. Lambers, David Christen, Duncan J. Webster, Gisela Kuhn, and Ralph Müller. Local Mechanical Stimuli Regulate Bone Formation and Resorption in Mice at the Tissue Level. *PLoS ONE*, 8, 2013.

[105] Patrik Christen, Keita Ito, Rafaa Ellouz, Stephanie Boutroy, Elisabeth Sornay-Rendu, Roland D. Chapurlat, and Bert Van Rietbergen. Bone remodelling in humans is load-driven but not lazy. *Nature Communications*, 5:1–5, 2014.

[106] Shailly H Jariwala, Hwabok Wee, Evan P Roush, Tiffany L Whitcomb, Gery Kozlansky, Akhlesh Lakhtakia, Allen R Kunselman, Henry J Donahue, April D Armstrong, and Gregory S Lewis. Time course of peri-implant bone regeneration around loaded and unloaded implants in a rat model. *Journal of Orthopaedic Research*, 35:997–1006, 2017.

[107] Zihui Li, Ralph Müller, and Davide Ruffoni. Bone remodeling and mechanobiology around implants: Insights from small animal imaging. *Journal of Orthopaedic Research*, 36:584–593, 2017.

[108] Yun He, Dominik Fischer, Istabrak Hasan, Werner Götz, Ludger Keilig, Luisa Ziegler, Markus Abboud, Christoph Bourauel, and Gerhard Wahl. Sika deer antler as a novel model to investigate dental implant healing: A pilot experimental study. *PLoS ONE*, 13:1–12, 2018.

[109] G.S. Beaupre, T.E. Orr, and D.R. Carter. An Approach for Time-Dependent Bone Modeling and Remodeling-Application: A Preliminary Remodeling Simulation. *Journal of Orthopaedic Research*, 8:662–670, 1990b.

[110] A. Gjelsvik. Bone Remodeling and Piezoelectircity-I. *Journal of Biomechanics*, 6:69–77, 1973.

[111] R.T. Hart and D.T. Davy. Theories of bone modeling and remodeling, in bone mechanics (ed. s. c. cowin). *CRC Press, Boca Raton, FL*, pages 253–277, 1989.

[112] H.W.J. Huiskes, H. Weinans, H.J. Grootenboer, M. Dalstra, B. Fudala, and T.J.J.H. Slooff. Adaptive bone-remodeling theory applied to prosthetic- design analysis. *Journal of Biomechanics*, 20:1135 – 1150, 1987.

[113] Christopher R. Jacobs, Juan C. Sirno, Gary S. Beaupre, and Dennis R. Carter. Adaptive bone remodeling incorporating simultaneous density and anisotropy considerations. *Journal of Biomechanics*, 30:603 – 611, 1996.

[114] B.K. Kummer. Biomechanics of bone. *Prentice-Hall, Englewood Cliffs*, 1972.

[115] S.C. Cowin, A.M. Sadegh, and G.M. Luo. An evolutionary wolff's law for trabecular architecture. *Journal of Biomechanical Engineering*, 114:129 – 136, 1992.

[116] D.M. Hegedus and S.C. Cowin. Bone remodeling ii: Small strain adaptive elasticity. *Journal of Elasticity*, 6:337–352, 1976.

[117] J. Wolff. The law of bone remodeling (original publication 1892 translated in 1986 by p. maquet and r. furlong). *Springer, Berlin*, 1982.

[118] D. R. Carter, D. P. Fyhrie, and R. T. Whalen. Trabecular bone density and loading history: Regulation of connective tissue biology by mechanical energy. *Journal of Biomechanics*, 20, 1987.

[119] D. R. Carter, T. E. Orr, and D. P. Fyhrie. Relationships Between Femoral Loading History and. *Journal of biomechanics*, 22:231–244, 1989.

[120] B. Mikic and D.R. Carter. Bone strain gage data and theoretical models of functional adaptation. *Journal of Biomechanics*, 28:465 – 469, 1995.

[121] H Weinans, R Huiskes, and H.J. Grootenboer. The Behavior of Adaptive Bone-Remodeling Simulation Models . *Journal of Biomechanics*, 25:1425–1441, 1992.

[122] J Kerner, R Huiskes, G H Van Lenthe, H Weinans, B Van Rietbergen, C A Engh, and A A Amis. Correlation between pre-operative periprosthetic bone density and post-operative bone loss in THA can be explained by strain-adaptive remodelling. *Journal of Biomechanics*, 32:695 – 703, 1999.

[123] M.G. Mullender, R. Huiskes, and H. Weinans. A physiological approach to the simulation of bone remodeling as a self-organizational control process. *Journal of Biomechanics*, 27:1389–1394, 1994.

[124] R.T. Hart, D.T. Davy, and K.G. Heiple. Mathematical modelling and numerical solutions for functionally dependent bone remodelling. *Calcif Tissue Int*, 36:104–109, 1984a.

[125] B. Van Rietbergen, R. Huiskes, H. Weinans, D. R. Sumner, T. M. Turner, and J. O. Galante. The mechanism of bone remodeling and resorption around press-fitted THA stems. *Journal of Biomechanics*, 26:369–382, 1993.

[126] M G Mullender and R Huiskes. Proposal for the Regulatory Mechanism of Wolff ' s Law. *Journal of Orthopaedics Research*, 1995.

[127] M. G. Mullender and R. Huiskes. Osteocytes and bone lining cells: Which are the best candidates for mechano-sensors in cancellous bone? *Bone*, 20:527–532, 1997.

[128] M. Mullender, B. Van Rietbergen, P. Rüegsegger, and R. Huiskes. Effect of mechanical set point of bone cells on mechanical control of trabecular bone architecture. *Bone*, 22:125–131, 1998.

[129] H M Frost. Skeletal Structural Adaptations to Mechanical Usage (SATMU): 2 . Redefining Wolff ' s Law : The Remodeling Problem. *The Anatomical Record*, 422:414–422, 1990b.

[130] Laoise M. Mcnamara and Patrick J. Prendergast. Perforation of cancellous bone trabeculae by damage-stimulated remodelling at resorption pits: A computational analysis. *European Journal of Morphology*, 42:99 – 109, 2005.

[131] Mette Bagge. A model of bone adaptation as an optimization process. *Journal of Biomechanics*, 33:1349–1357, 2000.

[132] M. Doblaré and J. M. García. Application of an anisotropic bone-remodelling model based on a damage-repair theory to the analysis of

the proximal femur before and after total hip replacement. *Journal of Biomechanics*, 34:1157–1170, 2001.

[133] Rik Huiskes, Ronald Ruimerman, and G. Harry van Lenthe. Effects ofmechanical forces onmaintenance and adaptation of form in trabecular bone. *Nature*, 405, 2000.

[134] R. Ruimerman, R. Huiskes, G. H. Van Lenthe, and J. D. Janssen. A computer-simulation model relating bone-cell metabolism to mechanical adaptation of trabecular architecture. *Computer Methods in Biomechanics and Biomedical Engineering*, 4:433–448, 2001.

[135] R Ruimerman. Modeling and Remodeling in Bone Tissue. *Thesis, Technische Universiteit Eindhoven*, 2005.

[136] J. Martínez-Reina, J. M. García-Aznar, J. Domínguez, and M. Doblaré. A bone remodelling model including the directional activity of BMUs. *Biomechanics and Modeling in Mechanobiology*, 8:111–127, 2009.

[137] Diogo Geraldes. Orthotropic modelling of the skeletal system. *Thesis, Imperial College of Science, Technology and Medicine*, 2012.

[138] Shitong Lou, Xingquan Shen, Xin Bai, Jing Bai, Jianning Han, and Yu Shang. Validation of material algorithms for femur remodelling using medical image data. *Hindawi Applied Bionics and Biomechanics*, pages 24–29, 2017.

[139] P. Shang, J. Zhang, and A. R. Qian. Bone cells under microgravity. *Journal of Mechanics in Medicine and Biology*, 13, 2013.

[140] H. Gong, L.Y. Kong, R. Zhang, J. Fang, and M.S. Zhao. A femur-implant model for the prediction of bone remodeling behavior induced by cementless stem. *Journal of Bionic Engineering*, 10:350–358, 2013.

[141] Xinghua Zhu, He Gong, Dong Zhu, and Bingzhao Gao. A study of the effect of non-linearities in the equation of bone remodeling. *Journal of Biomechanics*, 35:951–960, 2002.

[142] Zev Miller, Moshe B. Fuchs, and Mircea Arcan. Trabecular bone adaptation with an orthotropic material model. *Journal of Biomechanics*, 35:247–256, 2002.

[143] Y. Shang, J. Bai, L. Peng, and J. Lau. Comparison of methods for determining orthotropic axes in 3d femur remodeling. *Progress in Natural Science*, 17:1405 – 1411, 2007.

[144] Juan Fang, He Gong, Lingyan Kong, and Dong Zhu. Simulation on the internal structure of three-dimensional proximal tibia under different mechanical environments. *BioMedical Engineering Online*, 12:1–17, 2013.

[145] W. R. Taylor, H. Ploeg, D. Hertig, M. D. Warner, and S. E. Clift. Bone remodelling of a proximal femur with the thrust plate prosthesis: An in vitro case. *Computer Methods in Biomechanics and Biomedical Engineering*, 7:131–137, 2004a.

[146] Jianying Li, Haiyan Li, Li Shi, Alex S L Fok, Cemal Ucer, Hugh Devlin, Keith Horner, and Nick Silikas. A mathematical model for simulating the bone remodeling process under mechanical stimulus. *Dental Material*, 3:1073–1078, 2007.

[147] J. Vander Sloten, H. van Oosterwyck, S.V.N. Jaecques, J. Duyck, and I. Naert. Adaptive bone remodelling: bone as a true smart material. *Eur Cells Mater*, 14:27, 2007.

[148] H.Y. Chou, J.J. Jagodnik, and S. Müftü. Prediction of bone remodelling around dental implant systems. *Journal of Biomechanics*, 41:1365 – 1373, 2008.

[149] Istabrak Hasan, Friedhelm Heinemann, and Christoph Bourauel. Biomechanical finite element analysis of small diameter and short dental implant. *Biomedical Engineering / Biomedizinische Technik*, pages 341–350, 2010a.

[150] Christoph Bourauel, Maria Aitlahrach, Friedhelm Heinemann, and Istabrak Hasan. Biomechanical finite element analysis of small diameter and short dental implants : extensive study of commercial implants. *Biomedical Engineering / Biomedizinische Technik*, pages 21–32, 2012.

[151] R. Wilhelm, I. Hasan, L. Keilig, F. Heinemann, H. Stark, and C. Bourauel. Biomechanical investigations of the secondary stability of commercial short dental implants in porcine ribs. *Biomed Tech (Berl).*, 59:507 – 513, 2014.

[152] B.S. Sotto-Maior, E.G. Mercuri, P.M. Senna, N.M. Assis, C.E. Francischone, and A.A. Del Bel Cury. Evaluation of bone remodeling around single dental implants of different lengths: a mechanobiological numerical simulation and validation using clinical data. *Computer Methods in Biomechanics and Biomedical Engineering*, 7:1 – 8, 2015.

[153] J. Y. Cha, M. D. Pereira, A. A. Smith, K. S. Houschyar, X. Yin, S. Mouraret, J. B. Brunski, and J. A. Helms. Multiscale analyses of the bone-implant interface. *Journal of Dental Research*, 94:482–490, 2015.

[154] Andy H. Choi, Richard C. Conway, and Besim Ben-Nissan. Finite-element modeling and analysis in nanomedicine and dentistry. *Nanomedicine*, 9:1681–1695, 2014.

[155] Stefan Ihde, Tomas Goldmann, Lucie Himmlova, Zoran Aleksic, and Jiri Kuzelka. Implementation of contact definitions calculated by FEA to describe the healing process of basal implants. *Biomedical papers of the Medical Faculty of the University Palacký, Olomouc, Czechoslovakia*, 152:169–173, 2008.

[156] Istabrak Hasan, Friedhelm Heinemann, Ludger Keilig, and Christoph Bourauel. Simulating the trabecular bone structure around dental implants : a case presentation. *Biomedical Engineering / Biomedizinische Technik*, 57:17–19, 2012a.

[157] I. Hasan, A. Rahimi, L. Keilig, Kai-Thomas Brinkmann, and C. Bourauel. Computational simulation of internal bone remodelling around dental implants: a sensitivity analysis. *Computer Methods in Biomechanics and Biomedical Engineering*, 15:807–814, 2012b.

[158] Salih Celik, Ludger Keilig, Istabrak Hasan, and Christoph Bourauel. Simulation of Bone Healing Processes around Dental Implants during the Healing Period. *Conference paper, 15th International Symposium on Computer Methods in Biomechanics and Biomedical Engineering and 3rd Conference on Imaging and Visualization(CMBBE 2018)P. R. Fernandes and J. M. Tavares (Editors)*, 2018.

[159] A. Mellal, H. W. A. Wiskott, J. Botsis, S. S. Scherrer, and U. C. Belser. Stimulating effect of implant loading on surrounding bone-comparison of three numerical models and validation by in vivo data. *Clinical Oral Implants Research*, 15:239–248, 2004.

[160] Eriko Kitamura, Roxana Stegaroiu, Shuichi Nomura, and Osamu Miyakawa. Biomechanical aspects of marginal bone resorption around osseointegrated implants: Considerations based on a three-dimensional finite element analysis. *Clinical Oral Implants Research*, 15:401–412, 2004.

[161] Kivanc Akca and Murat Cavit Cehreli. Biomechanical consequences of progressive marginal bone loss around oral implants: A finite element stress analysis. *Medical and Biological Engineering and Computing*, 44:527–535, 2006.

[162] Luigi Baggi, Ilaria Cappelloni, Franco Maceri, and Giuseppe Vairo. Stress-based performance evaluation of osseointegrated dental implants by finite-element simulation. *Simulation Modelling Practice and Theory*, 16:971–987, 2008.

[163] Z. Q. Lian, H. Guan, Y. C. Loo, S. Ivanovski, and N.W. Johnson. Finite element simulation of bone remodelling in human mandible around osseointegrated dental implant. *IOP Conf. Series: Materials Science and Engineering*, 2010.

[164] Atilim Eser, Ergin Tonuk, Kivanc Akca, and Murat Cavit Cehreli. Predicting time-dependent remodeling of bone around immediately loaded dental implants with different designs. *Medical Engineering and Physics*, 32:22–31, 2010.

[165] Daniel Lin, Qing Li, Wei Li, Naughton Duckmanton, and Michael Swain. Mandibular bone remodeling induced by dental implant. *Journal of Biomechanics*, 43:287 – 293, 2010.

[166] Atilim Eser, Ergin Tonuk, Kivanc Akca, Michel M. Dard, and Murat Cavit Cehreli. Predicting bone remodeling around tissue- and bone-level dental implants used in reduced bone width. *Journal of Biomechanics*, 46:2250–2257, 2013.

[167] Chaiy Rungsiyakull, Junning Chen, Pimduen Rungsiyakull, Wei Li, Michael Swain, and Qing Li. Bone's responses to different designs of implant-supported fixed partial dentures. *Biomechanics and Modeling in Mechanobiology*, 14:403–411, Apr 2014.

[168] J. Ojeda, J. Martínez-Reina, J. M. García-Aznar, J. Domínguez, and M. Doblaré. Numerical simulation of bone remodelling around dental implants. *Proceedings of the Institution of Mechanical Engineers, Part H: Journal of Engineering in Medicine*, 225:897–906, 2016.

[169] Scott J. Hazelwood, R. Bruce Martin, Mark M. Rashid, and Juan J. Rodrigo. A mechanistic model for internal bone remodeling exhibits different dynamic responses in disuse and overload. *Journal of Biomechanics*, 34:299–308, 2001.

132

[170] C.J. Hernandez. Simulation of bone remodeling during the development and treatment of osteoporosis. *PhD thesis, Stanford University*, 2001.

[171] David Taylor, Edoardo Casolari, and Cristina Bignardi. Predicting stress fractures using a probabilistic model of damage, repair and adaptation. *Journal of Orthopaedic Research*, 22:487–494, 2004b.

[172] A. Hosokawa. Numerical simulations of change in trabecular structure due to bone remodeling under ultrasound propagation. *Journal of Mechanics in Medicine and Biology*, 13:1350003, 2013.

[173] Chao Wang, Weiping Zhang, Deepal Haresh Ajmera, Yun Zhang, Yubo Fan, and Ping Ji. Simulated bone remodeling around tilted dental implants in the anterior maxilla. *Biomechanics and Modeling in Mechanobiology*, 15:701–712, 2016.

[174] Kangning Su, Li Yuan, and Jing Du. Bone remodeling under tooth loading. In Metals & Materials Society TMS, The Minerals, editor, *TMS 2017 146th Annual Meeting & Exhibition Supplemental Proceedings*, pages 331–340, Cham, 2017. Springer International Publishing.

[175] Nobuhiro Yoda, Keke Zheng, Junning Chen, Zhipeng Liao, Shigeto Koyama, Christopher Peck, Michael Swain, Keiichi Sasaki, and Qing Li. Biomechanical analysis of bone remodeling following mandibular reconstruction using fibula free flap. *Medical Engineering and Physics*, 56:1–8, 2018.

[176] R. Huiskes and E.Y.S. Chao. A survey of finite element analysis in orthopedic biomechanics: The first decade. *Journal of Biomechanics*, 16:385 – 409, 1983.

[177] D. P. Fyhrie and D. R. Carter. A unifying principle relating stress to trabecular bone morphology. *Journal of Orthopaedic Research*, 4:304–317, 1986.

[178] H Weinans, R Huiskes, and H J Grootenboer. Convergence and uniqueness of adaptive bone remodeling. *Transactions of the 35th Annual Meeting of the Orthopaedic Research Society*, 310, 1989.

[179] J. Wolff. Uber die innere architektur der knochen und ihre bedeutung fur die frage vom knochenwachstum. *Arch. Pathol. Anat. Physiol. Klin. Med.*, 50:389 – 453, 1870.

[180] John G. Skedros and Sidney L. Baucom. Mathematical analysis of trabecular 'trajectories' in apparent trajectorial structures: The unfortunate historical emphasis on the human proximal femur. *Journal of Theoretical Biology*, 244:15 – 45, 2007.

[181] K. Buchjek. Nonequilibrium bone remodelling: Changes of mass density and of the axes of anisotropy. *International Journal of Engineering Science*, 28:1039 – 1044, 1990.

[182] J. M. Garcia, M. A. Martinez, and M. Doblare. An anisotropic internal-external bone adaptation model based on a combination of cao and continuum damage mechanics technologies. *Computer Methods in Biomechanics and Biomedical Engineering*, 4:355 – 377, 2001.

[183] T. J. Reiter. Functional adaptation of bone and application in optimal structural design. *VDI-Berichte*, 17, 1996.

[184] Ali Vahdati and Gholamreza Rouhi. A model for mechanical adaptation of trabecular bone incorporating cellular accommodation and effects of microdamage and disuse. *Mechanics Research Communications*, 36:284–293, 2009.

[185] Elisabeth H. Burger and Jenneke Klein-Nulend. Mechanotransduction in bone—role of the lacuno-canalicular network. *The FASEB Journal*, 13:101–112, 1999.

[186] Elisabeth M. Aarden, Peter J. Nijweide, and Elisabeth H. Burger. Function of osteocytes in bone. *Journal of Cellular Biochemistry*, 55:287–299, 1994.

[187] S.C. Cowin, L. Moss Salentijn, and M.L. Moss. Candidates for the mechanosensory system in bone. *Journal of Biomechanical Engineering*, 113:191–197, 1991.

[188] Elisabeth M. Aarden, Peter J. Nijweide, and Elisabeth H. Burger. The effects of mechanical forces on bones and joints, experimental study on the rat tail. *Journal of Bone Joint Surg*, 79-B:1025–1030, 1997.

[189] Gholamreza Rouhi, Marcelo Epstein, Leszek Sudak, and Walter Herzog. Free surface density and microdamage in the bone remodeling equation: Theoretical considerations. *International Journal of Engineering Science*, 44:456 – 469, 2006.

[190] H.M. Frost. Presence of microscopic cracks in vivo in bone. *Henry Ford Hospital Medical Bulletin*, 1960.

[191] O. Verborgt, G.J. Gibson, and M.B. Schaffler. Loss of osteocyte integrity in association with microdamage and bone remodeling after fatigue in vivo. *Journal of Bone and Mineral Research*, 1:60–67, 2000.

[192] David Taylor and Jan-Herman Kuiper. The prediction of stress fractures using a 'stressed volume' concept. *Journal of Orthopaedic Research*, 19:919 – 926, 2001.

[193] D. Vashishth, K.E. Tanner, and et al. Contribution, development and morphology of microcracking in cortical bone during crack propagation. *J Biomech*, 33:1169–1174, 2000.

[194] H. Zilch, A. Rohlmann, and et al. Material properties of femoral cancellous bone in axial loading. part ii: Time dependent properties. *Arch Orthop Trauma Surg*, 97:257 – 262, 1980.

[195] R.T. Hart, D.T. Davy, and K.G. Heiple. A computational method for solution of adaptive elasticity problems. *Advances in Bioengineering, American Society of Mechanical Engineers*, pages 123–126, 1982.

[196] R.T. Hart, D.T. Davy, and K.G. Heiple. A computational method for stress analysis of adaptive elastic materials with a view towards applications in strain-induced bone remodelling. *Journal of Biomechanical Engineering*, 106:342–350, 1984b.

[197] S.C. Cowin, R.T. Hart, J.R. Balser, and D.H. Kohn. Functional adaptation in long bones: Establishing in vivo values for surface remodeling rate coefficients. *Journal of Biomechanics*, 18:665 – 684, 1985.

[198] D.R. Carter. Mechanical loading histories and cortical bone remodeling. *Calcified Tissue Int.*, 36:19 – 24, 1984.

[199] Christoph Bourauel, Dirk Vollmer, and Andreas Jäger. Application of bone remodeling theories in the simulation of orthodontic tooth movements. *Journal of Orofacial Orthopedics / Fortschritte der Kieferorthopädie*, 61:266–279, 07 2000.

[200] S.C. Cowin. Adaptive elasticity: A review and critique of a bone tissue adaptation model. *Engineering Transactions*, 51, 2015.

[201] Gholamreza Rouhi. Theoretical aspects of bone remodeling and resorption processes. *PhD Thesis, University of Calgary*, 2006.

135

[202] D.R. Carter and W.C. Hayes. The compressive behavior of bone as a two-phase porous structure. *Journal of Bone Joint Surg Am.*, 59:954 – 962, 1977.

[203] U. Lekholm and G.A. Zarb. Patient selection and preparation. in: Branemark p.i., zarb g., albrektsson t., eds. tissue-integrated prostheses. osseointegration in clinical dentistry. *Chicago: Quintessence Publishing Company Inc.*, pages 199–209, 1985.

[204] Engquist Bo, Bergendal Tom, Kallus Thomas, and Linden Ulf. A retrospective multicenter evaluation of osseointegrated implants supporting overdentures. *The International Journal of Oral and Maxillofacial implants*, 3:129–134, 1988.

[205] B. Friberg. Treatment with dental implants in patients with severe osteoporosis: A case report. *Int Journal Periodontics Restorative Dent*, 1994.

[206] C.E. Misch. Progressive loading of bone with implant prostheses. *PJ Dent Symp*, 1:50–53, 1993.

[207] Trisi Rao and Walter Rao. Bone classification: clinical-histomorphometric comparison. *Clinical Oral Implants Research*, 10:1–7, 1999.

[208] Oded Bahat. Treatment planning and placement of implants in the posterior maxillae: Report of 732 consecutive nobelpharma implants. *International Journal of Oral and Maxillofacial Implants*, 8:151–161, 1993.

[209] B. Friberg, T. Jemt, and U. Lekholm. Failures in 4,641 consecutively placed branemark dental implants: A study from stage 1 surgery to the connection of completed prostheses. *International Journal of Oral and Maxillofacial Implants*, 6:142–146, 1991.

[210] K.W. Higuchi, Folmer Tiddo, and Kultje Christina. Implant survival rates in partially edentulous patients: A 3-year prospective multicenter study. *Journal of Oral and Maxillofacial Surgery*, 53:264 – 268, 1995.

[211] T. Jemt and U. Lekholm. Implant treatment in edentulous maxillae: A five-year followup report on patients with different degrees of jaw resorption. *International Journal of Oral and Maxillofacial Implants*, 10:303–311, 1995.

[212] N. Arpak, W. Niedermeier, I. Nergiz, A. Schulz, and H. Bostanci. Morphometry of the periimplant of immediate and late endosseous implants. *Journal of Dent Res*, pages 74–110, 1995.

[213] D.R. Carter and W.E. Caler. Cycle-dependent and time-dependent bone fracture with repeated loading. *Journal of Biomech Eng*, 105:166 – 170, 1983.

[214] C.E. Misch. Density of bone: Effect on treatment plans, surgical approach, healing and progressive bone loading. *Int Journal Oral Implantol*, 6:23–31, 1990.

[215] H.F. Morris, S. Ochi, and W. Gillette. Bone quality and implant integration during follow-up in the dicrg clinical study. *Journal of Dent Res*, 74:495–753, 1995.

[216] T. Jemt and K.G. Strid. Assessment of bone quality from cutting resistance during implant surgery. *Int Journal OralMaxillofac Surg*, 9:279–288, 1994.

[217] C.E. Misch. A key determinant for clinical success. in: Misch c.e., ed. contemporary implant dentistry. *2nd ed. St Louis, Mo: Mosby*, pages 109–118, 1999.

[218] C. Lindh, M. Nilsson, B. Klinge, and A. Petersson. A quantitative computed tomography of trabecular bone in the mandible. *Dentomaxillofacial Radiology*, 25:146–150, 1996.

[219] B. Friberg, L. Sennerby, J. Roos, and U. Lekholm. dentification of bone quality in conjunction with insertion of titanium implants: A pilot study in jaw autopsy specimens. *Clin Oral Implants Res*, 6:213–219, 1995.

[220] Louis Charles Gerstenfeld, Dennis M Cullinane, George L Barnes, Dana T Graves, and Thomas A. Einhorn. Fracture healing as a postnatal developmental process: molecular, spatial, and temporal aspects of its regulation. *Journal of cellular biochemistry*, 88:873–84, 2003a.

[221] Liesbet Geris, Alf Gerisch, Jos Vander Sloten, Rüdiger Weiner, and Hans Van Oosterwyck. Angiogenesis in bone fracture healing: A bioregulatory model. *Journal of Theoretical Biology*, 251:137 – 158, 2008.

[222] Lutz Claes, Peter Augat, Gebhard Suger, and Hans-Joachim Wilke. Influence of size and stability of the osteotomy gap on the success of fracture healing. *Journal of Orthopaedic Research*, 15:577–584, 1997.

[223] Lutz Claes, C.A. Heigele, C. Neidlinger-Wilke, D. Kaspar, W. Seidl, K.J. Margevicius, and P Augat. Effects of mechanical factors on the fracture healing process. *Clin. Orthop*, pages 132–147, 1998.

[224] PJ Prendergast. Finite element models in tissue mechanics and orthopaedic implant design. *Clinical Biomechanics*, 12:343 – 366, 1997.

[225] Marjolein C.H.van der Meulen and Rik Huiskes. Why mechanobiology? a survey article. *Journal of Biomechanics*, 2002.

[226] Peter Augat, Johannes Burger, Sandra Schorlemmer, Thomas Henke, Manfred Peraus, and Lutz Claes. Shear movement at the fracture site delays healing in a diaphyseal fracture model. *Journal of Orthopaedic Research*, 21:1011–1017, 2003.

[227] D R Epari, G N Duda, and M S Thompson. Mechanobiology of bone healing and regeneration: in vivo models. *Proceedings of the Institution of Mechanical Engineers, Part H: Journal of Engineering in Medicine*, 224:1543–1553, 2010.

[228] Hanna Isaksson. Recent advances in mechanobiological modeling of bone regeneration. *Mechanics Research Communications*, 42:22 – 31, 2012. Recent Advances in the Biomechanics of Growth and Remodeling.

[229] Richard Marsell and Thomas Einhorn. The biology of fracture healing. *Injury*, 42:551–555, 2011.

[230] S.M. Perren and L. Claes. Biology and biomechanics in fracture management. in: Ruedi, t.p., murphy, w.m. (eds.). *AO Principles of Fracture Fanagement. Thieme, Stuttgart*, page 7 – 32, 2000.

[231] H.M. Frost. The biology of fracture healing. an overview for clinicians. part i. *Clin. Orthop*, pages 283 – 293, 1989a.

[232] H.M. Frost. The biology of fracture healing. an overview for clinicians. part ii. *Clin. Orthop*, pages 294 – 309, 1989b.

[233] P. I. Branemark, B.O. Hansson, R. Adell, U. Breine, J. Lindstrom, O. Hallen, and A. Ohman. Osseointegrated implants in the treatment of the edentulous jaw. experience from a 10-year period. *Scand journal Plast Reconstr Surg Suppl*, 16:1–132, 1977.

[234] J.E. Davies. Understanding peri-implant endosseous healing. *journal Dent Educ*, 67:932–949, 2003.

[235] F. Marco, F. Milena, G. Gianluca, and O. Vittoria. Peri-implant osteogenesis in health and osteoporosis. *Micron*, 36:630–644, 2005.

[236] R. Gapski, H.L. Wang, P. Mascarenhas, and N.P. Lang. Critical review of immediate implant loading. *Clin Oral Implants Res*, 14:515–527, 2003.

[237] M. Esposito, J.M. Hirsch, U. Lekholm, and P. Thomsen. Biological factors contributing to failures of osseointegrated oral implants. (i). success criteria and epidemiology. *Eur Jurnal Oral Sci*, 106:527–551, 1998a.

[238] M. Esposito, J.M. Hirsch, U. Lekholm, and P. Thomsen. Biological factors contributing to failures of osseointegrated oral implants. (ii). etiopathogenesis. *Eur Journal Oral Sci*, 106:721–764, 1998b.

[239] Bertil Friberg, Kerstin Gröndahl, Ulf Lekholm, and Per-Ingvar Branemark. Long-term follow-up of severely atrophic edentulous mandibles reconstructed with short branemark implants. *Clinical Implant Dentistry and Related Research*, 2:184–189, 2000.

[240] I. Hasan. Computational simulation of trabecular bone distribution around dental implants and the influence of abutment design on the bone reaction for implant-supported fixed prosthesis. *PhD thesis, University of Bonn*, 2011.

[241] I. Hasan, A. Rahimi, L. Keilig, R. Krause, and C. Bourauel. Applying adaptive bone remodelling theory to the alveolar bone around dental implants in the fully osseointegrated state. *9th International Symposium on Computer Methods in Biomechanics and Biomedical Engineering, Valencia*, 264D, 2010b.

[242] Harrie Weinans, Dale R. Sumner, Ruben Igloria, and Raghu N Natarajan. Sensitivity of periprosthetic stress-shielding to load and the bone density–modulus relationship in subject-specific finite element models. *Journal of Biomechanics*, 33:809 – 817, 2000.

[243] W. C. Hayes, S. J. Piazza, and P. K. Zysset. Biomechanics of fracture risk prediction of the hip and spine by quantitative computed tomography. *Radiologic Clinics of North America*, 29:1–18, January 1991.

[244] Emil Nutu. Role of initial density distribution in simulations of bone remodeling around dental implants. *Acta of Bioengineering and Biomechanics*, 20:23 – 31, 2018.

[245] N. Meredith. Assessment of implant stability as a prognostic determinant. *International Journal of Prosthodontics*, 11:491 – 501, 1998.

[246] H.M. Frost, Y.Y. Su, and D. Drescher. Insertion angle impact on primary stability of orthodontic mini-implants. *Angle Orthod.*, 78:1065 – 1070, 2008.

[247] P.K. Chang, Y.C. Chen, C.C. Huang, W.H. Lu, Y.C. Chen, and H.H. Tsai. Distribution of micromotion in implants and alveolar bone with different thread profiles in immediate loading: a finite element study. *International Journal of Oral Maxillofac Implants*, 27:e96 – 101, 2012.

[248] Werner Winter, Daniel Klein, and Matthias Karl. Effect of model parameters on finite element analysis of micromotions in implant dentistry. *Journal of Oral Implantology*, 39:23–29, 2013.

[249] Ertugrul H.Zeynep and Pipko Donald J. Measuring mobility of 2 dental implant fixtures of different configurations: an in vitro study. *Implant Dent.*, 15:290–297, 2006.

[250] Philipp Leucht, Jae-Beom Kim, Rima Wazen, Jennifer A. Currey, Antonio Nanci, John B. Brunski, and Jill A. Helms. Effect of mechanical stimuli on skeletal regeneration around implants. *Bone*, 40:919 – 930, 2007.

[251] Rima M. Wazen, Jennifer A. Currey, Hongqiang Guo, John B. Brunski, Jill A. Helms, and Antonio Nanci. Micromotion-induced strain fields influence early stages of repair at bone–implant interfaces. *Acta Biomaterialia*, 9:6663 – 6674, 2013.

[252] Eric P. Holmgren, Robert J. Seckinger, Leslie M. Kilgren, and Francis Mante. Evaluating parameters of osseointegrated dental implants using finite element analysisa two-dimensional comparative study examining the effects of implant diameter, implant shape, and load direction. *Journal of Oral Implantology*, 24:80–88, 1998.

[253] Franklin A. Young, Keith R. Williams, Robert Draughn, and Robert Strohaver. Design of prosthetic cantilever bridgework supported by osseointegrated implants using the finite element method. *Dental Materials*, 14:37 – 43, 1998.

[254] H.-J. Chun, S.-Y. Cheong, J.-H. Han, S.-J. Heo, J.-P. Chung, I.-C. Rhyu, Y.-C. Choi, H.-K. Baik, Y. Ku, and M.-H. Kim. Evaluation

of design parameters of osseointegrated dental implants using finite element analysis. *Journal of Oral Rehabilitation*, 29:565–574, 2002.

[255] Jian-Ping Geng, Keson B.C. Tan, and Gui-Rong Liu. Application of finite element analysis in implant dentistry: A review of the literature. *Journal of Prosthetic Dentistry*, 85:585 – 598, 2001.

[256] Michele Calì, Elisabetta Maria Zanetti, Salvatore Massimo Oliveri, Riccardo Asero, Stefano Ciaramella, Massimo Martorelli, and Cristina Bignardi. Influence of thread shape and inclination on the biomechanical behaviour of plateau implant systems. *Dental Materials*, 34:460 – 469, 2018.

[257] Paolo Trisi, Marco Berardini, Antonello Falco, and Michele Podaliri Vulpiani. Effect of implant thread geometry on secondary stability, bone density, and bone-to-implant contact: A biomechanical and histological analysis. *Implant dentistry*, 24 4:384–91, 2015.

[258] Kıvanç Akça, Mete I. Fanuscu, and Angelo A. Caputo. Effect of compromised cortical bone on implant load distribution. *Journal of Prosthodontics*, 17:616–620, 2008.

[259] Heng-Li Huang, Chin-Han Chang, Jui-Ting Hsu, Alison M. Fallgatter, and Ching-Chang Ko. Comparison of implant body designs and threaded designs of dental implants: A3-dimensional finite element analysis. *International Journal of Oral and Maxillofacial Implants*, 22:551–562, 2008.

[260] P. Bicudo, J. Reis, A.M. Deus, L. Reis, and M.F. Vaz. Mechanical behaviour of dental implants. *Procedia Structural Integrity*, 1:26 – 33, 2016. XV Portugese Conference on Fracture, PCF 2016, 10-12 February 2016, Paco de Arcos, Portugal.

[261] H.L. Huang, C.H. Chang, J.T. Hsu, A.M. Fallgatter, and C.C. Ko. Comparison of implant body designs and threaded designs of dental implants: a 3-dimensional finite element analysis. *International Journal of Oral Maxillofac Implants*, 22:551 – 562, 2007.

[262] Cynthia S. Petrie and John L. Williams. Comparative evaluation of implant designs: influence of diameter, length, and taper on strains in the alveolar crest. *Clinical Oral Implants Research*, 16:486–494, 2005.

[263] P.M. Cattaneo, M. Dalstra, and B. Melsen. The finite element method: a tool to study orthodontic tooth movement. *Journal of Dental Research*, 84:428–433, 2005.

[264] Sheng-Hui Liao, Ruo-Feng Tong, and Jin-Xiang Dong. Influence of anisotropy on peri-implant stress and strain in complete mandible model from ct. *Computerized Medical Imaging and Graphics*, 32:53 – 60, 2008.

[265] Nina Von Wovern and Kaj Stoltze. Ex and age differences in bone morphology of mandibles. *Scandinavian Journal of Dental Research*, 86:478–485, 1978.

[266] X. Zhou, Z. Zhao, M. Zhao, and Y. Fan. The boundary design of mandibular model by means of the three-dimensional finite element method. *West China Journal of Stomatology*, 17:29–32, 1999.

[267] H.C. Kao, Y.W. Gung, T.F. Chung, and M.L. Hsu. The influence of abutment angulation on micromotion level for immediately loaded dental implants: a 3-d finite element analysis. *International Journal of Oral and Maxillofacial Implants*, 23:623–630, 2008.

[268] Daniel Lin, Qing Li, Wei Li, and Michael Swain. Dental implant induced bone remodeling and associated algorithms. *Journal of the Mechanical Behavior of Biomedical Materials*, 2:410–432, 2009.

[269] D. Bozkaya, S. Muftu, and A. Muftu. Evaluation of load transfer characteristics of five different implants in compact bone at different load levels by finite elements analysis. *Journal of Prosthetic Dentistry*, 92:523–530, 2004.

[270] Jae-Hoon Lee, Val Frias, Keun-Woo Lee, and Robert F. Wright. Effect of implant size and shape on implant success rates: A literature review. *The Journal of Prosthetic Dentistry*, 94:377 – 381, 2005.

[271] G. Robert and L. Marcus. Restorative dental materials. *Mosby Year Book inc.*, 1997.

[272] Z.Q. Lian, H. Guan, and Y.C. Loo. Optimum degree of bone-implant contact in bone remodelling induced by dental implant. *Procedia Engineering*, 14:2972 – 2979, 2011. The Proceedings of the Twelfth East Asia-Pacific Conference on Structural Engineering and Construction.

[273] Jose Manuel Garcia-Aznar, Thomas Rüberg, and Manuel Doblare. A bone remodelling model coupling microdamage growth and repair by 3d bmu-activity. *Biomechanics and Modeling in Mechanobiology*, 4:147–167, 2005.

[274] J. Martínez-Reina, J.M. García-Aznar, J. Domínguez, and M. Doblaré. On the role of bone damage in calcium homeostasis. *Journal of Theoretical Biology*, 254:704 – 712, 2008.

[275] Raoof Korabi, Shemtov-Yona Keren, Dorogoy Avraham, and Rittel Daniel. The failure envelope concept applied to the bone-dental implant system. *Scientific Reports*, 2017.

[276] Vee San Cheong, Paul Fromme, Aadil Mumith, Melanie J. Coathup, and Gordon W. Blunn. Novel adaptive finite element algorithms to predict bone ingrowth in additive manufactured porous implants. *Journal of the Mechanical Behavior of Biomedical Materials*, 87:230 – 239, 2018.

[277] L.E Claes and C.A Heigele. Magnitudes of local stress and strain along bony surfaces predict the course and type of fracture healing. *Journal of Biomechanics*, 32:255 – 266, 1999.

[278] H.W.J. Huiskes and S.J. Hollister. From structure to process, from organ to cell : recent developments of fe-analysis in orthopaedic biomechanics. *Journal of Biomechanical Engineering : Transactions of the ASME*, 115:520–527, 1993.

[279] JingYun Han, JianXia Hou, Gang Zhou, Chao Wang, and YuBo Fan. A histological and biomechanical study of bone stress and bone remodeling around immediately loaded implants. *Science China Life Sciences*, 57:618–626, Jun 2014.

[280] Soroush Irandoust and Sinan Muftu. The interplay between bone healing and remodeling around dental implants. *Scientific Reports*, 10:4335, 2020.

[281] Daniel Lin, Qing Li, Wei Lic, Ionut Ichim, and Michael Swain. Evaluation of dental implant induced bone remodelling by using a 2d finite element model. *5th Australian Congress on Applied Mechanics, ACAM 2007*, 12 2007.

[282] Han-Yi Cheng, Kuo-Tien Chu, Fa-Chih Shen, Yung-Ning Pan, Hsin-Hua Chou, and Keng-Liang Ou. Stress effect on bone remodeling and

osseointegration on dental implant with novel nano/microporous sur-face functionalization. *Journal of Biomedical Materials Research Part A*, 101A:1158–1164, 2013.

[283] D. Kurniawan, F.M. Nor, H.Y. Lee, and J.Y. Lim. Finite element analysis of bone–implant biomechanics: refinement through featuring various osseointegration conditions. *International Journal of Oral and Maxillofacial Surgery*, 41:1090 – 1096, 2012.